Defects and transport in fluorite related materials $Nd_2Ce_2O_7$ and $Gd_2Ce_2O_7$

Shiyang Cheng

Master Thesis in Materials, Energy and Nanotechnology

DEPARTMENT OF PHYSICS

UNIVERSITY OF OSLO

JUNE 2012

Preface

The thesis is the review of my master work and experiments and I delivery it to fulfill my Master of Science degree at the Department of Chemistry, University of Oslo. The experimental work is executed at the Centre for Materials Science and Nanotechnology (SMN) during the time from August 2010 to May 2012.

Firstly, I would like to appreciate my supervisor, associate professor Reidar Haugsrud for his enthusiasm, patiently, friendly guide and advice in my two years' study. Furthermore, I am thankful to my co-supervisors, Professor Truls Evine Norby and Harald Fjeld for their help in the academic. I would like thank Ragnhild Hancke for helping me in the TG measurement and Camilla Vigen in the XRD Rietveld refinement. Thanks Einar Vøllestad for his great suggestions in the low temperature measurement. Thanks Zuoan Li and Wen Xing for helping me in my studies and life in Norway.

Finally, I am grateful to my parents, Xuegeng Cheng and Xiaomei Wang for their meticulous care and support in my life and study.

University of Oslo, June 2012

Shiyang Cheng

Abstract

In this master thesis, defects and transport properties in fluorite related materials $Ln_2Ce_2O_7$ (Ln=Nd, Gd) were investigated by electrical measurements and thermogravimetry. $Nd_{2-x}Ca_xCe_2O_{7-\delta}$ (x=0, 0.05, 0.1, 0.2) and $Gd_{2-x}Ca_xCe_2O_{7-\delta}$ (x=0, 0.05, 0.1, 0.2) were synthesized by solid state reactions and wet chemical methods. Crystal structures were characterized by XRD and the ratio of the chemical elements and microstructure were studied by SEM-EDS. Rietveld refinement was used to determine the cell parameters and occupancy of oxygen ions. The electrical characterization was done by measuring the AC conductivity as a function of temperature from 1100°C to 300°C, of oxygen partial pressure (pO_2) and water vapor partial pressure (pH_2O). Electrical measurements were also carried out from 100°C to -60°C. The relative mass change of the materials as a consequence of the temperature decrease from 1100°C to 300°C was studied by thermogravimetry under wet and dry conditions.

$Nd_2Ce_2O_7$ and $Gd_2Ce_2O_7$ crystallize in fluorite type structure and cubic rare earth oxide structure, respectively. According to the SEM characterization and Rietveld refinement, the solubility of calcium in $Nd_2Ce_2O_7$ was less than 10% but more than 20% in $Gd_2Ce_2O_7$. It was observed from curve fitting of pO_2 and pH_2O dependency of conductivity that oxygen ion conduction predominates from 1100°C to 600°C in wet O_2 or Ar and protons become significant below 500°C. It is suggested that association between oxygen vacancies and acceptor dopants happened in doped samples. Oxygen vacancies in $Nd_2Ce_2O_7$ and $Gd_2Ce_2O_7$ are not fully hydrated at 350°C which is in agreement with the net mass difference in TG results measured under wet and dry conditions. Hydration enthalpy cannot be obtained by modeling results of pH_2O and pO_2 dependency of conductivity but it should be fairly low because of the low amount of water absorption from 1100°C to 300°C. Proton mobility and dissolution decrease with decreasing ionic radius of lanthanides in $Ln_2Ce_2O_7$. The decreasing proton mobility can be due to the decreasing polarization of lattice or symmetry. The enthalpy of oxygen ion mobility in $Ln_2B_2O_7$ (Ln=lanthanides, B=Ce, Zr) decreases with increasing radius of Ln^{3+} due to larger unit cell volume facilitating oxygen ion mobility. Also, the enthalpy of oxygen ion mobility in $Ln_2Ce_2O_7$ with a high degree of anion disorder is much higher than that in $Ln_2Zr_2O_7$ with ordered oxygen ions. It is suggested the different oxygen ion migration pathways in $Ln_2B_2O_7$ with large difference in anion disorder. The higher cation disorder in $Ln_2Ce_2O_7$ than $Ln_2Zr_2O_7$ can also affect oxygen ion mobility due to the trapping effect between cation antitsite and oxygen vacancies.

At room temperature, the conductivities of $Nd_2Ce_2O_7$, $Gd_2Ce_2O_7$ and $Gd_{1.95}Ca_{0.05}Ce_2O_{7-\delta}$ are around 1×10^{-5} Scm^{-1}. TG measurement and the relation of $\sigma \propto pH_2O^{2.8}$ indicate the enhanced conductivity should be ascribed to protonic conduction. It is suggested that

protonic conduction at room temperature is independent of grain size and doping concentration. The conductivity change at 0°C suggests a phase transition from water to ice. Protons are thereby expected to transport in water condensed in micro-sized pores or cracks in the form of hydronium ions.

Table of Contents

1. INTRODUCTION

1.1. Background

The global worlds' economic keep increasing rapidly and people's living standard are developing at the same time. The relationship between the development and energy is crucial, and people need more energy for development. Fossil fuels, which is the most important energy source, have been using by people for a long time. However, this will not last forever. With the reduction of the global oil reserves, fuels become increasingly expensive. The traditional way to produce electricity is burning the petroleum fuels or coal. The process mainly includes converting chemical energy to thermal energy and converting thermal energy to electrical energy. Nevertheless, the efficiency is low and this double conversion process may waste a lot of chemical energy. A report from IPCC (International panel on climate change) [1] pointed out that about 90% of the CO_2 emission is produced from combustion of fossil fuels and CO_2 as a greenhouse pollution may lead to global warming. Furthermore, a report from IEA (International Energy Agency) [2] pointed out that 43% of CO_2 emission from fuel combustion were produced from coal, 37% from oil and 20% from gas in 2009. According to the statistic from Mauna Loa Observatory [3] (cf. Figure 1.1a), atmospheric CO_2 concentration is about 310 ppmv in 1960 and increase to 400 ppmv in 2012. Furthermore, the annual mean growth rate is also increase from 1ppm/year to 2ppm/year [3] (cf. Figure 1.1b). From these results, the energy crisis and environmental problems becomes serious.

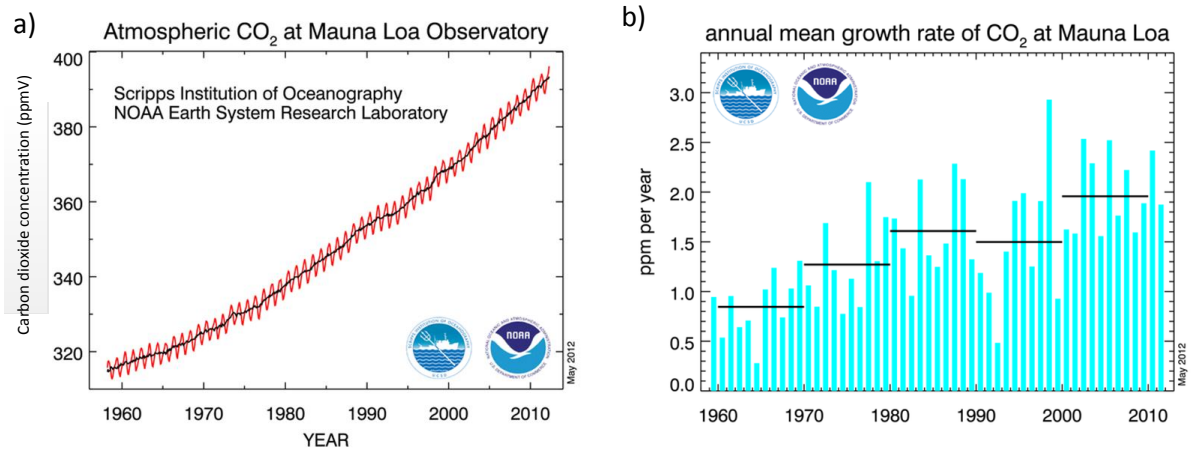

Figure 1.1 a) Annual atmospheric CO_2 concentrations (1960-2012)[3] b) annual mean CO_2 growth rates[3].

One possible way to solve these problems is to utilize some sustainable energy sources, such as solar energy, wind energy, hydro energy and tidal energy, etc. Another possible way is to seek more environmentally friendly power generation methods to exploit these fossil fuels.

Fuel cell is one of the promising devices which theoretically convert chemical energy to electricity efficiency between 40%-60% [4]. Unlike internal combustion engines which must undergo two steps of energy conversion, the fuel cell can directly convert chemical energy to electricity without limitation of Carnot cycle. Fuel cell can operate with a variety of fuels, e.g. hydrogen, natural gas, syngas, methane, butane etc. For the fuel cell using hydrogen as the fuel, the emission is just water in theory. Solid state ionic conductors are promising players in future energy technologies, e.g. as electrolytes in fuel cells or as membranes for gas separation.

1.2. Solid oxide fuel cell (SOFC)

Solid oxide fuel cell is one of the promising fuel cell which uses solid oxide as the electrolyte. As shown in Figure 1.2a, a SOFC consists of a ceramic electrolyte and two solid electrodes. In traditional SOFC, the electrolyte is a pure oxygen ion conductor with high electron resistance. Oxygen is reduced to oxygen ions and electrons at the cathode followed by oxygen ions diffusing through the electrolyte and reacting with hydrogen at the anode. The operating temperature for SOFC is typically range between 800°C and 1000°C that always associate with undesirable phenomena e.g. interaction and insulating phase formation [5].

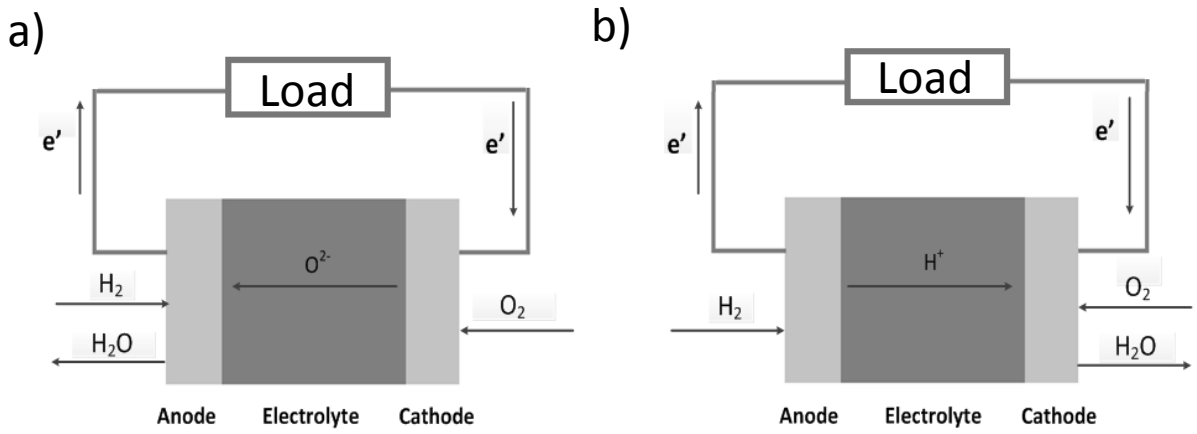

Figure 1.2 a) Working program of oxygen ion SOFC b) proton conducting SOFC.

Compared with traditional SOFC, proton conducting solid oxide fuel cells (PC-SOFCs) is beneficial for its much lower operation temperature e.g. 600°C-700°C for Ba(Ce,Zr,Ln)O_3 based PC-SOFCs [5]. As Figure 1.2b shows, similarly as traditional oxygen iron conductor oxide fuel cell, the electrolyte in this fuel cell is proton conductor. The hydrogen is divided into protons and electrons at anode. Protons then diffuse through the electrolyte and combine with oxygen to form water at cathode.

1.3. Gas separation membrane

Some conventional methods for separating gases, such as high temperature gas fraction, not only cost high energy, but also cannot entirely separate the gases. One may, in gross terms divide these high temperature conductors into materials with two types of functional properties; oxide ion conductors and proton conductors. Both classes can be applied as electrolyte membranes in solid oxide fuel cells, and when they also possess electronic transport, they are susceptible to permeation of oxygen and hydrogen, respectively (ambipolar ionic-electronic transport). Mixed ionic-electronic conductors as such can be utilized as membranes in processes related to production of high purity hydrogen from natural gas and coal gasified gas streams. Figure 1.3 displays the schematic of a gas separation system consisting of oxygen and hydrogen separation membranes.

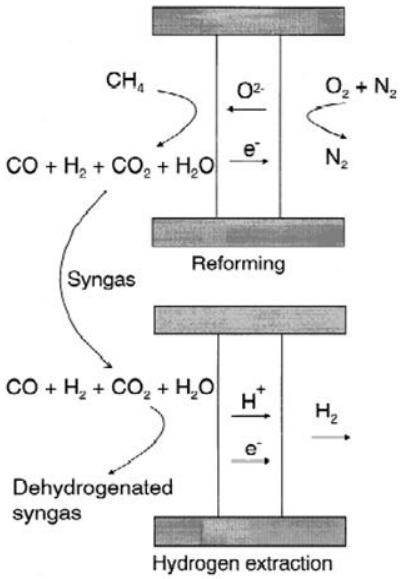

Figure 1.3 The system of mixed oxygen ion-electronic conduction for oxygen separation and mixed proton electronic conduction for hydrogen extraction [6].

1.4. Objective of the thesis

Oxides with nominal composition $A_2B_2O_7$, where A is a trivalent cation and B is a four-valent cation, often take on the so-called pyrochlore structure. This is an interesting structural family that has been shown to display remarkable properties, e.g. with respect to ionic conduction. Pyrochlores with A-site rare-earths and e.g. Ti, Zr, Ce, Sn etc as B-site cations have been in focus as ionic and mixed ionic-electronic conductors, in particular as oxide ion conductors but also as proton conductors. Previous studies demonstrated that electrical conductions vary with the different cations in pyrochlore, but the relationship is still unclear. The aim of the master thesis is to study how the ionic and electronic conduction vary with the detail of the structure and the chemical nature of the respective cations in a pyrochlore

family $Ln_2Ce_2O_7$ (Ln=Nd, Gd). Also, previous studies reported that the cations or anions may disorder in $Ln_2Ce_2O_7$, but the relationships between the ionic conduction and disorder of constitutes is still unclear. In this work, the effect of cation or anion disorder on the defects and transport in $Ln_2Ce_2O_7$ is studied. This may help to clarify the ionic transport in other pyrochlore related materials.

In addition, many fluorite related materials exhibit enhanced conduction at room temperature, but defects and diffusion at such low temperatures is controversial in many studies. Thus, in order to understand the defects and diffusion at low temperatures, another part of the work is emphasized on the study of electrical properties of $Ln_2Ce_2O_7$ at low temperatures.

2. Theory

The main theories in this master research focus on the defect chemistry, which are related in the types of the defects, formation of the defects, thermodynamic parameters, and the electrochemical diffusion of defects in disordered fluorite related materials $Nd_2Ce_2O_7$ and $Gd_2Ce_2O_7$. The contribution of the different defects in the polycrystalline can be distinguished due to the vary dependencies as a function of the different atmospheres. The content of the defect chemistry is based on the compendium "Defects and transport in crystalline solids" compiled by Norby and Kofstad [7] and the electrical measurement refers to Norby's "Electrical measurement" [8].

2.1. Defect chemistry

2.1.1. Defects in crystalline materials

Defects are present in all crystalline materials at any temperatures and play important roles in the chemical and physical properties. Defects can be divided into different types depending on their dimension, as summarized in the Table 2.1.

Table 2.1 Types of defects in crystalline materials [9].

Dimension	type	Samples
Zero dimensional defects	point defects	Vacancies, interstitial atoms, and substitutions impurity atoms
One-dimensional defects	line defects	dislocations
Two-dimensional defects	planar defects	stacking faults, grain boundaries, internal and external surfaces
Three-dimensional defects	volume defects	Defect clusters, voids, and precipitates

In addition to these structural defects, crystals also contain electronic defects like electrons and electron holes, which tend to move rather freely in the crystal under some appropriate situations, such as heating, light shining, and electric field etc.

2.1.2. Kröger-Vink notation

Point defects play vital roles for many properties of polycrystalline materials. F.A.Kröger and H.J.Vink developed a system of notations to conveniently express the point defects in the lattice. As far as a general unit in the notation, A_b^c , A is the symbol of a certain chemical element or a vacancy, b represents the site in sublattice that the species occupy, and c denotes the effective charge. The electron and electron hole have their particular notations e' and $h^{\bullet}$, respectively. The effective charge, positive, negative charge and neutral charges are denoted with superscripts dot •, slash ′ and cross x, respectively. Furthermore, the number of the dots or slashes represents the effective charge when the charge carriers with more than one effective charges. Ions which occupy interstitial sites in the crystal lattice are with subscript "i".

2.1.3. Kröger-Vink compatible notation

The Kröger-Vink notation can define the cation sites, anion sites, interstitials or substitutions in the common crystal lattice. For materials with inherent disorder or partial occupancy of the cation or anion sites, the disordered cation or anion sites are not appropriate to be expressed by Kröger-Vink notation, such as $Nd_2Ce_2O_7$ (NCO) and $Gd_2Ce_2O_7$ (GCO) in this thesis. According to the XRD results and Rietveld refinement, $Nd_2Ce_2O_7$ crystallizes in a fluorite structure (F-type) whose cations and anions are totally disordered .Although $Gd_2Ce_2O_7$ crystallizes in a cubic rare earth oxide (C-type) structure with ordered oxygen ions, it may transfer to the F-type structure with disordered oxygen ions at high temperatures [10]. Since oxygen vacancies and oxygen ions are randomly distributed in the oxygen sublattice in NCO and GCO, defects in GCO and NCO can be expressed by a compatible KV notation in this work. The compatible KV notation, which is developed by Norby [11], is to statistically describe the defects in these materials with disordered sublattice. In a disordered fluorite, oxygen ions statistically occupy 7/8 of the perfect oxygen sites and the intrinsic structural oxygen vacancies take place the rest 1/8 of the oxygen sites. The site in this situation can be written as $\frac{7}{8}O$ and the statistical charge of this site is 7/4. Furthermore, since the real charge of oxygen ion is -2, so the effective charge of this compatible oxygen site is -1/4. Therefore, the oxygen sites in the disorder fluorite can be figured out as a new type of defect and the new oxygen vacancy is $V_{\frac{7}{8}O}^{\frac{7}{4}\bullet}$. Similarly, the effective charge of the compatible oxygen site is 1/4 and the derived Kröger-Vink notation is $O_{\frac{7}{8}O}^{\frac{1}{4}\prime}$. The crystal structure will be discussed in Chapter 5. The symbol notations used in this work are given in Table 2.2.

Table 2.2 List of defects relevant for the work done in this thesis.

Notation	Defect
$V_{\frac{7}{8}O}^{\frac{7}{4}\bullet}$	Compatible oxygen vacancy
$O_{\frac{7}{8}O}^{\frac{1}{4}/}$	Compatible oxygen site
$h^{\bullet}$	Electron hole
$e^{/}$	Electron
$Ca_{Nd}^{/}$	Calcium substitute Neodymium
$Ca_{Gd}^{/}$	Calcium substitute Gadolinium
$OH_{\frac{7}{8}O}^{\frac{3}{4}\bullet}$	Compatible proton

2.1.4. Defect and thermodynamics

The change of Gibbs free energy ΔG of a chemical reaction in a closed system depends on the change of enthalpy ΔH, the change of entropy ΔS, and the absolute temperature, which can be written as

$$\Delta G = \Delta H - T\Delta S \qquad \textbf{Equation 2-1}$$

As a chemical reaction, the formation of point defects in solids can be treated by statistical thermodynamics. Specifically, if n_v moles of vacancies are formed in the solid, the total change of enthalpy is $n_v\Delta H$ which stands for the energy for formation of new sites. There are two different types of entropy. One is the vibrational entropy, ΔS_{vib}, which describes the entropy change due to the vibration around each new sites. The total vibrational entropy is proportional to the number of the vacancies n_v, which gives $n_v\Delta S_{vib}$. The other entropy is called configurational entropy,ΔS_{config}, which represents the distribution of the new sites among the whole sites. Therefore, the total Gibbs energy of formation numbers of n_v new sites is

$$\Delta G = n_v(\Delta H - T\Delta S_{vib}) - T\Delta S_{config} \qquad \textbf{Equation 2-2}$$

The total configuration enthalpy can be calculated by thermodynamic probability W

$$\Delta S_{config} = k\ln W \qquad \textbf{Equation 2-3}$$

The thermodynamic probability W describes the n_v vacancies distributing on the total numbers of sites $N + n_v$, which gives

$$W = \frac{(N + n_v)!}{N!\, n_v!} \qquad \textbf{Equation 2-4}$$

Because of the large number of the N and n_v, Stirling's approximation ($\ln x = x\ln x - x$ for $x \gg 1$) can be used to simplify the equation

$$\Delta S_{config} = k\left(N\ln + n_v \ln \frac{N + n_v}{n_v}\right) \qquad \textbf{Equation 2-5}$$

At equilibrium, the derivative of ΔG with respect of n_v should be zero, so the resulting expression is

$$\frac{d\Delta G}{dn_v} = (\Delta H - T\Delta S_{vib}) + kT\ln \frac{n_v}{n_v + N} = 0 \qquad \textbf{Equation 2-6}$$

The term $\frac{n_v}{n_v+N}$ means the concentration of the vacancy in the vacancy formation reaction $E_E = V_E + E_E$, so the expression of the vacancy concentration gives

$$K_v = X = \frac{n_v}{n_v + N} = \exp\left(\frac{\Delta S_{vib}}{k}\right)\exp\left(\frac{-\Delta H}{kT}\right) \qquad \textbf{Equation 2-7}$$

where K_v is the equilibrium constant in the vacancy formation reaction, X is the site fraction of vacancy in the crystal lattice.

2.1.5. Hydration thermodynamics in proton conducting pyrochlores

In pyrochlore related materials, some structural oxygen interstitial sites and oxygen vacancies can form after acceptor doping. The oxygen vacancies in pyrochlore can be hydrated to form protonic defects throughout the lattice by the following hydration reaction:

$$O_O^X + V_O^{2\bullet} + H_2O = 2OH_O^\bullet \qquad \textbf{Equation 2-8}$$

The equilibrium constant K_{hydr} can be expressed by thermodynamic constants, its hydration enthalpy ΔH_{hydr}^0 and hydration entropy ΔS_{hydr}^0

$$K_{hydr} = \exp\left(-\frac{\Delta G_{hydr}^0}{RT}\right) = \exp\left(\frac{\Delta S_{hydr}^0}{RT}\right)\exp\left(-\frac{\Delta H_{hydr}^0}{RT}\right) \qquad \textbf{Equation 2-9}$$

In principle, the hydration reaction is an exothermic reaction which indicates that protons tend to predominate at low temperatures while the concentration of oxygen ions becomes significantly large at high temperature. Therefore, this reaction can be used to predict the concentration of protons in oxides.

2.2. Defects in $Ln_2Ce_2O_7$

By examining the relative influence of Ca mole fraction on the ionic conduction, one may, with the assistance of the appropriate defect model, extract the value of the intrinsic disorder as previously done in the system $Ln_2Ce_2O_7$.

At low oxygen partial pressures, reduction may predominate

$$O_{\frac{7}{8}O}^{\frac{1}{4}/} = V_{\frac{7}{8}O}^{\frac{7}{4}\bullet} + 2e^{/} + \frac{1}{2}O_2(g) \qquad \textbf{Equation 2-10}$$

$$K_{red}{}^{/} = \frac{X_{V_{\frac{7}{8}O}^{\frac{7}{4}\bullet}}}{X_{O_{\frac{7}{8}O}^{\frac{1}{4}/}}} n^2 pO_2^{\frac{1}{2}} = \left(\frac{\left[O_{\frac{7}{8}O}^{\frac{1}{4}/}\right]}{\left[O_{\frac{7}{8}O}^{\frac{1}{4}/}\right] + \left[V_{\frac{7}{8}O}^{\frac{7}{4}\bullet}\right]}\right)\left(\frac{\left[V_{\frac{7}{8}O}^{\frac{7}{4}\bullet}\right]}{\left[V_{\frac{7}{8}O}^{\frac{7}{4}\bullet}\right] + \left[O_{\frac{7}{8}O}^{\frac{1}{4}/}\right]}\right)^{-1} n^2 pO_2{}^{\frac{1}{2}}$$

$$K_{red}{}^{/} = \left[O_{\frac{7}{8}O}^{\frac{1}{4}/}\right]\left[V_{\frac{7}{8}O}^{\frac{7}{4}\bullet}\right]^{-1} n^2 pO_2^{\frac{1}{2}}$$

Here $\left[O_{\frac{7}{8}O}^{\frac{1}{4}/}\right] + \left[V_{\frac{7}{8}O}^{\frac{7}{4}\bullet}\right]$ represents the site occupation in terms of molar fraction for $Ln_2Ce_2O_7$

$$\left[O_{\frac{7}{8}O}^{\frac{1}{4}/}\right] + \left[V_{\frac{7}{8}O}^{\frac{7}{4}\bullet}\right] = 8 \qquad \textbf{Equation 2-11}$$

Therefore, the fraction of the concentration of defects will be directly expressed by the concentration in the equations. Assuming that electrons are the minority defects, such relation can be derived

$$\left[O_{\frac{7}{8}O}^{\frac{1}{4}/}\right] = 7\left[V_{\frac{7}{8}O}^{\frac{7}{4}\bullet}\right] \qquad \textbf{Equation 2-12}$$

$$\left[e^{/}\right] = \left(7K_r{}^{/}\right)^{\frac{1}{2}}(PO_2)^{-\frac{1}{4}} \qquad \textbf{Equation 2-13}$$

Similarly, oxidation will predominate under high oxygen partial pressures, which is written as follow

$$\frac{1}{2}O_2(g) + V_{\frac{7}{8}O}^{\frac{7}{4}\bullet} = 2h^{\bullet} + O_{\frac{7}{8}O}^{\frac{1}{4}/} \qquad \textbf{Equation 2-14}$$

$$K_{ox}{}^{/} = \left[V_{\frac{7}{8}O}^{\frac{7}{4}\bullet}\right]^{-1}\left[O_{\frac{7}{8}O}^{\frac{1}{4}/}\right] p^2 pO_2^{-\frac{1}{2}} \qquad \textbf{Equation 2-15}$$

In this case, electron holes are assumed to be minority defects, the electroneutrality is the same as equation 2-12. The concentration of electron hole can be derived by combing equation 2-11, 2-12 and 2-15

$$[h^{\bullet}] = \left(\frac{1}{7}K_{ox}{}'\right)^{\frac{1}{2}} (PO_2)^{\frac{1}{4}} \qquad \textbf{Equation 2-16}$$

The Brouwer diagram displaying the variations in defect concentration as a function of the oxygen partial pressure is created based on the calculation. The diagram can be divided into five regions. For the extremely low oxygen partial pressures, in region 1, the concentration of oxygen vacancies is so high that the oxide can be close to metals, which is solely a theoretical limited state. Region 2 illustrates the concentration of the defects under reducing atmospheres corresponds to the equation 2-10. The concentration of oxygen vacancies and electrons increase and the negative oxygen ion decrease gradually from high to low oxygen partial pressure. In region 3, the concentration of the two oxygen defects is constant in ideal case and the logarithm concentration of electron and electron hole show -1/4 and 1/4 dependencies as a function of log pO_2, respectively. In region 4, large concentration of oxygen vacancies are oxidized to be the oxygen sites. In the region 5, as a limited state, all the oxygen vacancies disappear and there are just oxygen sites which is close to oxygen gas.

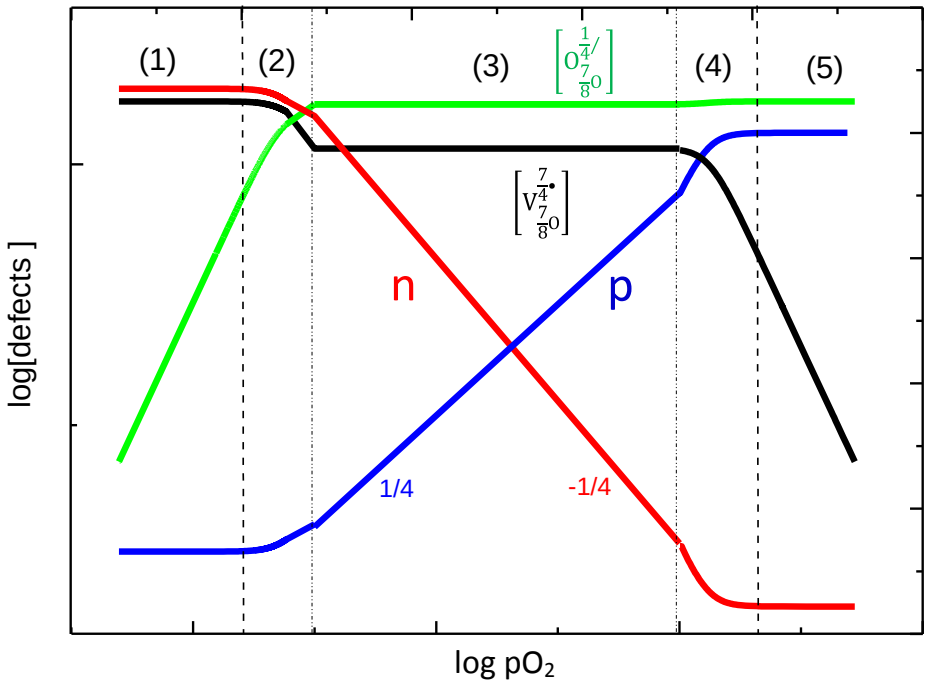

Figure 2.1 Brouwer diagram of $Ln_2Ce_2O_7$ shows logarithm concentration of defects as a function of log pO_2.

2.2.1. Defects in $Ln_{2-x}Ca_xCe_2O_{7-\delta}$

In the pyrochlore system, acceptor dopants will increase the concentration of oxygen vacancy. The acceptor may be charge compensated by oxygen vacancies and the electroneutrality will be given as

$$[\mathrm{Acc}^{/}] = 2[\mathrm{V}_{\mathrm{O}}^{\bullet\bullet}] \qquad \textbf{Equation 2-17}$$

In this thesis, Ca^{2+} is chosen to substitute Nd^{3+} and Gd^{3+} in NCO and GCO as acceptor dopants. For the disordered fluorite related materials $Nd_2Ce_2O_7$ and $Gd_2Ce_2O_7$ as the host materials, this process can be written as

$$2\mathrm{CaO} + 2\mathrm{CeO}_2 = 2\mathrm{Ce}_{\mathrm{Ce}}^{\mathrm{x}} + 2\mathrm{Ca}_{\mathrm{Ln}}^{/} + 2\mathrm{V}_{\frac{7}{8}\mathrm{O}}^{\frac{7}{4}\bullet} + 6\mathrm{O}_{\frac{7}{8}\mathrm{O}}^{\frac{1}{4}/} \qquad \textbf{Equation 2-18}$$

According to the defect reaction, the two negatively charged species, the acceptor dopant $\mathrm{Ca}_{\mathrm{Nd}}^{/}$ and oxygen sites $\mathrm{O}_{\frac{7}{8}\mathrm{O}}^{\frac{1}{4}/}$, are both compensated by the positively charged $\mathrm{V}_{\frac{7}{8}\mathrm{O}}^{\frac{7}{4}\bullet}$. The condition for the electronuetrality is

$$\frac{1}{4}\left[\mathrm{O}_{\frac{7}{8}\mathrm{O}}^{\frac{1}{4}/}\right] + \left[\mathrm{Ca}_{\mathrm{Ln}}^{/}\right] = \frac{7}{4}\left[\mathrm{V}_{\frac{7}{8}\mathrm{O}}^{\frac{7}{4}\bullet}\right] \qquad \textbf{Equation 2-19}$$

In terms of the molar fraction for $Ln_2Ce_2O_7$, the overall oxygen occupancy is same as equation 2-11. Since the positively charged oxygen vacancy is initially compensated by negatively charged oxygen ions, the addition of the extrinsic negatively charged doping will lead to transforming some negative oxygen sites to positive oxygen vacancies. Therefore, the Brouwer diagram for the $Ln_2Ce_2O_7$ with dopant should be similar like that for $Ln_2Ce_2O_7$, which is drawn as

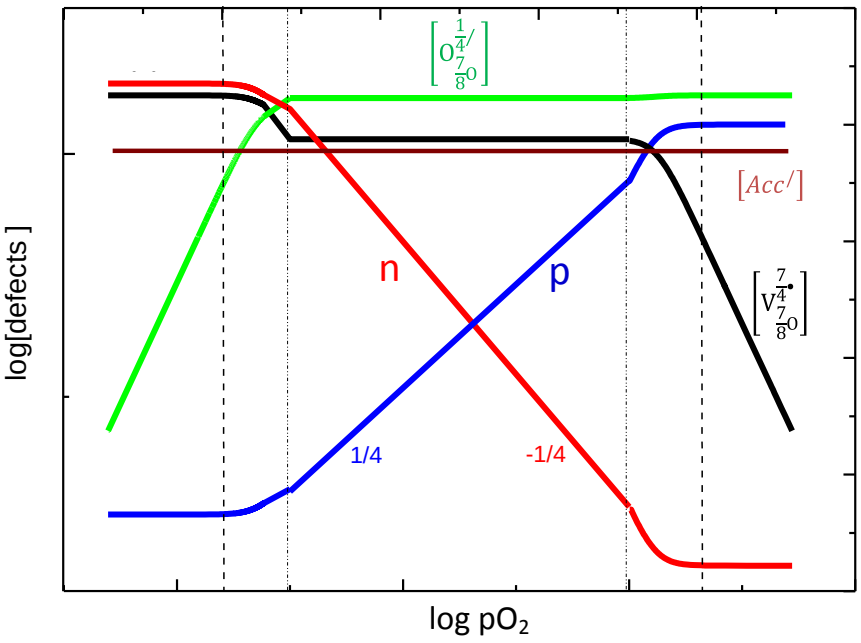

Figure 2.2 Brouwer diagram of $Ln_{2-x}Ca_xCe_2O_{7-\delta}$ shows logarithm concentration of defects as a function of log pO_2.

2.2.2. Protons in $Ln_2Ce_2O_7$

Materials with oxygen vacancies can be hydrated and by formation of protons as follow

$$H_2O + V_O^{\bullet\bullet} + O_O^X = 2OH_O^{\bullet} \qquad \textbf{Equation 2-20}$$

Disordered fluorite related materials $Nd_2Ce_2O_7$ and $Gd_2Ce_2O_7$ may also react with water due to the large amount of intrinsic oxygen vacancies. Hydration of the $Ln_2Ce_2O_7$ can be written as follow:

$$H_2O + V_{\frac{7}{8}O}^{\frac{7}{4}\bullet} + O_{\frac{7}{8}O}^{\frac{1}{4}/} = 2OH_{\frac{7}{8}O}^{\frac{3}{4}\bullet} \qquad \textbf{Equation 2-21}$$

The equilibrium constant of the hydration reaction is derived as

$$K_H = \frac{\left[OH_{\frac{7}{8}O}^{\frac{3}{4}\bullet}\right]^2}{\left[V_{\frac{7}{8}O}^{\frac{7}{4}\bullet}\right]\left[O_{\frac{7}{8}O}^{\frac{1}{4}/}\right] p_{H_2O}} \qquad \textbf{Equation 2-22}$$

The total oxygen sites occupancy now reads

$$\left[OH_{\frac{7}{8}O}^{\frac{3}{4}\bullet}\right] + \left[V_{\frac{7}{8}O}^{\frac{7}{4}\bullet}\right] + \left[O_{\frac{7}{8}O}^{\frac{1}{4}/}\right] = 8 \qquad \textbf{Equation 2-23}$$

And the electroneutrality relation is given as

$$\frac{3}{4}\left[OH_{\frac{7}{8}O}^{\frac{3}{4}\bullet}\right] + \frac{7}{4}\left[V_{\frac{7}{8}O}^{\frac{7}{4}\bullet}\right] = \frac{1}{4}\left[O_{\frac{7}{8}O}^{\frac{1}{4}/}\right] \qquad \textbf{Equation 2-24}$$

Assuming that the proton is in the minority, $\left[OH_{\frac{7}{8}O}^{\frac{3}{4}\bullet}\right] \ll \left[V_{\frac{7}{8}O}^{\frac{7}{4}\bullet}\right]$, the site of the oxygen vacancies and oxygen ions then read

$$\left[V_{\frac{7}{8}O}^{\frac{7}{4}\bullet}\right] = 1 \quad \left[O_{\frac{7}{8}O}^{\frac{1}{4}/}\right] = 7 \qquad \textbf{Equation 2-25}$$

Proton concentration as a function of water vapor partial pressure is

$$\left[OH_{\frac{7}{8}O}^{\frac{3}{4}\bullet}\right] = (7K_H)^{\frac{1}{2}} P_{H_2O}{}^{\frac{1}{2}} \qquad \textbf{Equation 2-26}$$

As the material is hydrated, the concentration of oxygen vacancy will be so small that protons take over as the major defect $\left[OH_{\frac{7}{8}O}^{\frac{3}{4}\bullet}\right] \gg \left[V_{\frac{7}{8}O}^{\frac{7}{4}\bullet}\right]$. The concentration of defects is

$$\left[OH_{\frac{7}{8}O}^{\frac{3}{4}\bullet}\right] = 2 \quad \left[O_{\frac{7}{8}O}^{\frac{1}{4}/}\right] = 6 \qquad \textbf{Equation 2-27}$$

Then the relationship between the concentration of oxygen vacancies and water vapor partial pressure is

$$\left[V_{\frac{7}{8}O}^{\frac{7}{4}\bullet}\right] = \frac{2}{3} K_H^{-1} P_{H_2O}{}^{-1} \qquad \textbf{Equation 2-28}$$

The Brouwer diagram can be drawn based on these calculations, as shown in Figure 2.3.

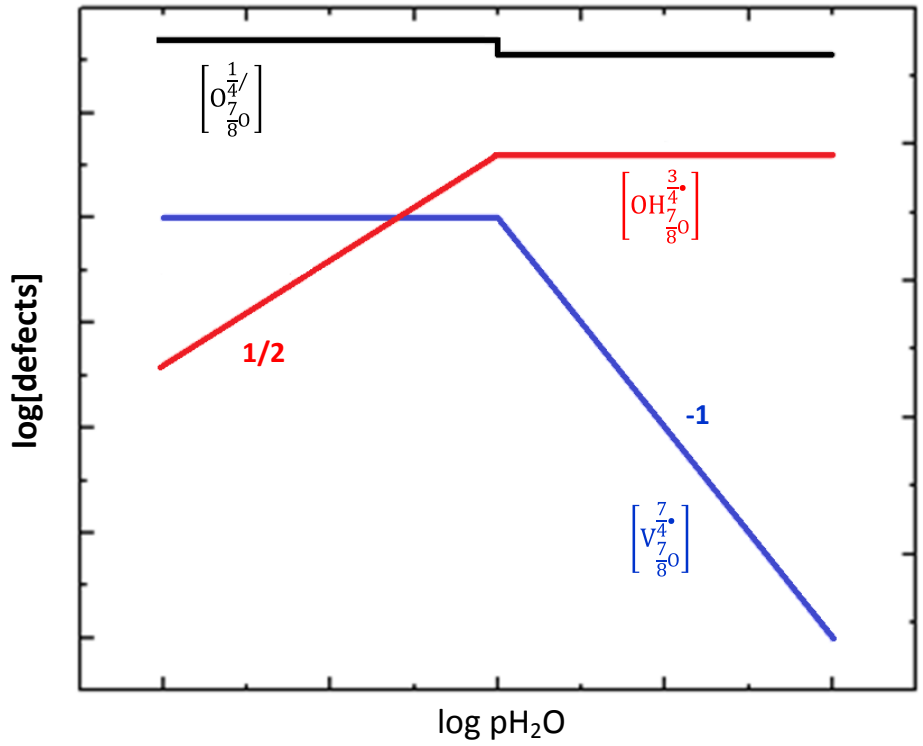

Figure 2.3 Brouwer diagram of $Ln_2Ce_2O_7$ about logarithm defect concentration as a function of log pH_2O.

2.2.3. Protons in $Ln_{2-x}Ca_xCe_2O_{7-\delta}$

The electrical neutrality condition of $Ln_{2-x}Ca_xCe_2O_{7-\delta}$ under wet conditions is

$$\frac{3}{4}\left[OH_{\frac{7}{8}O}^{\frac{3}{4}\bullet}\right] + \frac{7}{4}\left[V_{\frac{7}{8}O}^{\frac{7}{4}\bullet}\right] = \frac{1}{4}\left[O_{\frac{7}{8}O}^{\frac{1}{4}/}\right] + \left[Ca_{Nd}^{/}\right] \qquad \textbf{Equation 2-29}$$

The sum of the number of the anion sites is accord to equation 2-23 and the chemical equilibrium constant is the same form as equation 2-22. The acceptor dopant will make a role as slightly modifying the ratio between the oxygen ion and oxygen site and the Brouwer

diagram should be similar as that for the undoped samples, as shown in Figure 2.4. The concentration of the protons can be calculated by combining equation 2-27, 2-28, and 2-29

$$\left[OH_{\frac{7}{8}O}^{\frac{3}{4}\bullet}\right] = \frac{-4P_{H2O}K_H + \sqrt{(4P_{H2O}K_H)^2 - P_{H2O}K_H(P_{H2O}K_H - 4)(3[Acc/] - 0.25[Acc/]^2 + 7)}}{2 - 0.5P_{H2O}K_H} \quad \textbf{Equation 2-30}$$

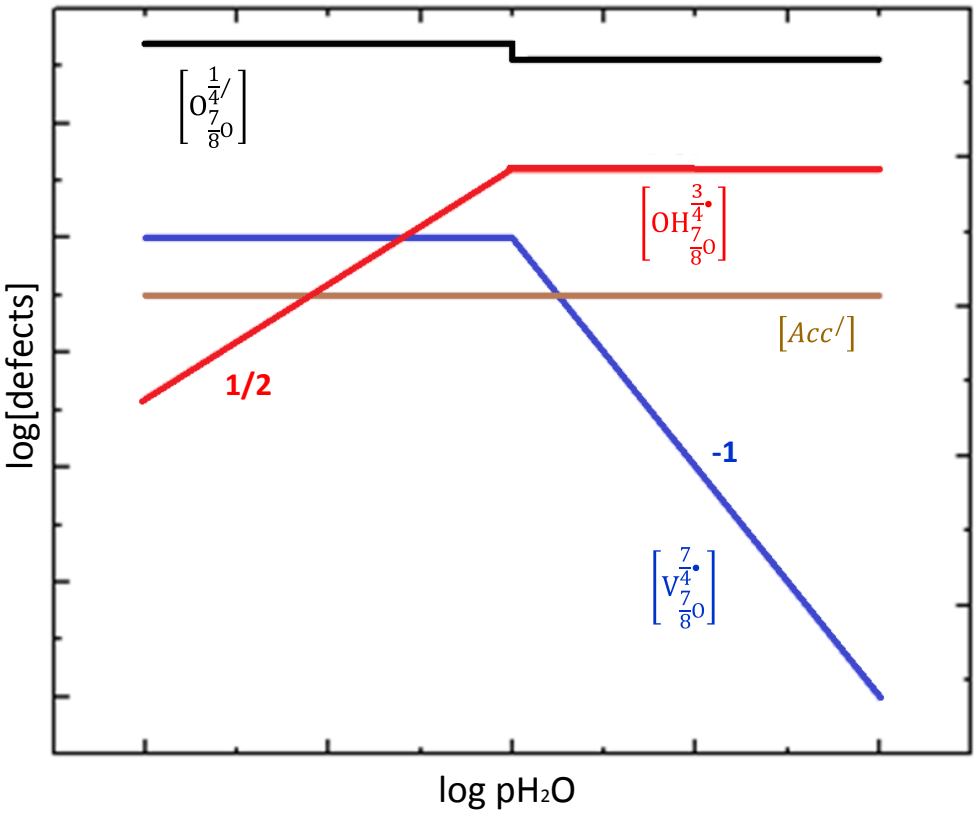

Figure 2.4 Brouwer diagram about the logarithm defect concentration vs. log pH_2O in $Ln_{2-x}Ca_xCe_2O_{7-\delta}$

The concentration of protons in oxides can be calculated by the change of pH_2O based on the reaction, the water uptake can be directly measured by thermogravimetry. Standard molar hydration thermodynamic parameters of disordered fluorite can be calculated by fitting the thermogravimetry data by equation 2-30.

2.3. Diffusion

In polycrystalline materials, diffusion will happen in the lattice due to the presence of defects. Diffusion can happen along line and surface defects like grain boundaries, inner or outer surfaces of pores or cracks etc. Diffusion along two dimensional defects like surface is usually faster than diffusion through the lattice because of the high diffusivity or short diffusion lengths. The diffusion behavior includes self-diffusion, tracer diffusion, ambipolar

diffusion and chemical diffusion etc. In this work, some charge carriers like oxygen ions and protons diffuse as point defects, but some other charge carriers exhibit the diffusion along the inner surface of the sample, such as hydronium ions. Diffusion mechanisms will be discussed in Chapter 6.

2.3.1. Diffusion coefficient

For the random diffusion, the diffusion coefficient depends on jump distance s and the number of jumps per unit time Γ, which can be expressed

$$D = \frac{1}{6} s^2 \Gamma \qquad \textbf{Equation 2-31}$$

Γ is determined by some factors such as jump frequency ω; N_d denotes the number of site can be jumped to; Z represents the number of the nearest sites. Hence, Γ gives

$$\Gamma = N_d Z \omega \qquad \textbf{Equation 2-32}$$

The diffusion coefficient D in a cubic structure in this work can be written

$$D = \alpha a_0 \omega N_d \qquad \textbf{Equation 2-33}$$

where α is the geometrical factor depends on the crystal structure, $a_0$is the lattice parameter. The defect concentration N_d can be expressed by the defect formation enthalpy ΔH_d and formation entropy ΔS_d, which gives

$$N_d = \exp\left(\frac{-G_d}{RT}\right) = \exp\left(\frac{\Delta S_d}{R}\right) \exp\left(-\frac{\Delta H_d}{RT}\right) \qquad \textbf{Equation 2-34}$$

Atoms keep shaking and vibrating in their sites among the lattice due to the internal energy. If an atom can leave its site and move freely, it needs sufficient energy to jump beyond the energy barrier. Zener (1951, 1952) described the complex activated process based on a system includes an initial equilibrium condition and an activated condition at the top of the energy barrier. The rate of transition between the two states can be written

$$\omega = \gamma \exp\left(\frac{\Delta S_m}{R}\right)\left(-\frac{\Delta H_m}{RT}\right) \qquad \textbf{Equation 2-35}$$

where γ , $\Delta S_m, \Delta H_m$ are Debye frequency (10^{13}Hz), entropy and enthalpy of the activated process, respectively. The diffusion coefficient D can be derived based on combining equation 2-33, 2-34, and 2-35

$$D = \alpha a_0 \gamma \exp\left(\frac{\Delta S_d + \Delta S_m}{R}\right) \exp\left(-\frac{\Delta H_d + \Delta H_m}{RT}\right) \quad \textbf{Equation 2-36}$$

2.4. Electrical conductivity

In oxides, the charge carriers will diffuse under driving forces such as electrical potential and chemical potential. Once electrical potential gradient is in the oxides, the charge carriers will undergo an electrical force which is proportional to the electrical field and the charge number of the species. The force can be written as

$$F = -z_i e \frac{d\varphi}{dx} = z_i e E \quad \textbf{Equation 2-37}$$

where F denotes the electrical force, and E is the electric field. The flux of the particle depends on the defect concentration C_i, the particle mobility B and the electrical force F. So the flux is

$$j = C_i B_i F = z_i e B_i C_i E \quad \textbf{Equation 2-38}$$

The net current density arising from the force reads

$$i = z_i e j_i = (z_i e)^2 z_i C_i e \quad \textbf{Equation 2-39}$$

The mobility of the species μ_i is proportional to B_i, which gives

$$\mu_i = B_i z e \quad \textbf{Equation 2-40}$$

The equation 2-41 can be derived by combining equation 2-38 and equation 2-39

$$i = z_i e C_i \mu_i E = \sigma_i E \quad \textbf{Equation 2-41}$$

where $\sigma_i = z_i e C_i \mu_i$ represents the conductivity of the charge carrier with unit of Scm^{-1} in this work. The ratio of the partial conductivity of some species σ_i divided by the total conductivity σ_{tot} is denoted by the transport number of the species, i:

$$t_i = \frac{\sigma_i}{\sigma_{tot}} \quad \textbf{Equation 2-42}$$

The transport number of a particular charge carrier is between 0 and 1 and the sum of all the transport number is always equal to 1.

2.4.1. Nernst-Einstein relation

The relationship between the diffusion coefficient and mechanical mobility is

$$D = BTk \qquad \textbf{Equation 2-43}$$

Nernst-Einstein equation can be derived by combining equation 2-40 and 2-43

$$D_i = BTk = \frac{\mu Tk}{z_i e} = \sigma_i \frac{Tk}{c_i (z_i e)^2} \qquad \textbf{Equation 2-44}$$

Furthermore, when a charge carrier moves through a polar oxide, they will polarize the surrounding neighbors and lead to a local distortion of the structure. Such charge carriers are called polarons. For the large polaron, the interaction between the electronic defects and surrounding lattice is so weak that electrons are quite delocalized. Large polarons can be found in some highly ionic non-transition metal oxides whose band gap is over 6eV. The dimension of a small polaron is smaller than the lattice parameter. Unlike the large polaron, the electronic defects strongly interact with the lattice which is localized. Due to the strong interaction between the small polaron and the surrounding lattice, their mobility increases with increasing temperature. The small polaron follows the traditional diffusion mechanism and its electrical conductivity can be expressed by the Nernst-Einstein equation as follow

$$\sigma_i = \frac{D_i c_i (z_i e)^2}{Tk} \qquad \textbf{Equation 2-45}$$

The expression of the conductivity are derived by combing equation 2-36 and 2-45

$$\sigma_i = \frac{\alpha a_0 \gamma c_i (z_i e)^2}{Tk} \exp\left(\frac{\Delta S_d + \Delta S_m}{R}\right) \exp\left(-\frac{\Delta H_d + \Delta H_m}{RT}\right) \qquad \textbf{Equation 2-46}$$

The expression of the small polaron in this work can be written as a Arrhenius's equation as

$$\sigma_i = \frac{\sigma_0}{T} \exp\left(-\frac{E_a}{RT}\right) \qquad \textbf{Equation 2-47}$$

where σ_0 is the pre-exponential factor of conductivity, E_a is the activation energy of the conductivity including the defect formation enthalpy and enthalpy of defect mobility.

2.4.2. Isotope effect

In proton conducting oxides, the conductivity in D_2O or D_2 is always lower than that in H_2O and H_2 .This phenomenon is called isotope effect and is related to the difference in mass between H and D. For a proton conductor, the protons form bonds with the oxygen ions and

the stretching frequency of the bonds depends on the mass. Zener vividly described the stretching of the bonds by a spring. The stretching frequency γ gives

$$\gamma = \frac{\alpha}{a}\sqrt{\frac{\Delta H_m}{M}} \qquad \textbf{Equation 2-48}$$

Where α denotes a structure and mechanism factor, a represents the lattice parameter, M is the reduced mass of the oscillator. From equation 2-36 and equation 2-44, we know that the mobility is proportional to the frequency. For H-O and D-O bond, the ratio between the conductivity can be derived based on equation 2-48

$$\frac{\sigma_{H+}}{\sigma_{D+}} = \frac{\gamma_{H+}}{\gamma_{D+}} = \sqrt{\frac{M_{D+}}{M_{H+}}} = \sqrt{2} = 1.414 \qquad \textbf{Equation 2-49}$$

2.5. Electrochemical Impedance Spectroscopy

Electrochemical Impedance Spectroscopy is a useful technique applied in characterization of the electrical properties of electroceramics. The technique makes it possible to specifically study the electrical behavior of grain interior and grain boundaries in polycrystalline materials. Also, it can also distinguish the contribution from the electrode and determine the rate limiting electrochemical process in the electrodes.

2.5.1. Alternating current

In measurement based on direct current (DC) methods, the applied voltage and the resulting current are always constant. In contrast to measurements applying alternating current (AC), both the voltage and current vary as a function of time. Once a sinusoidal voltage is applied on the two electrodes of the sample, a sinusoidal current response can be observed. The sinusoidal voltage can be described by the frequency f, angular frequency $\omega = 2\pi f$, and the amplitude U_0. The corresponding current can be the same angular frequency as voltage, but different amplitudes and phase angles ωt. However, due to the capacitive or inductive circuit elements, the current will exhibit a phase shift θ. The voltage and the current can be characterized as follow

$$U = U_0 \sin\omega t \qquad \textbf{Equation 2-50}$$

$$I = I_0 \sin(\omega t + \theta) \qquad \textbf{Equation 2-51}$$

2.5.2. Passive electrical circuit elements

When alternating current flows through a material, it will be affected by the microstructure. As far as a polycrystalline material, the grains are divided by a large numbers of grain boundaries. The material and electrodes are also separated by several interfaces as well. These components can be charged and they can impede the transport of charge carriers, accordingly, show resistance effects, capacitance effects and inductance effects. Therefore, three passive electrical circuit elements, the resistance, R, the inductance, L, and capacitance, C, are introduced to describe the electrical response from the microstructure.

Resistor

A resistor is the element which can transport charge carriers in the long range where mobile charge carriers give rise to the electrical conductance G and resistance R=1/G. If a voltage is applied on the resistor, a current will flow through it at once. Generally, the impedance Z applied by an alternating current can be expressed as

$$Z = R = \frac{U}{I} = \frac{U_0 \sin\omega t}{I_0 \sin(\omega t)} = \frac{U_0}{I_0} \qquad \textbf{Equation 2-52}$$

Capacitor

Capacitor is formed by an ideal insulator between two conductions. A capacitor is typically described as two parallel conducting plates separated by insulating air. Once a voltage applied on the two plates, the capacitor can be charged. The capacitance of a capacitor can be calculated as

$$C = \varepsilon_0 \varepsilon_r \frac{A}{d} \qquad \textbf{Equation 2-53}$$

where $\varepsilon_0$is the vacuum permittivity $\varepsilon_0 \approx 8.854 \times 10^{-14}\ \mathrm{Fcm^{-1}}$, d is the distance between the two parallel plates, A denotes the area of one plate, and ε_r represents the relatively static permittivity of the insulating medium between the plates, as far as vacuum $\varepsilon_r = 1$. The capacitance can also be determined by the charge on the capacitor, which gives

$$I = \frac{dQ}{dt} C \frac{dU}{dt} = C \frac{d(U_0 \sin\omega t)}{dt} = \omega C U_0 \cos\omega t = \omega C U_0 \sin(\omega t + \frac{\pi}{2}) \qquad \textbf{Equation 2-54}$$

Therefore, the phase angle of current over the capacitor is $\frac{\pi}{2}$ larger than that of voltage. The capacitance resistance is defined as the ratio between the peak voltage and peak current, which gives as

$$R_C = \frac{1}{\omega C}$$ **Equation 2-55**

The peak resistance is inversely dependent of the frequency of the AC.

Inductor

In contrast to the capacitor as an ideal insulator in the circuit, the inductor is considered as an ideal conductor without any resistance. When an AC voltage is applied on the inductor, the voltage can be given as

$$U = -U_L = L\frac{dI}{dt} = L\frac{d(I_0 \sin(\omega t))}{dt} = \omega L I_0 \cos(\omega t) = \omega L I_0 \sin(\omega t + \frac{\pi}{2})$$ **Equation 2-56**

The voltage applied on the capacitor is $\frac{\pi}{2}$ phase angle more than the current. The resistance of the inductor can be given as

$$R_L = \omega L$$ **Equation 2-57**

2.5.3. Impedance and impedance sweeps

Impedance is a more general expression for what we have called resistance up to now. Generally, AC and DC are included in the impedance which is the ratio between voltage and current, and its unit is ohm. In the AC, the impedance also follows the ohm law, which gives as the ratio between the voltage and the current (cf. equation 2-50, 2-51)

$$Z = \frac{U}{I} = \frac{U_0 \sin\omega t}{I_0 \sin(\omega t + \theta)}$$ **Equation 2-58**

There are two components in the current. One component in current is in phase with the voltage and the other one is 90° degrees deviations out of the phase. Therefore, the impedance is divided into two parts. One part is the in phase part (real part R) which is the voltage divided by the in-phase component, which reflects the resistance of charge carriers pass through the impedance elements; the other part is 90° out of phase (imaginary part X), which reflects the charge carriers not really transport through the impedance. A total impedance is described by a two-dimensional vector with real and imaginary parts, as shown in Figure 2.5

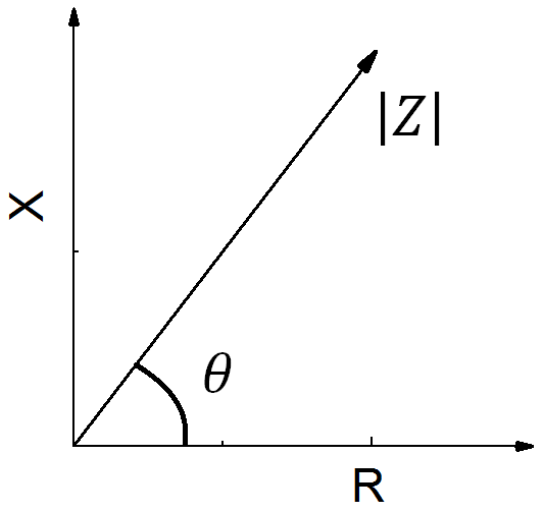

Figure 2.5 Complex impedance, x axis is the real part; y axis is the imaginary part

In Figure 2.5, the vector Z with the phase shift angle θ represents the impedance for the sample and the impedance can be expressed [12]:

$$Z^*(w) = Z' + jZ'' = Z(Re) + jZ(Im) = R + jX \quad \left(j = \sqrt{-1}\right) \qquad \textbf{Equation 2-59}$$

In the impedance measurement, the sweep can be plotted the real part of the impedance and the negative imaginary part from the maximum frequency to minimum frequency, which is also called Nyquist plot within resistance R versus negative reactance –X. Under alternating current, the response from the sample can be described by a model equivalent circuit which consists of passive electrical circuit elements. A typical way to simulate a process in the sample is to use resistor and capacitor in parallel, expressed as (RC). In a Nyquist plot, the (RC) circuit element corresponds to a perfect semicircle from the impedance spectra whose peak frequency gives as

$$\omega = \frac{1}{RC} = \frac{A}{L\rho}\frac{L}{\varepsilon_0\varepsilon_r A} = \frac{\sigma}{\varepsilon_0\varepsilon_r} \qquad \textbf{Equation 2-60}$$

Nevertheless, the microstructure is fairly complicated in a real crystalline material. The size and orientation of grains are different and some of grain boundaries are distorted. Therefore, the corresponding parts of these practical elements in the impedance should be more or less different from those from the ideal passive elements. Actually, the impedance spectra measured on real samples always exhibit depressed semicircles in the Nyquist plot, as shown in Figure 2.6a. In this case, a compatible constant phase element (CPE or Q) is introduced to describe this non-ideal case by defining two parameters n and Y whose admittance is written as

$$Y = Y_0(j\omega)^n = Y_0\left[\omega^n \cos\left(\frac{n\pi}{2}\right) + i\omega \sin\left(\frac{n\pi}{2}\right)\right] \quad \textbf{Equation 2-61}$$

By this equation, the ideal passive electrical element can be expressed when n=1,-1, 0, which is summarized in Table 2.3. Similarly, the impedance based on this equation can be derived as

$$Z_Q = [Y(j\omega)^n]^{-1} \quad \textbf{Equation 2-62}$$

Moreover, the capacitance of each (RQ) equivalent circuit is calculated as

$$C = Y^{\frac{1}{n}} R^{\frac{n-1}{n}} \quad \textbf{Equation 2-63}$$

Table 2.3 Passive electrical element in different values of n

n	Passive electrical elements	CPE
1	Pure capacitor	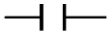
-1	inductor	
0	Resistor	
0.5	Warburg element	N/A

Nyquist diagrams generally consist of several semicircles which represent different parts from the microstructures of the specimen, typically the grain interior, grain boundary and electrodes. Figure 2.6b displays an ideal impedance spectrum from a polycrystalline material. The sweep is composed of three semicircles from high to low frequency, corresponding to bulk, grain boundary and electrode, respectively. Actually, most of the impedance spectra in this work just contain some parts of this ideal case. Since the samples are ceramics, resistances of grain and grain boundaries are affected by the temperature. Therefore, the frequency corresponds to the grain and grain boundaries vary due to equation 2-60. Actually, some semicircles can appear or vanish when the temperature changes a lot. On the other hand, the grain boundaries of some materials do not contribute too much to the resistance, the semicircle for the grain boundaries cannot be detected from the impedance spectra.

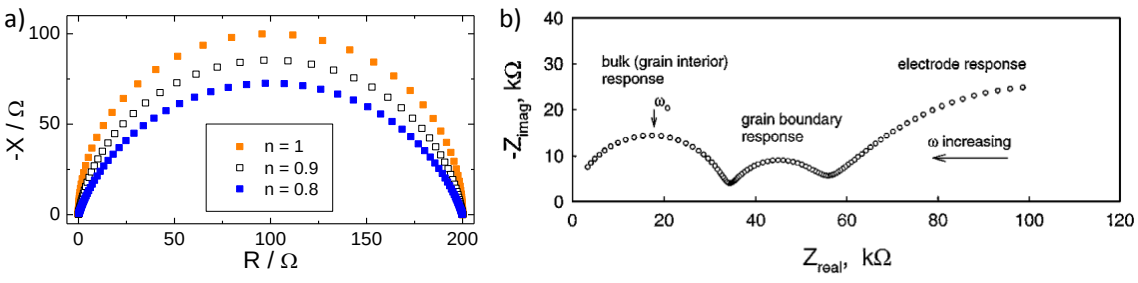

Figure 2.6 a) The shape of vary Nyquist plots [12] b) a typical impedance spectra from a polycrystalline ceramic [13].

2.5.4. Brick layer model

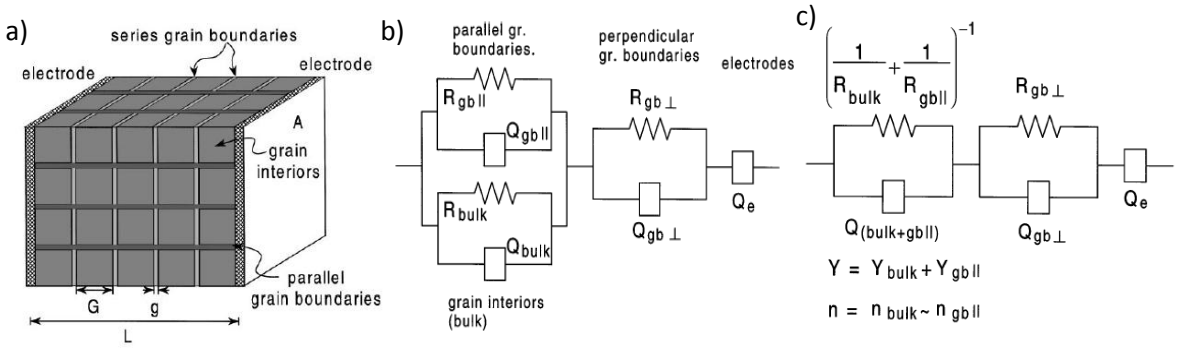

Figure 2.7 a) A polycrystalline material simulated by the "Brick layer model" whose grains are assumed to be cubic-shaped brick b) equivalent of circuit model of a polycrystalline material with the brick layer microstructure and grain boundary to exist as flat layers between grains c) simplified equivalent circuit without parallel grain boundaries [13].

The microstructure in polycrystalline materials can be described by the brick layer model. In the brick layer model, the polycrystalline material is considered as cubic-shaped grains separated by the grain boundaries. Along the electrical field, grain boundaries are not only in series but also parallel to each other, showed in Figure 2.7 a. The geometric parameter of grains and grain boundaries, "L" represents the sample length; "A" means the sample cross section area, and "g" is the width of grain boundaries. The equivalent circuit of the elements in the brick layer model is described by several parallel and series (RQ), as shown in Figure 2.7 b. The two parallel (RQ) elements correspond to the close packed bulk and parallel grain boundary. The parallel ((R_{Bulk}Q) ($R_{gb,\parallel}$Q)) can be simplified as one joint circuit element (R_1Q_1), whose resistance is $R_1 = \left(\frac{1}{R_{Bulk}} + \frac{1}{R_{gb,\parallel}}\right)^{-1}$. Apart from the bulk and parallel grain boundaries, the perpendicular grain boundaries can also be simulated as a (RQ) circuit in series with electrodes and the (R1Q1) circuit representing the sum of the bulk and parallel grain boundaries, as described in Figure 2.7 c.

Assuming that g<<G, the total length of all parallel grain boundaries are $L_\parallel$=L, and the total area of them are $A_\parallel = \frac{2g}{G}A$. Similarly, for the perpendicular grain boundaries, $L_\perp = \frac{g}{G}L$, $A_\perp$=A. The specific conductivity of an element in the circuit can be defined as $\sigma_i = \frac{L}{A}\frac{1}{R_i}$. The conductivity of sum of bulk and parallel grain boundary σ_1 and the conductivity of perpendicular grain boundaries σ_2 can be calculated as

$$\sigma_1 = \frac{2g}{G}\sigma_{gb} + \sigma_{bulk} \qquad \textbf{Equation 2-64}$$

$$\sigma_2 = \frac{G}{g}\sigma_{gb}$$ **Equation 2-65**

For a typical ceramic microstructure, like the polycrystalline materials in this work, the width of the grain interior G is estimated 100 times larger than the width of the grain boundary g. In this case, the current will not tend to pass through the pathway of the parallel grain boundaries due to the considerably small area. Therefore, most of the current will be easily conducted through the pathway of grain interior due to the large area, which gives $\sigma_1 \approx \sigma_{bulk}$. Therefore, the ratio between $\sigma_1$and σ_2 is

$$\frac{R_2}{R_1} = \frac{\sigma_1}{\sigma_2} = \frac{g}{G}$$ **Equation 2-66**

The appropriate ratio between R_1 and R_2 is between 0.01 and 100 which may show the two separate semicircles in the impedance spectra. From equation 2-60, the characteristic frequency of the bulk and grain boundary depends on dielectric constant of bulks ε_{bulk} and grain boundaries ε_{gb}.The dielectric constant of bulk and grain boundary is considered to be the same ($\varepsilon_{bulk} = \varepsilon_{gb}$) and the bulk conductivity is much higher than the grain boundary conductivity ($\sigma_1 = \sigma_2$). The frequency of bulk should be higher than that of grain boundary ($\omega_{bulk} = \omega_{gb}$). Since the parallel grain boundary part has the unfavorable geometry in the microstructure, the capacitance of this part should be so low that can be negligible. Combing equations 2-60, 2-66, the ratio between the capacitance of bulk and grain boundary gives

$$\frac{C_{Bulk}}{C_{gb}} = \frac{C_1}{C_2} = \frac{g}{G}$$ **Equation 2-67**

The conductivity of bulk, grain boundary can be calculated based on a complete sweep from high to low frequency. However, the conductance of grain boundary is comparable or higher than the bulk conductance in this work which means the resistance of the grain boundaries is so small that it cannot be discovered from the sweep.

3. Literature review

Chapter 3 consists three sections. The first section presents crystal structures with respect to the materials in this work. The next section focuses on electrical properties of materials related in this work. The last section deals with the protonic conduction in fluorite related materials at low temperatures.

3.1. Crystal structure

3.1.1. Fluorite-type oxides

Ideal fluorite was first discovered from a type of mineral with the main composition of calcium fluoride, and since then people have named those materials with the same crystal structure as CaF_2 "fluorite". The fluorite structure has a space group Fm-3m. The atomic sites can be expressed by the Wyckoff positions. As shown in Table 3.1, in the Wyckoff positions, cerium and oxygen sites are described by letters and numbers, representing the numbers of such sites in one unit cell. The geometry of fluorite is the cubic with the cations occupy equivalent 4a sites and oxygen ions positioned at an 8c sites which are coordinated by four cations, as shown in Figure 3.1. In general, fluorite related structure with space group Fm-3m is often called F-type structure. The crystal structures of the materials investigated in this work are all derivatives of fluorites.

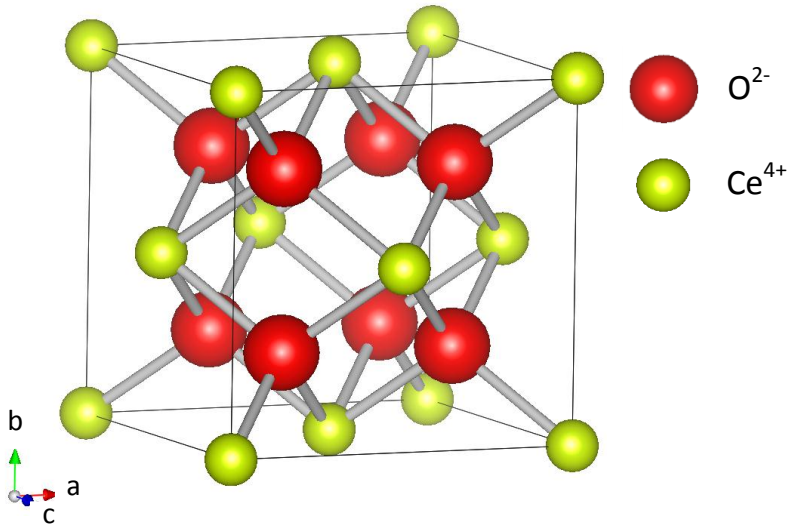

Figure 3.1 1/8 of unit cell of CeO_2 where yellow balls are Ce^{4+} ions and red balls are O^{2-} ions.

Table 3.1 The Wyckoff site symmetry of the CeO_2 in Fm-3m space group [14].

Atoms	x	y	z	Wyckoff site symmetry
Ce	0	0	0	4a
O	0.25	0.25	0.25	8c

3.1.2. Pyrochlore-type oxides

Oxides of composition $A_2B_2O_7$ often assume the pyrochlore structure type, which is also considered as a derivative of fluorite. Pyrochlore-type (P-type) oxides, which are belongs to space group Fd3m, can also be expressed $A_2B_2O_6O'$, where a bigger cation A^{3+} is coordinated by 8 oxygen ions and a smaller cation B^{4+} with coordination number of 6, as shown in Figure 3.2. The configuration of the unit cell is also face centered cubic (FCC) with the A^{4+} and B^{3+} cations orderly packing at the corns and face centers. The row of each cation species alternates along <110> direction. Oxygen ions occupy the tetrahedral sites similar as those in fluorite, but there is one structurally vacant tetrahedral site in each unit cell.

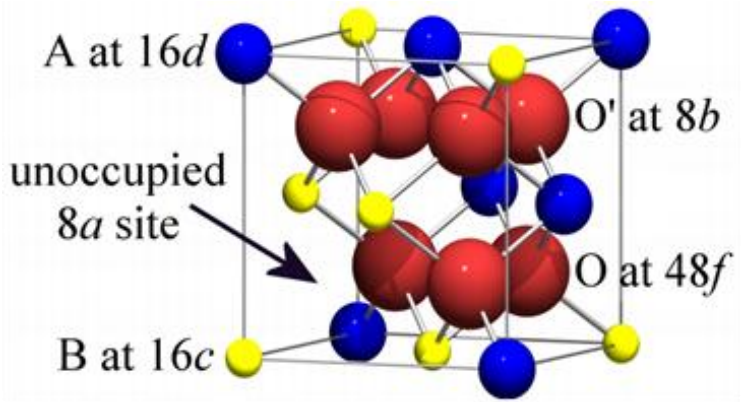

Figure 3.2 1/8 of unit cell of pyrochlore where blue spheres represent A^{3+} cations, yellow B^{4+} and red O^{2-} [15].

As summarized in Table 3.2, there are two types of oxygen sites in 1/8 of unit cell of pyrochlore. O (1) (6/7 out of the total oxygen ions) occupies the position 48f (x, 1/8, 1/8). x parameters varies from 0.3125 (perfect BO_6 octahedron and a distorted AO_8), to 0.375 (distorted BO_6 octahedral and a common AO_8 cubic). O (2) occupy the 8b site (1/7 out of the total oxygen ions) [16]. Besides 7 oxygen ions in 1/8 of unit cell, there is one 'vacant' oxygen site occurs at position 8a.

Table 3.2 The Wyckoff site symmetry of the $A_2B_2O_7$ pyrochlore in Fd3m space group [17].

Atoms	x	y	z	Wyckoff site symmetry
A	1/2	1/2	1/2	16d
B	0	0	0	16c
O(1)	X	1/8	1/8	48f
O(2)	3/8	3/8	3/8	8b

The size difference between cations on A and B sites is believed to be the driving force to stabilize the pyrochlore structure [18]. The stability of pyrochlore can be evaluated by the ratio between the radius of cations on A and B sites (r_{A3+}/r_{B4+}). The stable pyrochlore phase

requires that the ratio should be in the range of 1.46 to 1.80 [19]. A smaller ratio leads to disorder between the A^{3+} and B^{4+} cations, resulting in a disordered fluorite phase $(A,B)O_{1.75}$. The occupation of oxygen ions changes in the order-disorder transition. Due to Heremans's Rietveld refinement [20], occupation of the three oxygen sites in $Y_2Ti_2O_7$ change from 1 to 0.875 with increasing amount of substitution Zr^{4+} in the site of Ti^{4+} due to higher degree of oxygen ion disorder with the closer radii of the cations. However, the state of disorder cannot solely depend on the relative radii of the cations. For example, Wuensch's study shows that substitution of the larger Sn^{4+} ion for Ti^{4+} fails to induce a disorder in $Gd_2(Ti_xSn_{1-x})_2O_7$ [21].

Ina addition, some pyrochlore oxides exhibit order-disorder transition at different temperatures, such as 2300°C for $Nd_2Zr_2O_7$, 2200°C for $Sm_2Zr_2O_7$ and 1530°C for $Gd_2Zr_2O_7$ [21]. Pyrochlore may exhibit an order-disorder phase transition at elevated pressure, such as for $Y_2Ti_2O_7$, $Gd_2Ti_2O_7$, $Sm_2Zr_2O_7$ and $Gd_2Zr_2O_7$ [22-24]. High energy irradiation can also attribute to the order-disorder transition in pyrochlore [25].

3.1.3. C-type rare earth oxides

The sesquioxides rare earth oxides (Ln_2O_3) crystallize in three forms, A-type (hexagonal), B-type (monoclinic) and C-type (cubic) structures, according to the ionic radius of the rare earth ion [26]. Lighter elements from La to Nd exhibit A-type. Sm_2O_3 is reported to be B- type and the rest of the rare earth sesquioxides yield the C-type oxides [26]. The unit cell of a C-type rare earth oxide (Gd_2O_3) and 1/8 of the unit cell are shown in Figure 3.3 and the Wickoff site symmetry of Gd_2O_3 is summarized in Table 3.3. As shown in Figure 3.3b, C-type structure can be considered as a defective fluorite that ¼ of the oxygen atoms of stoichiometric fluorite lattice are lost. In that case, the C-type structure is close to the F-type structure with respect to the ordered vacancies.

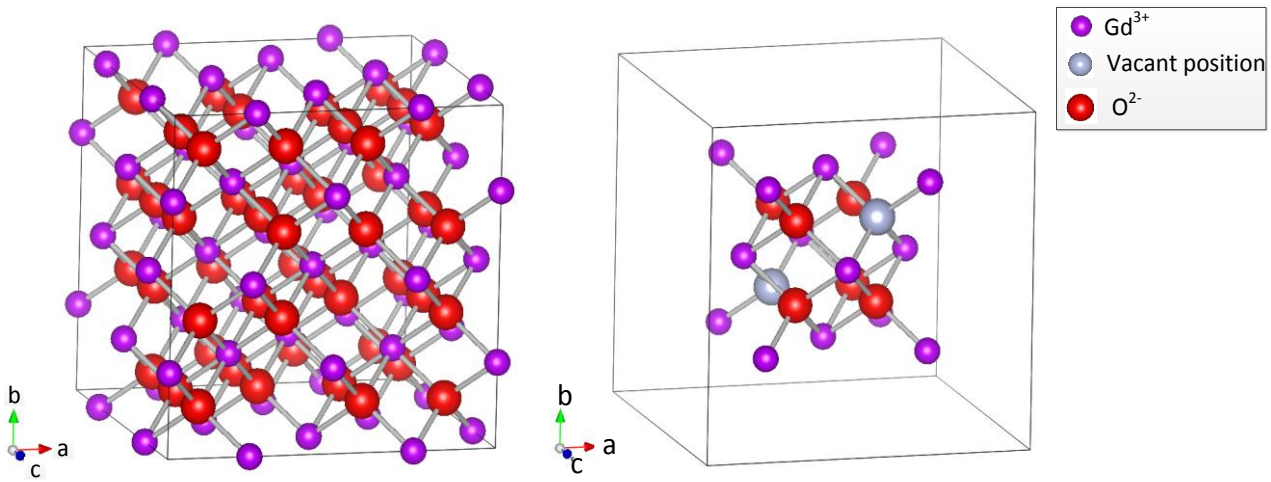

Figure 3.3 a) Unit cell of C-type Gd_2O_3 in Ia-3 space group b) 1/8 of unit cell of Gd_2O_3.

Table 3.3 The Wyckoff site symmetry of C-type Gd_2O_3 in Ia-3 space group [27].

Atoms	x	y	z	Wyckoff site symmetry
Gd1	0.25	0.25	0.25	8b
Gd2	0.97	0	0.25	24d
O	0.385	0.145	0.38	48e

It is interesting to compare the 1/8 unit cell of F-type, P-type and C-type structures. As can be seen from Figure 3.4, it is obvious that crystal structures of them are very similar and the fraction of the vacant position increases from F-type to C-type. The electrical properties of materials with these three structures will be reviewed in section 3.2.

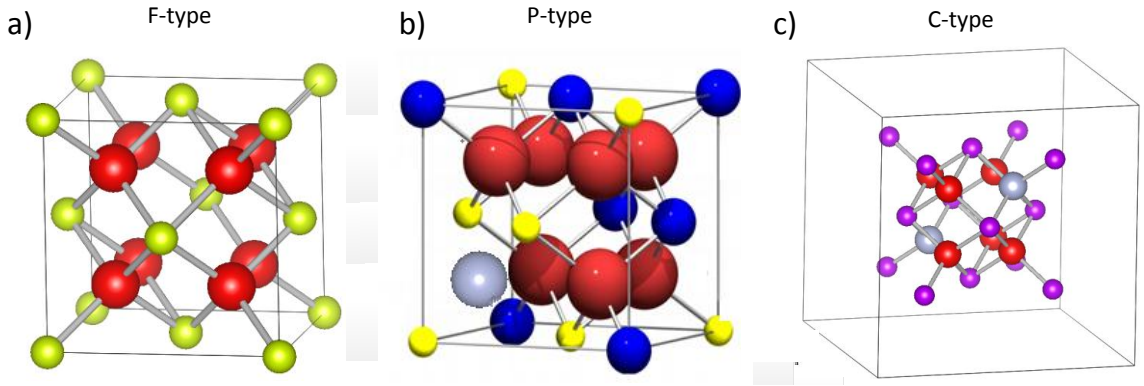

Figure 3.4 1/8 unit cell of a) F-type b) P-type c) C-type

3.1.4. Crystal structure of $Ln_2Ce_2O_7$ (Ln=lanthanides)

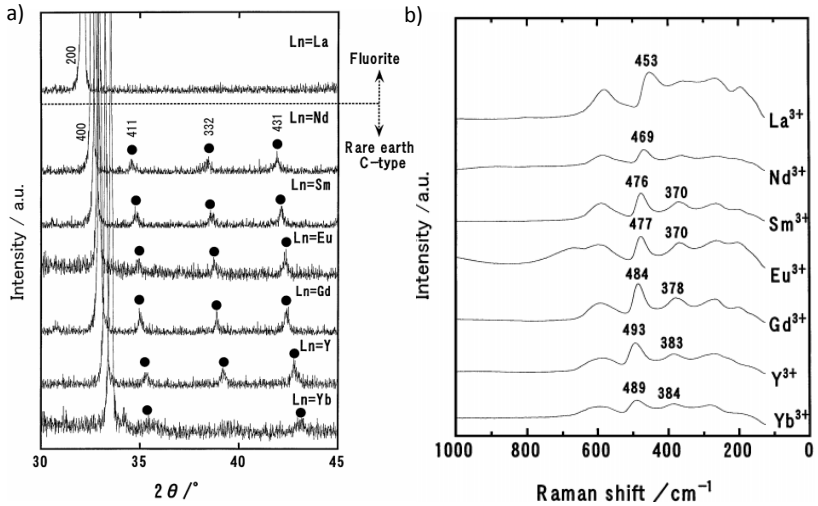

Figure 3.5 a) X-ray diffraction patterns for $Ln_2Ce_2O_7$ system [28] b) Raman spectra at room temperature for the $Ln_2Ce_2O_7$ systems [28].

Since $Nd_2Ce_2O_7$ and $Gd_2Ce_2O_7$ are the two materials studied in this work, it is interesting to first overview the crystal structure of $Ln_2Ce_2O_7$ (Ln=Lanthanides). Yamamura et al. [28] investigated $Ln_2Ce_2O_7$ (Ln=La, Nd, Sm, Eu, Gd, Y, Yb) by XRD and Raman spectra. As shown in

Figure 3.5a, the C-type superstructure is found when Yb^{3+}, Y^{3+}, Gd^{3+},Eu^{3+}, Sm^{3+}, Nd^{3+} were elements as Ln^{3+} in $Ln_2Ce_2O_7$ while only F-type one was obtained when Ln^{3+} was La^{3+}. Raman peaks (cf. Figure 3.5b) suggests all the samples has the similar local structure among the oxides. Furthmore, it was recognized for peaks for C-type in wave number range of 470-490cm^{-1} and 360-380cm^{-1} which is in accordance with XRD results.

In addition, many studies reported the crystal structure of $Ln_2Ce_2O_7$. The main phase and the lattice parameter of $Ln_2Ce_2O_7$ from the studies are summarized in Table 3.4. The lattice parameter decreases with decreasing size of lanthanides and the phase changes from F-type to C-type with decreasing lattice parameter. Tyagi et al. [10] explained the pure F type in $La_2Ce_2O_7$ and $Nd_2Ce_2O_7$ is a result of high coordination number of La^{3+} and Nd^{3+} in the lanthanide site, which is a requisition of F-type lattice. The size of the following rare earth elements decrease significantly. The lower size will attribute to lower coordination numbers and tends to stabilize the C-type phase. Also, Yamamura et al. [28] explained that the smaller Ln^{3+} will stabilize C-type phase in $Ln_2Ce_2O_7$ and the phase will exist if $r(Ln^{3+})/r(Ce^{4+})$ is smaller than 1.17.

Table 3.4 Crystal Structures of $Ln_2Ce_2O_7$ (Ln=Lanthanides).

Materials	Type of structure	Lattice parameter	Ionic size of Ln^{3+} CN=VI[29]	Expansion coefficient	Reference
$La_2Ce_2O_7$	F type	5.577	1.032	10.48	[30, 31]
$Nd_2Ce_2O_7$	F type	5.496	0.983	11.87	[30, 31]
$Sm_2Ce_2O_7$	C type	5.457	0.958	12.10	[30, 31]
$Eu_2Ce_2O_7$	C type	5.438	0.947	12.61	[30, 31]
$Gd_2Ce_2O_7$	C type	5.428	0.938	12.47	[30, 31]
$Dy_2Ce_2O_7$	F type/C type	5.397	0.923	11.77	[30, 32]
$Ho_2Ce_2O_7$	C type	5.383	0.901	11.95	[30, 31]
$Er_2Ce_2O_7$	C type	5.374	0.89	12.29	[30, 31]
$Tm_2Ce_2O_7$	F and C type	N/A	0.880	N/A	[33]
$Yb_2Ce_2O_7$	F and C type	5.364	0.868	12.32	[30, 32]
$Lu_2Ce_2O_7$	F and C type	5.370	0.890	12.45	[30, 31]

3.1.5. Crystal Structure of $Nd_2Ce_2O_7$

The crystal structure of $Nd_2Ce_2O_7$ was firstly reported to be a fluorite type oxide in the cubic space group Fm-3m [32]. Later, Liu et al. [34] confirmed that $Nd_2Ce_2O_7$ exhibits a defective fluorite-type structure from X-ray diffraction.

As shown from the unit cell in Figure 3.6a, in the face centered cubic, the cations occupy the face centers and corners with coordination number of 8. However, the two cations Nd^{3+} and Ce^{4+} randomly occupy cation sites and the statistical possibility for each cation to occupy a specific site is 50%. The average coordination number of each cation is 7. The anions will

occupy the tetrahedral sites which are coordinated by four cations. Hence, $Nd_2Ce_2O_7$ can be written as $(Nd, Ce)_4O_7$. In addition, the seven oxygen ions randomly occupy the eight tetrahedral sites which means the statistical possibility for one anion to occupy a site is 0.875. The crystal information of the F-type $Nd_2Ce_2O_7$ is summarized in Table 3.5.

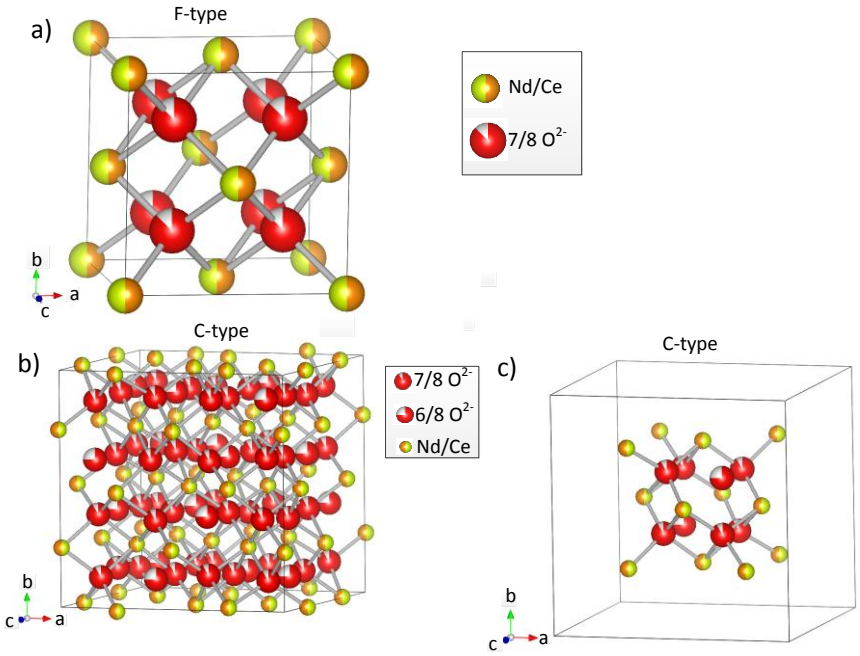

Figure 3.6 a) 1/8 unit cell of the F-type of $Nd_2Ce_2O_7$ b) unit cell of the C-type phase of $Nd_2Ce_2O_7$ c) 1/8 unit cell of the C-type of $Nd_2Ce_2O_7$.

On the other hand, based on neutron diffraction, Chakraborty et al. [35] reported that $Nd_2Ce_2O_7$ should crystallizes in C-type rare earth structure in space group Ia-3. The unit cell of C-type and 1/8 unit cell of $Nd_2Ce_2O_7$ are shown in Figure 3.6b and c. The crystal information of C-type $Nd_2Ce_2O_7$ is summarized in Table 3.6.

Table 3.5 Crystal information of F-type NCO from Brauer et al. [32].

Index	label	type	X	Y	z	Wyck.	sof
0	Nd1	Nd^{3+}	0	0	0	4a	0.5
1	Ce1	Ce^{4+}	0	0	0	4a	0.5
2	O1	O^{2-}	0.25	0.25	0.25	8c	0.875

Table 3.6 Crystal information of C-type NCO from Chakraborty et al. [35].

Index	label	type	X	Y	z	Wyck.	sof
0	Ce1	Ce^{4+}	0.25	0.25	0.25	8b	0.5
1	Nd1	Nd^{3+}	0.25	0.25	0.25	8b	0.5
2	Ce2	Ce^{4+}	-0.013	0	0.25	24d	0.5
3	Nd2	Nd^{3+}	-0.013	0	0.25	24d	0.5
4	O1	O^{2-}	0.3826	0.1367	0.3794	48e	0.918
5	O2	O^{2-}	0.3844	0.3844	0.3844	16c	0.756

Yamamura et al. [36] studied the structure of the $Ce_{1-x}Nd_xO_{2-\delta}$ (0<x<0.7) system through the Rietveld refinement of the neutron diffraction data. The samples exhibit a mixed C and F type phase and $Nd_2Ce_2O_7$ was modeled to be of 66.2% F-type phase and 33.8% C-type phase. Also, the C-type phase increase with the increasing of x.

Tyagi et al. [37] studied the phase transformation in the series of materials $Ce_{1-x}Nd_xO_{2-x/2}$ (x=0 to x=1). The crystal structure of $Ce_{1-x}Nd_xO_{2-x/2}$(x=0 to 0.5) shows the fluorite type structure while (x=0.5 to 1) exhibit C-type or A-type rare earth type structure. $Nd_2Ce_2O_7$ is in the boundary between the F-type phase and C-type phase. Sachdeva et al. [31] investigated the defect association in the series of materials $Ce_{1-x}Nd_xO_{2-x/2}$ (x=0 to 0.675) by using positron annihilation spectroscopic. The acceptor dopant Nd'_{Ce} and oxygen vacancy $V_O^{2\bullet}$ were found to associate each other, forming clusters as $[Nd'_{Ce}V_O^{2\bullet}Nd'_{Ce}]^x$. The concentration of this complex cluster increase from x=0 to x=0.5 and decreases from x=0.5 to x=0.675, due to the ordering of the oxygen vacancies for x>0.5. Results from the two studies on $Ce_{1-x}Nd_xO_{2-x/2}$ are in agreement each other.

As can be seen in Figure 3.7, Pieczulewsk et al. [38] constructed a rough phase diagram for the system N_2O_3-CeO_2 combining some existing data from other studies. The limitation of solubility of Nd_2O_3 in CeO_2 in 1000°C was found around 40%. It is worth noting that Nd_2O_3 and CeO_2 will form a complete solid solution ($Nd_2Ce_2O_7$) over 1400°C. This phase diagram may not be necessarily correct because some studies [34, 37] reported that a single phase $Nd_2Ce_2O_7$ could be synthesized below 1000°C. Also, $Nd_2Ce_2O_7$ were synthesized below 1400°C in this work. Results of crystal structure characterization will be shown in Chapter 5.

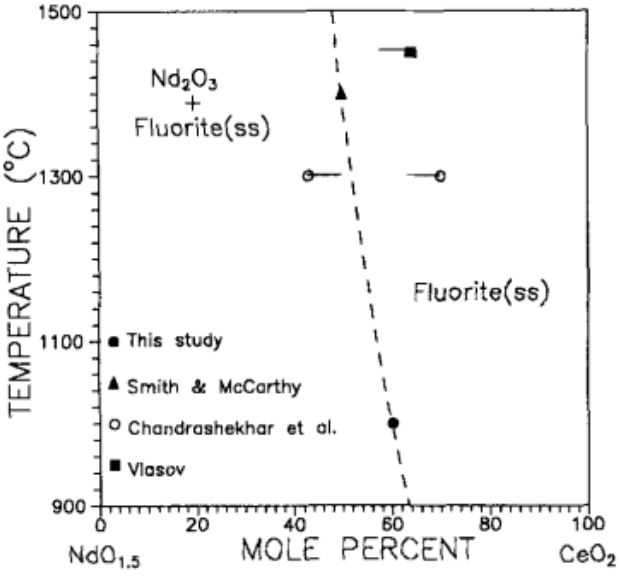

Figure 3.7 The $NdO_{1.5}$-CeO_2 phase diagram in air [38].

3.1.6. Crystal structure of $Gd_2Ce_2O_7$

$Gd_2Ce_2O_7$ was reported as a C-type related structure with space group $I2_13$ based on Ye's structure model on Gd-doped ceria [39], as shown in Figure 3.8a. In order to simplify the complicated structure, 1/8 of the unit cell is described in Figure 3.8b. The crystal information of C-type phase is summarized in Table 3.7.

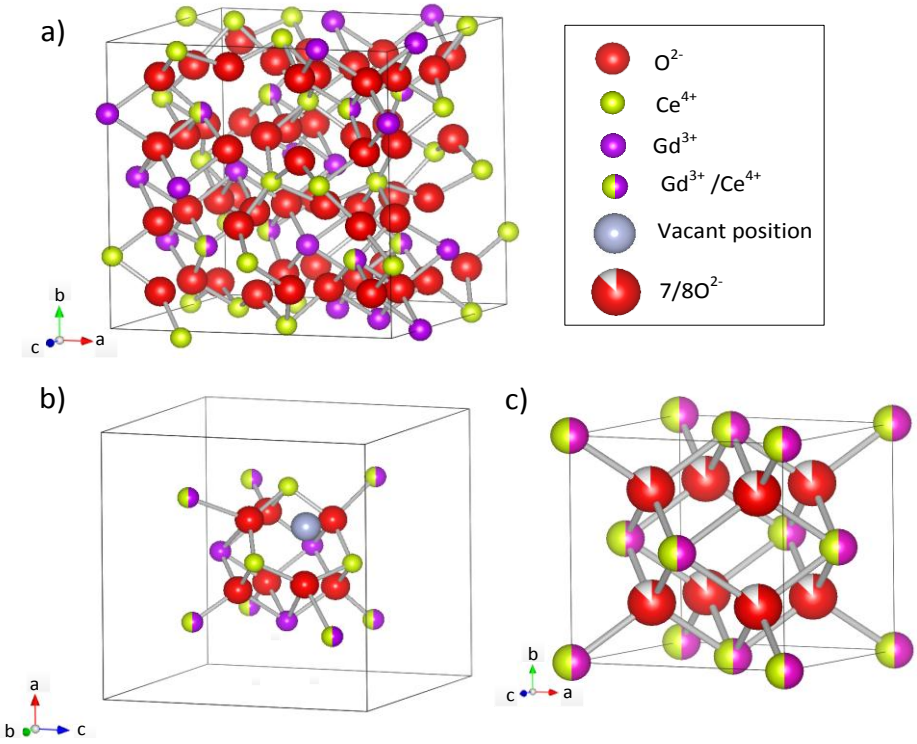

Figure 3.8 a) Unit cell of C-type rare-earth oxide GCO b) 1/8 of the unit cell of C-type GCO c) 1/8 of the unit cell of F-type phase GCO.

Table 3.7 Crystal information of C-type GCO [39].

Index	label	type	X	y	z	Wyckoff	sof
0	Gd1	Gd3+	0.265	0.265	0.265	8a	0.5
1	Ce1	Ce4+	0.265	0.265	0.265	8a	0.5
2	Gd2	Gd3+	0.5	0	0.25	12b	1
3	Ce2	Ce4+	0.977	0	0.25	12b	1
4	O1	O2-	0.363	0.13	0.378	24c	1
5	O2	O2-	0.59	0.859	0.624	24c	1
6	O3	O2-	0.375	0.375	0.375	8a	1

Many studies have been done on the crystal structure of $Gd_2Ce_2O_7$. According to Li's [40] studies on 50% doped Gd doped in ceria ($Gd_2Ce_2O_7$), large areas with microstructure different from fluorite structure were found in the sample which was indexed to be the C-type, verified by the simulated electron diffraction patterns. Similarly, Patwe et al. [41] analyzed the XRD results of a range of materials $Gd_2Ce_xZr_{2-x}O_7$ and he confirmed that $Gd_2Ce_2O_7$ is involve in C-

type lattice with lattice parameter of 10.857 Å because of the presence of the C-type superstructure peaks at 2θ=20.05°,35.07°,37.75°,42.43°,51.9°,54.8°,57.6°and 62.93°. Wang's computer calculation [42] also shows that C-type tends to be much more stable than the pyrochlore in Gd-doped Ceria. Grover et al. [43] reported that $Ce_{1-x}Gd_xO_{2-x/2}$ (x=0.1-0.4) have fluorite-type cubic lattice whereas products from x=0.5-0.95 retain the C-type cubic lattice. $Gd_2Ce_2O_7$ is located in the boundary between C-type and F-type, as shown in Table 3.8. From Scavinni's recent studies on $Ce_{1-x}Gd_xO_{2-x/2}$ by using first pair distribution function (PDF) [44], $Ce_{1-x}Gd_xO_{2-x/2}$ samples with Gd concentration $x_{Gd} \leq 0.25$ exhibited fluorite structure (space group Fm-3m) and C-type structure (Ia-3) for concentration $x_{Gd} \geq 0.5$, in accord with the phase analyses done by Grover et al. [43].

Table 3.8 Nominal composition, corresponding phase in $Ce_{1-x}Gd_xO_{2-x/2}$(x=0 to 0.95) [43].

S. no.	Nominal composition	Phase analyses	A (Å)
1	CeO_2	F	5.411(1)
2	$Ce_{0.90}Gd_{0.10}O_{1.95}$	F	5.410(1)
3	$Ce_{0.85}Gd_{0.15}O_{1.925}$	F	5.425(1)
4	$Ce_{0.80}Gd_{0.20}O_{1.90}$	F	5.432(1)
5	$Ce_{0.70}Gd_{0.30}O_{1.85}$	F	5.437(2)
6	$Ce_{0.60}Gd_{0.40}O_{1.80}$	F	5.439(2)
7	$Ce_{0.50}Gd_{0.50}O_{1.75}$	C	10.862(2)
8	$Ce_{0.40}Gd_{0.60}O_{1.70}$	C	10.854(3)
9	$Ce_{0.30}Gd_{0.70}O_{1.65}$	C	10.855(1)
10	$Ce_{0.20}Gd_{0.80}O_{1.60}$	C	10.849(1)
11	$Ce_{0.15}Gd_{0.85}O_{1.575}$	C	10.838(1)
12	$Ce_{0.10}Gd_{0.90}O_{1.55}$	C	10.837(1)
13	$Ce_{0.05}Gd_{0.95}O_{1.525}$	C	10.831(1)
14	Gd_2O_3	C	10.813(1)

F: F-type cubic; C: C-type cubic.

On the other hand, Chavan et al. [10] also reported $Gd_2Ce_2O_7$ exhibited F-type structure at 1200°C. It is observed that C-type ordering diminished with the decreasing temperature from the high temperature XRD and the C-type phase was completely transformed to F-type at 1200°C in $Gd_2Ce_2O_7$, which is also found in CeO_2 doped with 50mol% Eu, Dy and Sm. Bevan et al. [45] also reported it is a F-type cubic solid solution at 1400°C as well. The unit cell of the F-type phase of $Gd_2Ce_2O_7$ is shown in Figure 3.8c and the crystal information is summerized in Table 3.9. These studies about the crystal structure suggests that $Gd_2Ce_2O_7$ exhibit C-type to F-type phase transition from low to high temperatures, which is similar as some pyrochlore as introduced in section 3.1.2.

Table 3.9 Crystal information of F-type GCO [10].

Index	label	type	X	y	z	Wyckoff	sof
0	Gd1	Gd^{3+}	0	0	0	4a	0.5
1	Ce1	Ce^{4+}	0	0	0	4a	0.5
2	O1	O2-	0.25	0.25	0.25	8c	0.875

3.2. Electrical properties

3.2.1. Oxygen ion conduction in pyrochlore

Some pyrochlore oxides, such as $Gd_2Zr_2O_7$, $Gd_2Ti_2O_7$ and $Nd_2Zr_2O_7$, exhibit fairly high oxygen ion conductivity [46, 47]. Atomistic computer simulation study by Minervini et al. [48] shows that the oxygen ion conductivity depends on the intrinsic Frenkel disorder, which consists of a vacancy on 48f site and an interstitial on an 8a site:

$$O_O^x = V_{O(48f)}^{\bullet\bullet} + O_{i(8a)}'' \qquad \textbf{Equation 3-1}$$

Furthermore, the cation disorder increases the similarity between the three nonequivalent oxygen sites in pyrochlore. Wilde and Catlow [49] proposed that cation disorder decreases the anion Frenkel energy because cation disorder leads to a similar environment between 48f and 8b sites. Such process can be described by the defect reaction

$$A_A^X + B_B^X + O_O^X = A_B' + B_A^{\bullet} + V_{O(48f)}^{\bullet\bullet} + O_{i(8a)}'' \qquad \textbf{Equation 3-2}$$

Also, Minervini's calculation supports the idea that a cation antitsite pair adjacent to an anion Frenkel pair greatly reduces the anion Frenkel energy [48]. The calculation indicates that anions are prone to disorder if the cations are disordered in pyrochlore.

Dijk et al. [50] found it was energetically favorable for the oxygen to jump through the tetrahedral faces (path 2 in Figure 3.9a in pyrochlore. Also, Pirzada and Minervine [48, 51] confirmed that oxygen ions migrated via a vacancy mechanism at 48f site as well. As can be seen in Figure 3.9b, migration of α 48f oxygen ion to β will force the surrounding 48f oxygen ion to move into the vacant 8b site.

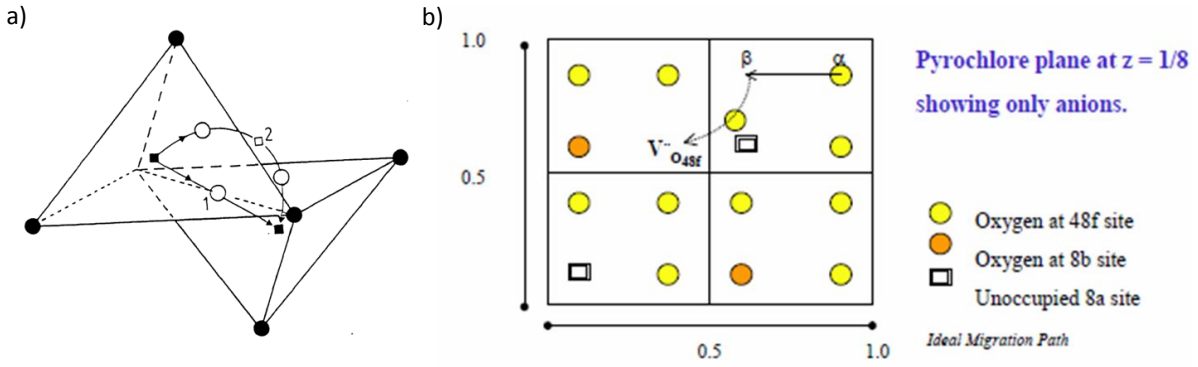

Figure 3.9 a) Dijk's model of oxygen migration [50] b) oxygen ion migration path in vacancy migration mechanism at 48f site [51].

The order and disorder structures in pyrochlore play an important role in the oxygen ion conductivity. Wuensch et al. [18] confirmed that the partial occupancy of all anion sites in the

disordered states results in high mobility for oxygen ions. Also, Wilde's [52] molecular dynamics(MD) calculation shows that the pyrochlore with ordered cation does not show fast-ion conduction. However, Pirzada et al. [51] calculated the oxygen migration activation energy in pyrochlore oxides in terms of vacancy migration mechanism at 48f site. The calculated oxygen migration energy, described by a contour map (cf. Figure 3.10), reveals that oxygen migration activation energy of lanthanide zirconate ($Ln_2Zr_2O_7$) is much lower than that of other pyrochlores. Based on the contour map, Pirzada proposed that the compound with higher degree of disorder tends to show higher activation energies. In addition, this order and disorder phenomenon will be used to interpret the measured oxide ion conductivity in this work, as shown in Chapter 6.

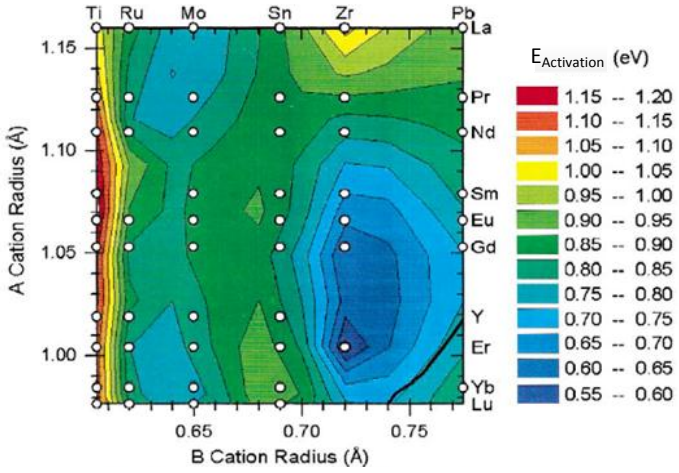

Figure 3.10 Contour map of oxygen migration activation energy (eV) [51].

Yamamura et al. [53] also studied the relationship between order-disorder transition and the oxygen ion conductivity in $Ln_2Zr_2O_7$ (Ln=lanthanide). Crystal structure of these materials changes from fluorite to pyrochlore when the ratio between two cations is above 1.26 and the maximum electrical conductivity appeared at the boundary of the transition between the two phases. The results show that the anion disorder will enhance the oxygen ion conductivity. Although these studies show that the cation disorder will promote anion disorder, Norby [54] proposed that pyrochlore with ordered cations and disordered anions may exist under certain condition.

Tuller et al. [47, 55, 56] investigated a range of pyrochlore-type materials $Gd_2B_2O_7$ (B= Ti, Sn) and these materials exhibited enhanced total conductivity (electronic or ionic conductivity) after doping. On the other hand, for pyrochlore $Gd_2Zr_2O_7$ with disordered cations [57, 58], Moon [59] pointed out that the conductivity of 1%Ca doped $Gd_2Zr_2O_7$ did not exhibit effect of doping, i.e. enhanced conductivity. Xing et al. [60] explained such insignificant effect of doping may be due to cation antitsite disorder. The charge of these acceptor dopants are just

compensated by the charge of disordered cation antitsite. The effect of doping in the materials investigated in this work will be discussed in Chapter 6.

3.2.2. Protonic conduction in pyrochlore oxides

Some pyrochlore related oxides have been reported to exhibit proton conduction under wet conditions. $La_2Zr_{1-x}Y_xO_{7-\delta}$, as one of the most significant proton conductors in pyrochlore, was first reported by Shimura [61]. Labrincha et al. [62] interpreted the defect chemistry of undoped $La_2Zr_2O_7$ by combining the formation of anti Frenkel defects and hydration of oxygen vacancy. The effect of Y for Zr substitution can be interpreted by the following defect chemistry reaction:

$$Y_2O_3 + La_2O_3 + H_2O \xrightarrow{La_2Zr_2O_7} 2La_{La}^{X} + 2Y_{Zr}^{/} + 2H_i^{\bullet} + 7O_O^{X} \qquad \textbf{Equation 3-1}$$

In addition, Omata et al. [63, 64] found that calcium doped $La_2Zr_2O_7$ in La or Zr sites exhibited predominate proton conduction below 873K. The transport number of protons in calcium doped $La_2Zr_2O_7$ is shown in Figure 3.11.

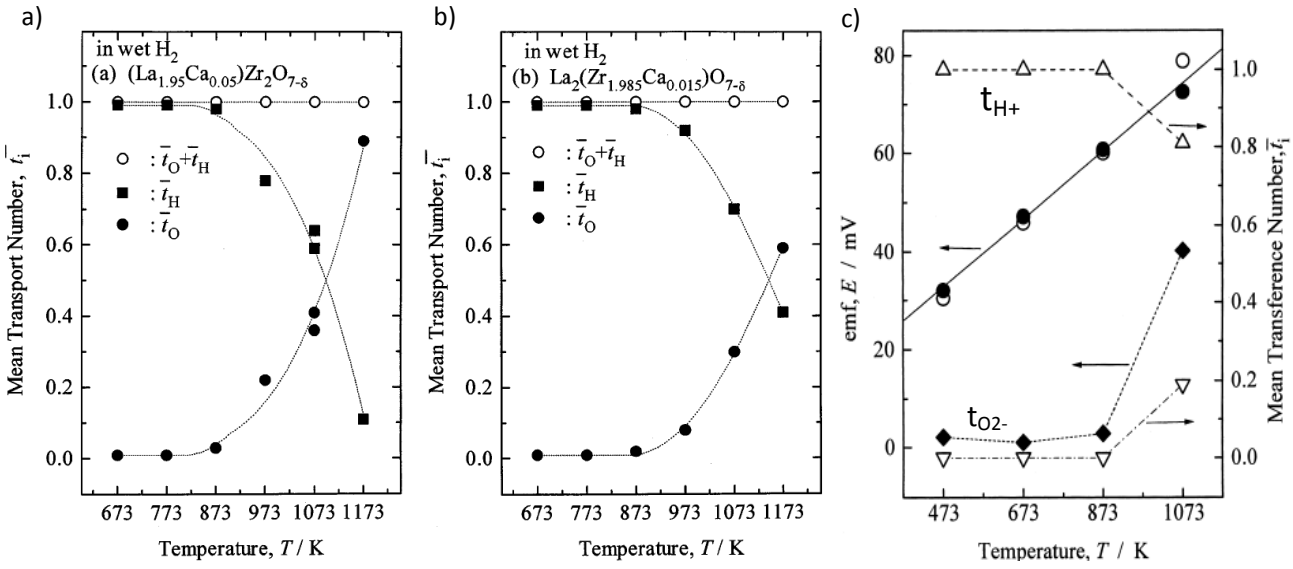

Figure 3.11 a) Mean transport number of protons, oxygen ion, and total ions for a) $La_{1.95}Ca_{0.05}Zr_2O_{7-\delta}$ [63] b) $La_2Zr_{1.985}Ca_{0.015}O_{7-\delta}$[63] c) $La_{1.98}Ca_{0.02}Zr_{1.98}Ca_{0.02}O_{7-\delta}$ [64].

In addition, proton conductivities of $La_{2-x}Ca_xZr_2O_{7-\delta}$ (x=0.05, 0.015) at 873 K were 0.068 Scm^{-1} and 0.01 Scm^{-1}, respectively, and increased with the increasing level of acceptor-doping. Furthermore, the proton conductivity of $La_{2-x}Ca_xZr_2O_{7-\delta}$ (x=0.03) is three times higher than that of $La_2Zr_{1.985}Ca_{0.015}O_{7-\delta}$. Such differences in proton conductivity may be ascribed to the different oxygen vacancies for the proton dissolution in $La_{2-x}Ca_xZr_2O_{7-\delta}$ and $La_2Zr_{2-x}Ca_xO_{7-\delta}$ systems. According to the molecular dynamics (MD) simulation about proton migration in

$La_2Zr_2O_7$ [65], as shown in Figures 3.12a and b, the stable protons positions at various oxygen sites were (ii) and (v). Thus, the most favorable pathway for proton is the continuous trajectory as (ii)-(ii)-(v)-(v)-(ii)-(ii)-…, as shown in Figure 3.12c.

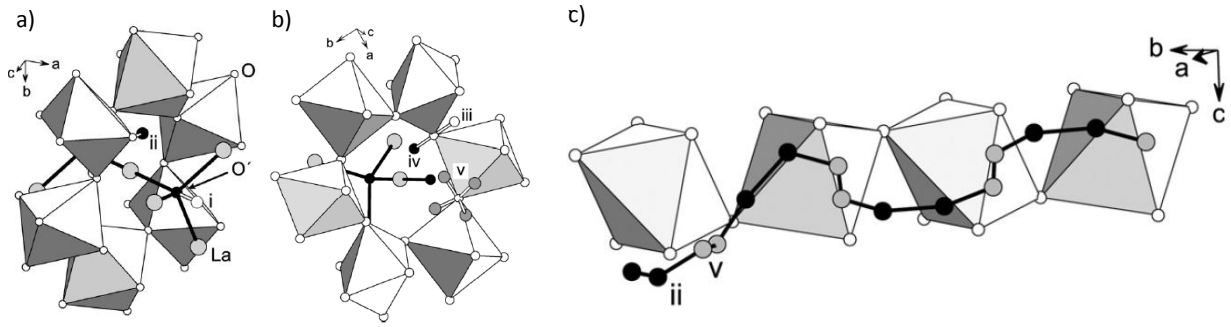

Figure 3.12 a) Stable proton positions at O' (i) and O (ii) in $La_2Zr_2O_7$ b) Stable proton positions (iii)-(iv) c) proton pathway in pure $La_2Zr_2O_7$ [65].

Furthermore, Shimura et al.[61] also found pyrochlore oxides $Ln_2Zr_{2-x}Y_xO_{2-\delta}$ (Ln=La, Nd, Gd, Sm and Er) were pure proton conductors in wet hydrogen, as shown in Figure 3.13.

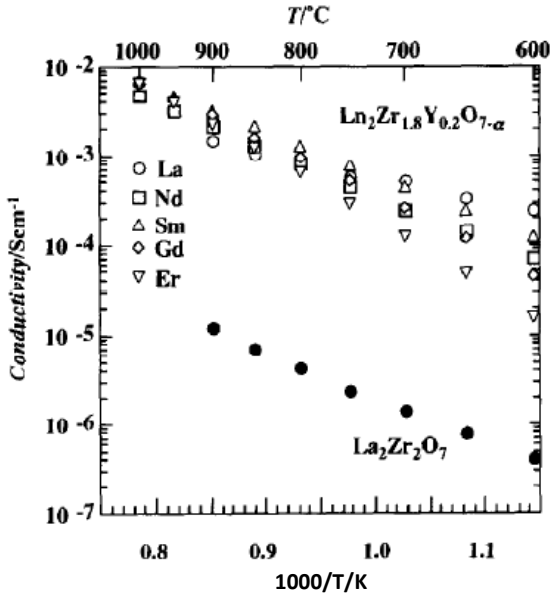

Figure 3.13 a) Electrical conductivities of $La_2Zr_2O_7$ and $Ln_2Zr_{1.8}Y_{0.2}O_{7-\delta}$ (Ln=La,Nd, Sm, Gd and Er) in wet hydrogen [61].

In lanthanide zirconate pyrochlores, non-systematic dependency of total conductivity on lanthanide cations (Ln^{3+}) is revealed. On the contrary, insignificant protonic conduction was found in pyrochlore $Y_2Ti_{1.8}M_{0.2}O_{2-\delta}$(M= In and Mg) [61].

Eurenius et al.[66] studied $Ln_{1.96}Ca_{0.04}Sn_2O_{7-\delta}$ (Ln=La, Sm and Yb) system. Proton conductivity was found to depend critically on the lanthanide size. The highest proton conductivity is

compound with La^{3+}, $\sigma_{H+} = 4 \times 10^{-7} Scm^{-1}$ at 300°C. Also, the tendency for proton absorption was also strongly influenced by lanthanide, being greatest for $La_{1.96}Ca_{0.04}Sn_2O_{7-\delta}$. In addition, Eurenius et al.[67] also reported that both $Sm_{1.92}Ca_{0.08}Ti_2O_{7-\delta}$ and $Sm_2Ti_{1.92}Y_{0.08}O_{7-\delta}$ pyrochlores present proton conduction under wet O_2. Similarly, the proton conduction of $Sm_{1.92}Ca_{0.08}Sn_2O_{7-\delta}$ and $Sm_2Sn_{1.92}Y_{0.08}O_{7-\delta}$ also shows the similar effect of doping as $Sm_2Ti_2O_7$ [67] that calcium doped in lanthanide exhibits higher proton conductivity. Infrared spectroscopy(IR) results suggest the presence of protonic defects at both the O(2) and O(1) sites for the Ln- site doped samples while only at O(1) for the B site doped samples meaning that Ln-site doped sample is more favorable to be hydrated. Furthermore, proton conduction of $Sm_2B_2O_7$(B=Ti,Sn,Zr,and Ce) was found to depend on ionic radius of B site [68]. As can be seen in Figure 3.14a, the proton concentration of $Sm_2B_2O_7$ with Ti and Sn in B site is much higher than B with Ce and Zr. Furthermore, the diffusion coefficient is inversely proportional to the ionic radius of the B site in acceptor doped pyrochlore oxides $Sm_2B_2O_7$, as shown in Figure 3.14b. In summary, the Ln^{3+} site and B^{4+} site of $Ln_2B_2O_7$ both determine the proton conduction. Combining the above studies, the effect of Ln^{3+} in $Ln_2Ce_2O_7$ on proton conduction will be further discussed in Chapter 6.

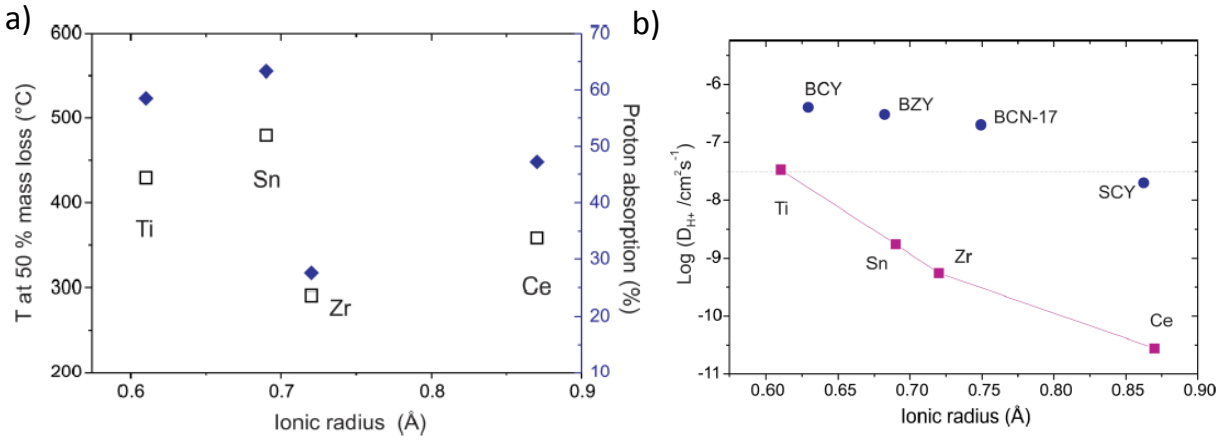

Figure 3.14 a) Summary of dehydrate temperature and level of absorbed protons [68] b) proton diffusion of $Sm_{1.94}B_{0.06}Ce_2O_{7-\delta}$ (B=Ti,Sn,Zr,Ce)at 300°C as a function of B site radius.

Fjeld et al.[69] reported that Ca-doped $Er_2Ti_2O_7$ with a pyrochlore structure exhibited protonic conduction. Based on measured impedance spectra, grain boundary was found to play a vital role in the proton transport and oxygen vacancy was considered as a main charge carrier in the grain interior. In addition, Haugsrud and Norby [70] studied the a mixed ionic and electronic conductor $La_{1.98}Ca_{0.02}Ti_2O_{7-\delta}$ with a distort orthorhombic from the cubic pyrochlore structure. The proton conductivity was characterized by EMF measurement to be 6×10^{-5} Scm^{-1} at 750°C in wet hydrogen.

3.2.3. Protonic conduction in F-type and C-type oxides

As we know from Section 3.1.3, the crystal structures of F-type and C-type oxides are similar as pyrochlore and some of them show proton conduction. Furthermore, some of the compounds with $A_2B_2O_7$ exhibit F-type or C-type structure, e.g., $Ln_2Ce_2O_7$ (Ln=Lanthanide).

Besikiotis et al. [71] found that disordered fluorite related material (F-type) $La_2Ce_2O_{7-\delta}$ exhibits oxygen ion conduction at high temepratures while proton conduction starts to dominate below 500°C ($\sigma_{H+} \approx 1.2 \times 10^{-5} Scm^{-1}$ at 400°C), as shown in Figure 3.15a. Moreover, total conductivity of calcium doped sample decreases compared with undoped sample, as shown in Figure 3.15b. Similarly, effect of doping on electrical conduction of $Nd_2Ce_2O_7$ and $Gd_2Ce_2O_7$ will be studied in this work.

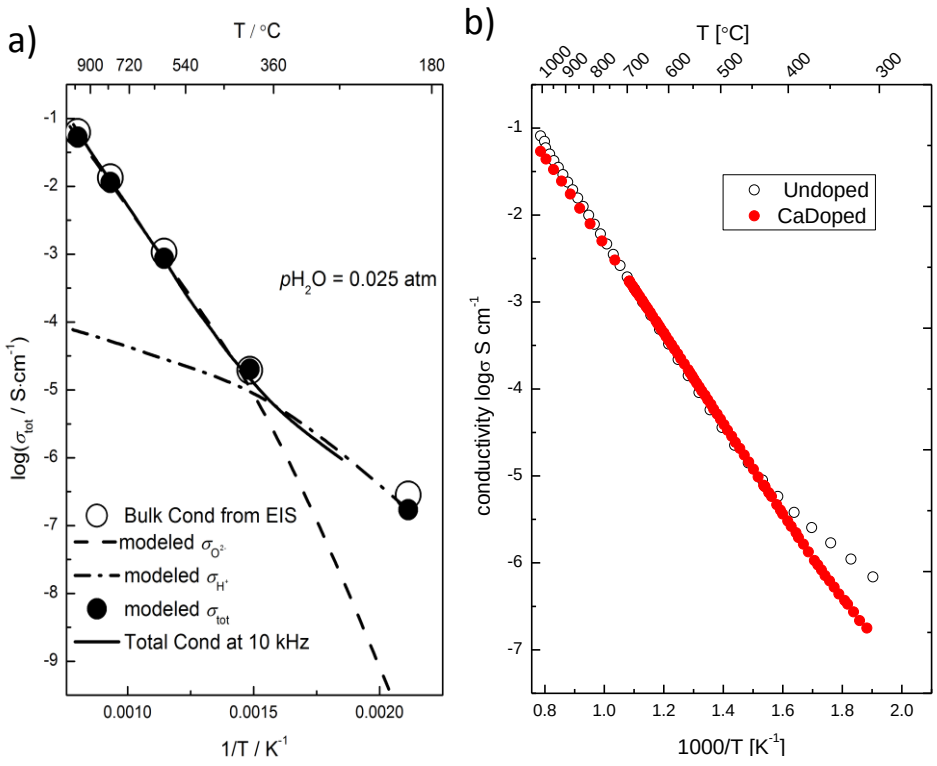

Figure 3.15 a) Modeled conductivity of $La_2Ce_2O_7$ between 1000 and 200 °C [71] b) Total conductivity vs. 1000/T in $La_2Ce_2O_7$ and Ca doped $La_2Ce_2O_7$ [72].

The structure of rare-earth tungstates can be described as either an ordered defective fluorite or a disordered pyrochlore [73-75] and this group of materials exhibit proton conduction [76]. From Figure 3.16, the proton conductivity decreases with decreasing radius of Ln^{3+} which show the similar trend in another group of materials $LnNbO_4$ (Ln=lanthanide) [77]. Furthermore, calcium doped $LnW_{1/6}O_2$ showed lower proton conductivity than undoped sample. The decreasing conductivity is explained by the association between acceptor and protons.

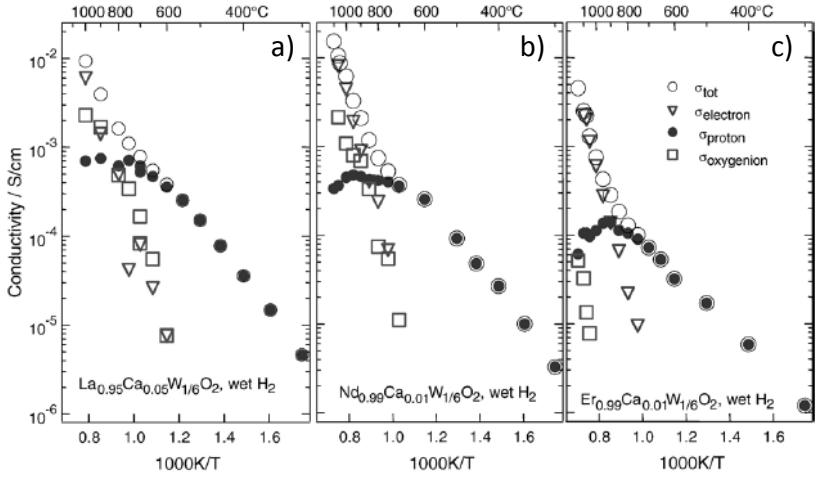

Figure 3.16 Partial conductivities, as determined from the EMF-technique, as a function of the 1/T for Ca doped $LaW_{1/6}O_2$ (a), $NdW_{1/6}O_2$ (b) and $ErW_{1/6}O_2$ (c) under H_2+2.5% atmospheres in the temperature range 300°C to 1050°C [76].

In addition, Zhu and his co-workers [78] used the electromotive forces (EMF) to measure the ionic transport properties in F-type 10GDC (10% Gd doped CeO_2). 10GDC with F-type related structure exhibits proton conductivity around 10^{-3} Scm^{-1} in H_2 and $5.9\times10^{-3}Scm^{-1}$ in oxygen at 400°C.

Norby et al.[79] studied the proton and oxygen ion conductions in acceptor-doped C-type rare-earth sesquioxides Y_2O_3+1mol% MgO, Sm_2O_3+1mol%CaO, Gd_2O_3+1mol%CaO, and YYb+5mol%CaO. According to Figure 3.17, the proton conductivity is higher in the sesquioxides with larger cations than those with lower cations. This trend is explained by the much easier oxygen vibrations in the bonds to the more polarizable heavy cation and migration of proton will be more favorable in this case.

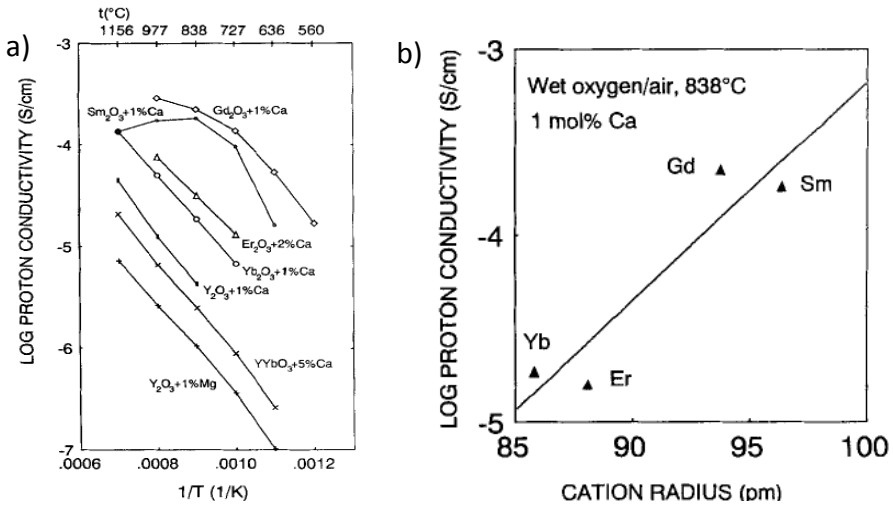

Figure 3.17 a) Proton conductivity vs. 1/T for acceptor-doped cubic rare-earth oxides of (Y_2O_3+1%Ca, Er_2O_3+2%Ca, Yb_2O_3+1% Ca) b) proton conductivities of 1 mol% calcium doped samples at 838°C, as a function of rare-earth cation radius [79].

Based on such previous studies, the proton conduction in F-type, C-type, P- type materials depends on the radius of the rare earth. Also, such dependency of materials in this work will be discussed in Chapter 6.

3.2.4. Electrical properties of $Nd_2Ce_2O_7$ and $Gd_2Ce_2O_7$

Liu et al. [34] investigated electrical properties of $Nd_2Ce_2O_7$ co-doped with Gd_2O_3 and ZrO_2 and the temperature dependency is shown in Figure3.18a. Their results presented that the lattice parameter will decrease with increasing x in $(Nd_{1-x}Gd_x)_2(Ce_{1-x}Zr_x)_2O_7$ and the conductivity will also change with lattice parameter changing. Also, the resistance contributing from the grain boundary is so small based on the result from the impedance spectra.

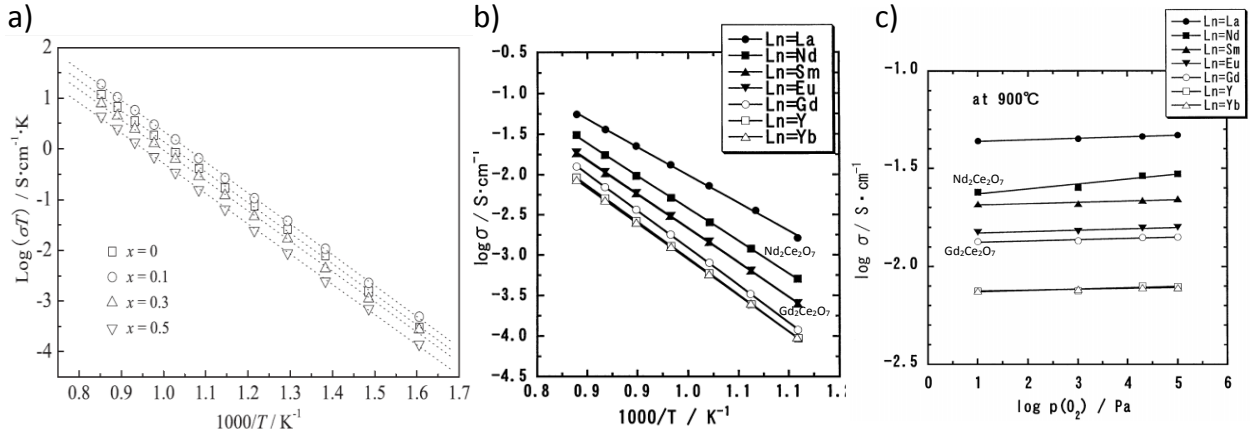

Figure 3.18 a) Arrhenius plot of the electrical conductivity of $(Nd_{1-x}Gd_x)(Ce_{1-x}Zr_x)_2O_2$ [34] b) Arrhenius plots of conductivity $Ln_2Ce_2O_7$ [36] c) log pO_2 vs. logσ of $Ln_2Ce_2O_7$ [36].

The pre-exponential constant and activation energy of $Nd_2Ce_2O_7$ is summarized in Table 3.10. In addition, as shown in Figure 3.18 b and c, Hagiwara and his co-workers [36] studied the electrical properties in the group of $Ln_2Ce_2O_7$ (Ln=La, Nd, Sm, Eu, Gd, Y and Yb). In this group, only $Nd_2Ce_2O_7$ was found as an ionic and electron hole mixed conductor at oxidizing atmospheres. Xia et al. [80] studied a group of materials $Gd_2(Zr_{1-x}Ce_x)_2O_7$ (0.1<x<0.3), from which the total conductivity was found decreases with the increasing cerium content.

Table 3.10 Electrical conductivity σ at 800°C, Unit cell volume V, Activation energy Ea and pre-exponential constant σ_0 for $Nd_2Ce_2O_7$ and $Gd_2Ce_2O_7$.

Compounds	σ at 800°C(Scm^{-1})	V(nm^3)	Ea ($kJmol^{-1}$)	σ_0($Scm^{-1}K$)	Reference
$Nd_2Ce_2O_7$	9.62	0.0654	116	9×10^7	[28, 34]
$Gd_2Ce_2O_7$	3.66	0.0611	132	N/A	[28]

Grimes et al. [48] pointed out that the oxygen ion conduction is determined by the anion Frenkel reaction. Moreover, cation antitsite is believed to improve the anion antitsite Frenkel reaction. As shown in Figure 3.19, potential energies of cation disorder and anion disorder in $A_2B_2O_7$ pyrochlore related materials are summarized. The potential energy of anion antitsite Frenkel reaction of $Nd_2Ce_2O_7$ and $Gd_2Ce_2O_7$ is low, indicating that cations and anions in these two materials are disordered. The high degree of anion disorder can be a reason for the high conductivity of $Nd_2Ce_2O_7$ and $Gd_2Ce_2O_7$.

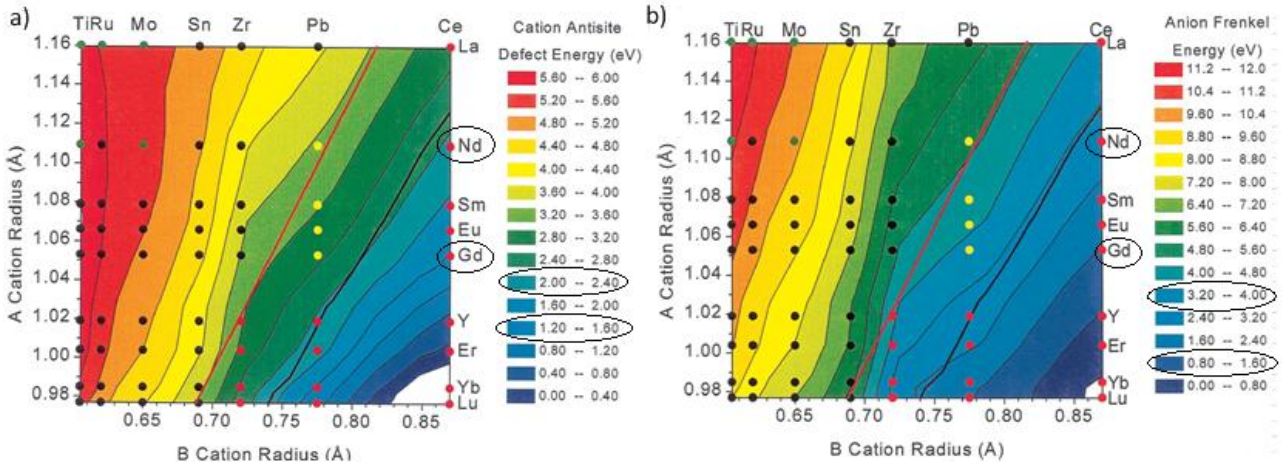

Figure 3.19 a) Contour map of cation antitsite defect-formation energy b) contour map of anion Frenkel pair defect-formation energy [48].

3.3. Protons in fluorite related materials at low temperatures

Some studies in this work are related to the protonic conduction of pyrochlores at low temperatures and the following review focuses on such electrical properties.

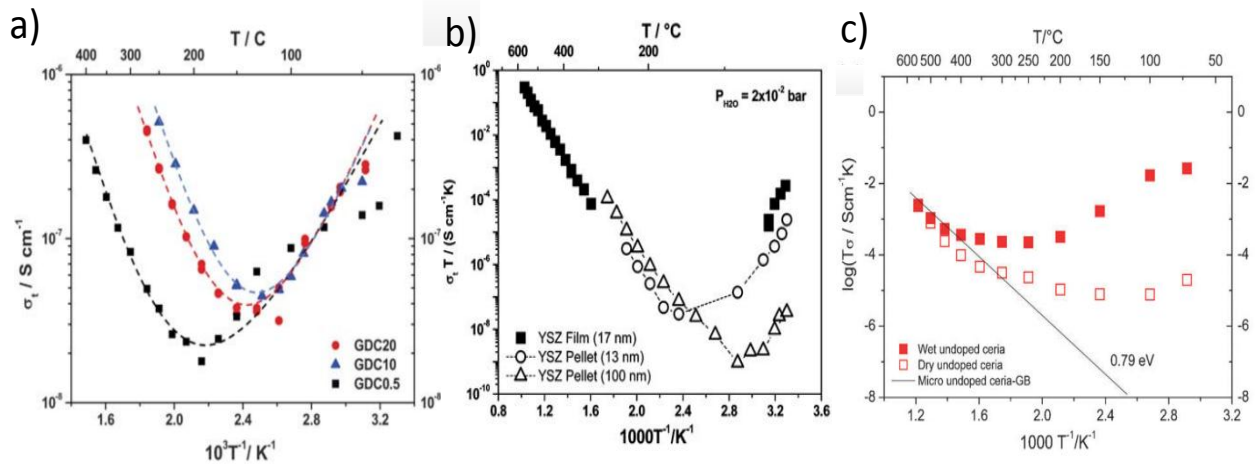

Figure 3.20 a) The total conductivity with 0.5%,10% and 20% doped ceria [81] b) total conductivity as a function of size in YSZ8 [81] c) Arrhenius plots of the conductivity of nanocrystalline un-doped ceria [82].

Recently, protonic conduction in fluorite related materials at low temperatures have been discovered by Kim et al. and Maier et al. [81-83]. As shown in Figure 3.20, nanocrystalline ceria, below 100°C, YSZ and Gd-doped ceria exhibited enhanced total conductivity with decreasing temperature. Furthermore, Avila-Paredes et al. [84] mentioned that the total conductivity of nanocrystalline materials will be enhanced with the decreasing grain size.

Kim et al. [82, 85] thought that proton plays a vital role in this phenomenon and he envisaged that the pathway for the protons diffusion at low temperatures may be along the grain boundaries. Generally, the grain boundary short circuits the bulk due to its relatively high conductance, as shown in Figure 3.21.

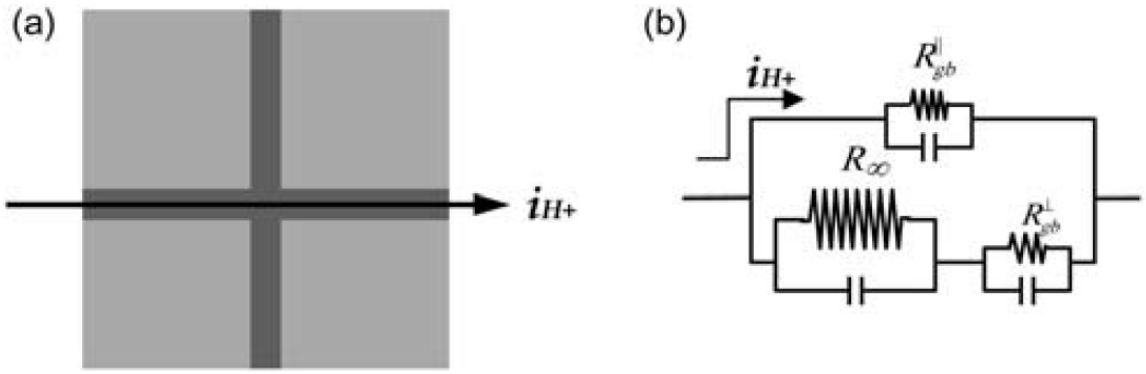

Figure 3.21 a) Kim's brick layer model for the proton diffusion pathway along the grain boundary b) the equivalent circuit for the model [84].

However, Maier and his coworkers discovered that nanocrystalline CeO_2 absorbed 0.03mole of water per mole of CeO_2 which means the 1nm grain boundary core is capable to accommodate about 10^{22} proton/cm^3 which is relatively larger than the value of 10^{21} proton/cm^3 in the bulk of some proton conductors [82]. However, the reason for protons moving along the grain boundary core is still unclear. In addition, they also pointed out the condensation or absorption of water in pores might be another possible reason. They found the dielectric constant calculated based on single semicircle impendence spectrum under wet and dry conditions are different which indicates the proton diffusion mechanism is different from Kim's model. Yamaguchi et al. [86] believed that the low temperature conductivity might a result of the surface charge. The acid/base reactivity of Lewis acid site and Brønsted acid sites on the surface of oxides will impact the electrical properties of oxides under wet conditions. However, Pietrowski et al. [87] proposed that this low temperature phenomenon in YSZ cannot be due to a bulk phenomenon or the grain boundary effect, but because of the internal surfaces provided by pores and micro cracks.

4. Experimental methods

In this part, the experimental methods carried out in this work were described. Firstly, samples were synthesized and then the crystal structure of the specimens was characterized by powder X-ray diffraction (PXRD). Also, the morphology and the elemental composition of the samples were investigated by Scanning Electron Microscopy (SEM). The electricity measurements were carried out by a system including an electrical measurement cell and impedance analyzers. The electrical characterization was done by using a two-probe four-wire measurement. The electrical properties were studied by impedance spectroscopy as a function of temperature, water vapor partial pressure and oxygen partial pressure in the temperature range 1100°C to 300°C. In addition, the electrical conductivity of selected materials was also measured at even lower temperature. Furthermore, thermogravimetry (TG) was utilized to measure the mass variation under wet and dry conditions from 1100°C to 300°C. Also, isothermal isotope swapping measurement and isothermal pO_2 measurement were carried out at 400°C and 550°C, respectively. Finally, mass change was also measured from 100°C to 20°C in wet air.

4.1. Synthesis and fabrication of samples

Several different methods was used to synthesize samples in this work including solid state reaction (SSR), co-precipitation reaction (CPR) and combustion reaction (CR). The samples and the methods of synthesis are summarized in Table 4.1 as follow:

Table 4.1 List of the samples synthesized in this work.

Sample composition	Abbreviated name	Methods
$Nd_2Ce_2O_7$	NCO	CPR
$Nd_{1.95}Ca_{0.05}Ce_2O_{7-\delta}$	NCCO5	CPR & CR
$Nd_{1.9}Ca_{0.1}Ce_2O_{7-\delta}$	NCCO10	CPR
$Nd_{1.8}Ca_{0.2}Ce_2O_{7-\delta}$	NCCO20	CPR
$Nd_2Ce_{1.9}Y_{0.1}O_{7-\delta}$	NCYO10	CPR
$Nd_2Ce_{1.9}Nb_{0.1}O_{7+\delta}$	NCNbO10	SSR
$Gd_2Ce_2O_7$	GCO	CPR
$Gd_{1.95}Ca_{0.05}Ce_2O_{7-\delta}$	GCCO5	CPR & CR
$Gd_{1.9}Ca_{0.1}Ce_2O_{7-\delta}$	GCCO10	CPR
$Gd_{1.8}Ca_{0.2}Ce_2O_{7-\delta}$	GCCO20	CPR

4.1.1. Solid State reaction method (SSR)

Solid state reaction is well known as an easy and convenient method to synthesize many inorganic materials. Stoichiometric amounts of the reactants are mixed, crushed and calcined several times which will help to gain a homogenous dispersion of the particles in the pressured powers, which is also called green body. SSR is always under much higher

temperature than CPR and CR because the counter diffusion of the ions needs fairly high energy to occur due to the larger distance between cations.
The reagents used in synthesizing GCO5, GCO10, GCO20 and NCNbO10 were $CaCO_3$ (Sigma-Aldrich, chemometric standard, 99.999%), Gd_2O_3 (Union MOLYCORP, 99.9%), Nd_2O_3 (Union MOLYCORP, 99.9%), $Ce(NO_3)\cdot 6H_2O$ (Fluka chemika,>99.0%). Especially, $CaCO_3$ and $Ce(NO_3)\cdot 6H_2O$ were chosen as the precursor of CaO and CeO_2 in the reaction.
Before mixing the reactants, Nd_2O_3 and Gd_2O_3 were dehydrated at 900°C overnight in ENTECH ENERGITEKNIK AB while $CaCO_3$ was heated to 500°C due to its low decomposition temperature. Afterwards, stoichiometric amount of the reactants were weighed and mixed in an agate mortar. During the crushing in the mortar, the sizes of the particles gradually decreased and the reactants were homogeneously mixed resulting in reduced diffusion length. After that, mixed powders were cold pressed into several dense pellets of 2.5cm diameters to get intimately contact between the reactants. The pellets were calcined at 900°C for 10 hours followed by calcination at 1000°C for another 10 hours twice. Crushing and pressuring were carried out after each calcination and obtained powders after each calcination were characterized by PXRD.

4.1.2. Co-precipitation reaction method (CPR)

CPR is a type of a wet chemical method which is widely used in preparing ceramics. In the coprecipitation method, oxides or salts of the different cations are dissolved in the same medium (e.g. dilute acids) and the cations are precipitated together with addition of the precipitating ions such as oxalate, carbonate or hydroxide. The precipitates prepared by this method are calcined at a lower temperature compared to solid state reaction because the diffusion length of the cations is greatly reduced when the cations are brought in intimately contact. Also, the nano-sized particles obtained after the calcination can be sintered at lower temperatures due to relatively high contract area between the particles. However, the precursor will inevitably incorporate some extra elements that contaminate the reactants in wet chemical methods. On the other hand, materials containing insolvable elements like Nb, Ta, and W which are difficult to solve cannot be easily prepared by the co-precipitation method or even wet chemical methods.

For preparing samples NCO, NCCO5, NCCO05, and NCCO10 and NCOY10 the starting materials used were $CaCO_3$ (Sigma-Aldrich, chemometric standard, 99.999%), Nd_2O_3 (Union MOLYCORP, 99.9%), $Ce(NO_3)\cdot 6H_2O$(Fluka chemika,>99.0%), ammonia(28%, VWR international S.A.S), nitric acid (68%, VWR international S.A.S).

Above all, the main reactants used in this work were measured by thermogravimetry. As shown in Figure 4.1, the mass of Cerium (III) nitrate hexahydrate (M_w=434.22g/mol) declined

gradually from room temperature to 600°C and became constant above 600°C. The final product was characterized to be CeO_2 whose theoretical molecular weight is 39.6 % (39.5% from Figure 4.1) of $Ce(NO_3)\cdot 6H_2O$.

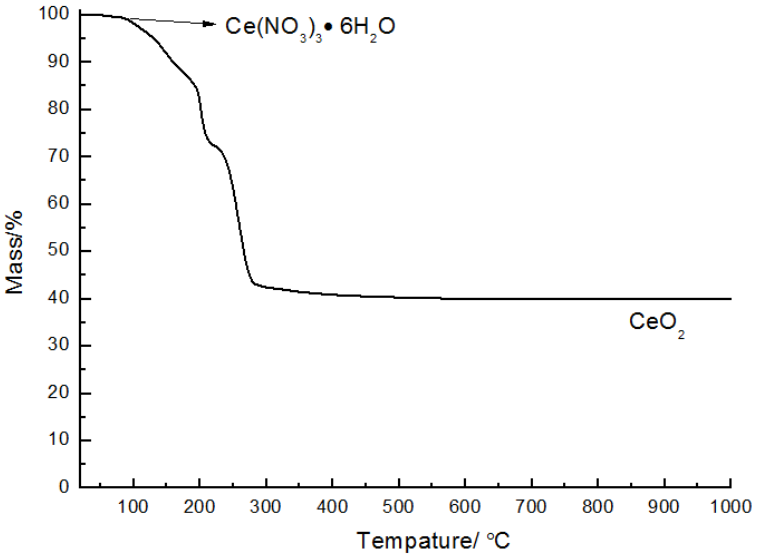

Figure 4.1 Thermogravimetry of the reactant $Ce(NO_3)_3\cdot 6H_2O$ from RT to 1000°C.

The raw materials $CaCO_3$, Nd_2O_3 and $CaCO_3$ were heated at 600°C for several hours in order to dehydrate the water absorbed by the powders. Then stoichiometric amount of the reactants were weighed by electronic balance (SARTORIUS ED224S). $CaCO_3$, Nd_2O_3 or Gd_2O_3 were dissolved in dilute nitric acid at 80°C. When the solution became clear, meaning that all the cations were dissolved entirely into the nitric acid, $Ce(NO_3)_3$ was poured directly into the solution containing the other cations followed by continuously mixed by a magnetic stirrer at 80°C. The PH of the solution was adjusted around 7 by dilute ammonia. The excessive amount of $(NH_4)_2CO_3$ was dropwise added into the solution and white particles formed. The turbid liquid was located in the fume hood overnight. The precipitate and the liquid were divided into two layers. A little supernatant was taken out and $(NH_4)_2CO_3$ was added in order to check if all cations were completely precipitated. The precipitates were leached out and dried at 150°C. The dried precipitates were calcined in furnace (Nabertherm BmbH) at 800°C for 10 hours. The chemical reactions are given as

$$Nd(NO_3)_3(aq) + Ce(NO_3)_3(aq) + 3(NH_4)_2CO_3(aq) = \frac{1}{2}Nd_2(CO_3)_3(s) + \frac{1}{2}Ce_2(CO_3)_3(s) + 12NH_4NO_3(aq)$$

$$Nd_2(CO_3)_3(s) + Ce_2(CO_3)_3(s) + \frac{1}{2}O_2(g) \xrightarrow{\Delta} Nd_2Ce_2O_7(s) + 6CO_2(g)$$

4.1.3. Combustion Synthesis

NCCO5 was also synthesized by combustion reaction. Nano-sized powders were prepared based on nitrates of calcium, cerium and neodymium using ethylene diamine tetra-acetic acid (EDTA) as fuel. Calcium nitrate and neodymium nitrate were prepared through dissolving stoichiometry ratio of Nd_2O_3, $CaCO_3$ $Ce(NO_3)_3$ into nitric acid. The solution was kept stirring at 80°C until the mixed solution became clear. Ammonia was introduced to adjust the pH of the solution around 7. Then, an appropriate amount of EDTA (EDTA to metal ratio of 1) was dissolved in dilute ammonia solution and the pH was modified around 7 by diluted nitric acid. The solution was dropwise added to the EDTA ammonia solution. During adding the solution, the pH kept decreasing and the EDTA was precipitated. So, the diluted ammonia solution was added to keep the PH around 7. After adding up all the solutions, the mixed solutions were kept stirring at 100°C to evaporate the solvent. With the evaporation of the solvent, the solution became more vicious and formed a gel. The gel was initially combusted at 250°C. After the first combustion, black ash was formed. The black ash was calcined at 500°C for 5 hours followed by calcination at 950°C for 10 hours. After the second calcination, fine powders were prepared.

4.1.4. Sintering

The powders were grinded together several drops of binder (Paraloid B-60/B-72) in agate mortar. Pellets of 2.5cm diameter were pressed by hydraulic press (Specac GS15011) using 2.5 tons. $Nd_2Ce_2O_7$ is stable up to 1400°C and the thermal expansion coefficient constant is up to 13×10^{-6} K^{-1} in the temperature range from 100°C to 1250°C [88]. Because of the low thermal expansion coefficient, the temperature cooling rate should be low in order to prevent the cracking results from the serious thermal expansion. The temperature profile of the sintering was shown in Figure 4.2.

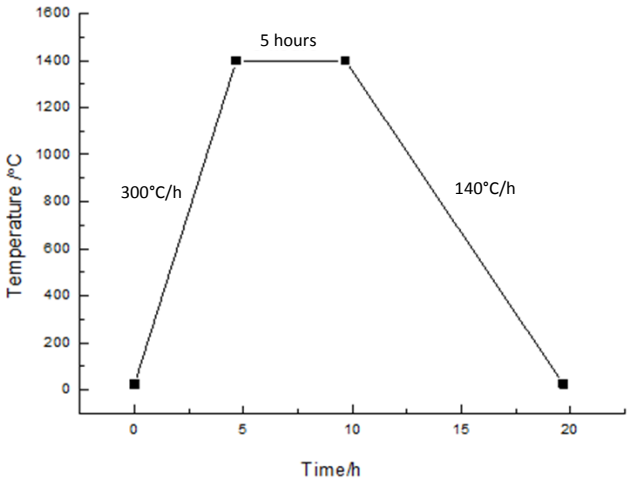

Figure 4.2 Temperature profile of sintering NCO, NCCO5, GCO and GCCO5.

4.1.5. The density measurement

The practical densities ρ_r were obtained through the measurement of the dimension by micrometer followed by checking the weight by the balance. The relative density for the sample NCO and GCO is over 70%, while the relative density for the samples doped by Ca^{2+} illustrates substantially high density which is over 90%. CaO formed by decomposition of $CaCO_3$ will not only significantly reduce the sintering temperature, but also enhance the density of the sample as well. The improved relative density can be attributed from the Ca^{2+} playing a role as the sintering aid.

Table 4.2 List of the relative density of the samples synthesized in this work.

Name	Measured density g/cm	theoretic density g/cm	relative density%
NCO	5.042	6.870 [34]	74%
NCCO5	6.548	6.870	95%
NCCO10	6.525	6.870	95%
NCCO20	6.520	6.870	95%
GCO	5.537	7.295 [89]	76%
GCCO5	6.346	7.295	87%
GCCO10	5.858	7.295	80%
GCCO20	6.508	7.295	89%

4.1.6. Electrodes

Before attaching the electrodes on the sample, two sides of the pellet were initially polished by 500 grit sandpaper followed by polished by 250 grit sandpaper to make the two sides flat and coplanar. Both of the sides of the sample were painted by platinum ink (METALOR 6695) and dried at 150°C for 30 minutes separately twice. Two round platinum electrodes were attached on both sides followed by being covered by the Pt ink again. The prepared samples were heated at 1100°C for 1 hour. GCO and GCCO5 pellets with electrodes were shown in Figure 4.3.

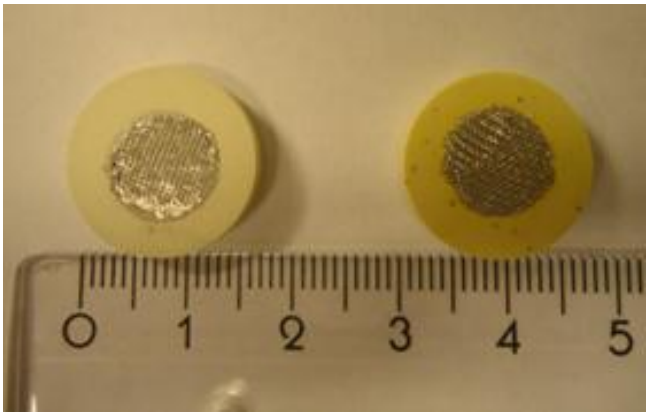

Figure 4.3 Picture of GCO (left) and GCCO5 (right) with Pt electrodes

4.1.7. Guard electrode

A guard electrode was prepared on the sample to diminish the conductivity result from the surface charge. After preparation of the electrodes, the platinum ink (METALOR 6695) was painted along the edge of the surface and the ink was dried at 150°C for 30 minutes. A platinum ring was prepared by pressing a platinum wire by Hydraulic press (Specac GS15011) under 5 tons. The Pt ring was attached on the place where painted on the platinum ink and was covered by the Pt ink again. The sample with guard electrode was heated at 1100°C for one hour in the furnace to evaporate the solvent. A GCO pellet with guard electrode is shown in Figure 4.4. After heating, the current between central electrode and guard electrode was tested by a hand held multimeter in order to make sure they were open circuit.

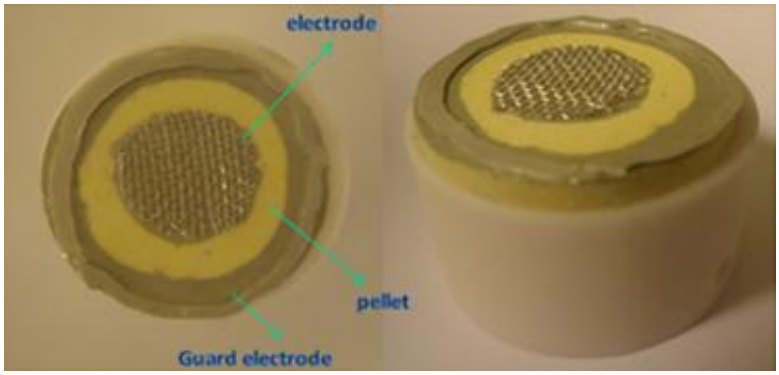

Figure 4.4 The photo of GCO with guard electrode.

4.2. Sample characterization

Powder x-ray diffraction (PXRD) and scanning electron microscopy (SEM) were used to characterize the crystal structure and phase purity. Rietveld refinement enables to obtain the specific information about the crystal structure. In this section, the sample characterization techniques used in this work are overviewed.

4.2.1. X-ray diffraction (XRD)

X-ray powder diffraction (XRD) is an analytical technique on phase identification of a crystalline material with the information of unit cell dimensions. The technique uses a known x-ray wavelength to determine unknown spaces between crystal planes.

In powder XRD pattern, crystal structure is determined by the intensity and position of the peaks. The intensity of the peaks depends on the chemical composition and the position is related to diffraction angles and distance between the successive crystallographic plans in the crystal lattice. The diffraction angles depend on the Bravais point lattice and the unit cell dimensions; the diffracted intensities depend on the atomic numbers of the constituent

atoms and their geometrical relation with respect to the lattice points. The distance between lattices can be calculated by the wavelength and incident angle from the Bragg's law as follow

$$n\lambda = 2d_{hkl}\sin\theta \qquad \textbf{Equation 4-1}$$

where λ is the wavelength of the radiation, d_{hkl} is the spacing between the atomic lattices, and θ is the angle between incident ray and the scattering planes. In cubic system, the d value can be obtained as follow

$$\mathrm{d} = \frac{\mathrm{a}}{\sqrt{\mathrm{h}^2 + \mathrm{k}^2 + \mathrm{l}^2}} \qquad \textbf{Equation 4-2}$$

The XRD measurement was executed by Bruker D8 advanced running in Bragg-Brentano geometry with Cu K α1 (λ = 1.5406 Å) in a 2θ-range of 10°-90°. The software DIFFRAC plus was used to analyze the XRD data and the patterns were indexed and compared by the database from ICCD (International Centre for Diffraction Data).

4.2.2. X-ray Rietveld refinement analysis

Rietveld refinement is a technique devised by Hugo Rietveld for use in the characterization of crystalline materials. In the polycrystalline samples, it is inevitable that some information lost due to the random orientation of crystallite sites [91]. In practical powder X ray diffraction, the inherent of overlapping reflexions limits the XRD pattern information to directly used to refine the structural parameters [92]. The solution for these limitations is to make the Rietveld refinement which includes the whole data in the least-squares refinement the integrated intensities of the composite diffraction peaks. In principle, the Rietveld refinement is to minimize the deviation M between the calculated pattern (calc) and measured data (obs) by the equation

$$\mathrm{M} = \sum_{\mathrm{i}} \mathrm{W_i}\left(\mathrm{y_i^{obs}} - \frac{1}{\mathrm{c}}\mathrm{y_i^{calc}}\right)^2 \qquad \textbf{Equation 4-3}$$

Where W_i is the statistical weight and c is the overall scale factor when $y_i^{obs} = y_i^{calc}$. Rietveld refinement was carried out by the software GSAS in this work. Selected parameters were refined, including scale factor, zero point, profile coefficient, cell parameter, site fraction, thermal factor and atomic occupation. There are three quality parameters χ, R_{wp} and R_p which can judge how good the fitness is. X denotes the "goodness of fit" defined by the function [93] as

$$\chi^2 = \frac{\mathrm{M}}{\mathrm{N_{obs}} - \mathrm{N_{var}}} \qquad \textbf{Equation 4-4}$$

where N_{obs} is the total number of observations in all histograms, N_{var} is the number of variables in the least squres requirement. R_{wp} and R_p is the residue functions to evaluation the least squres refinement. In practice, χ, R_{wp} and R_p should be as low as possible.

4.2.3. Scanning electron microscopy (SEM)

SEM (Scanning electron microscope) is a type of device which utilizes the high energy electron beam to scan the surface of samples. The electron beam interacts with atom can excite different signals from the sample e.g. Secondary electron (SE), Backscattered electron (BSE), X-Ray and Auger Electron etc. According to these signals, we can obtain the information about the topography, chemical element and composition of the sample.

In this work, a scanning electron microscopy (FEI Quanta 200 FEG-ESEM) was utilized to characterize the morphology and microstructure of the samples. The samples were characterized in both low vacuum and high vacuum (10^{-5} Pa) mode. In low vacuum, water is introduced in the SEM inspection chamber which virtually eliminated charging effects of non-conducting samples.

4.2.4. Energy Dispersive X-ray spectroscopy (EDS)

The SEM used in this work was also equipped by an energy dispersive X-ray spectroscope (EDS). Energy-dispersive X-ray spectroscopy (EDS or EDX) is an advanced analytical device to characterize the chemical compositions in a sample. The main principle of this technique is to use an incident electron beam to emit the electrons located in different electron shells of vary elements in the form of X-ray. The electrons in the inner shell need more energy to be emitted to be free electrons while the electrons in the outer shell always need less energy. The free electrons are emitted in the form of X-ray spectrum which can be detected by the EDS spectrometer. Elements with different atomic numbers exhibit unique peaks corresponding to the electron relaxing from the different shells.

4.3. Apparatus

4.3.1. Electrical measurement cell

The electrical properties of NCO, NCCO5, GCO, and GCCO5 were characterized by the measurement cell (Probostat, NorECs As) under the gas tight environment, as shown in Figure 4.5.

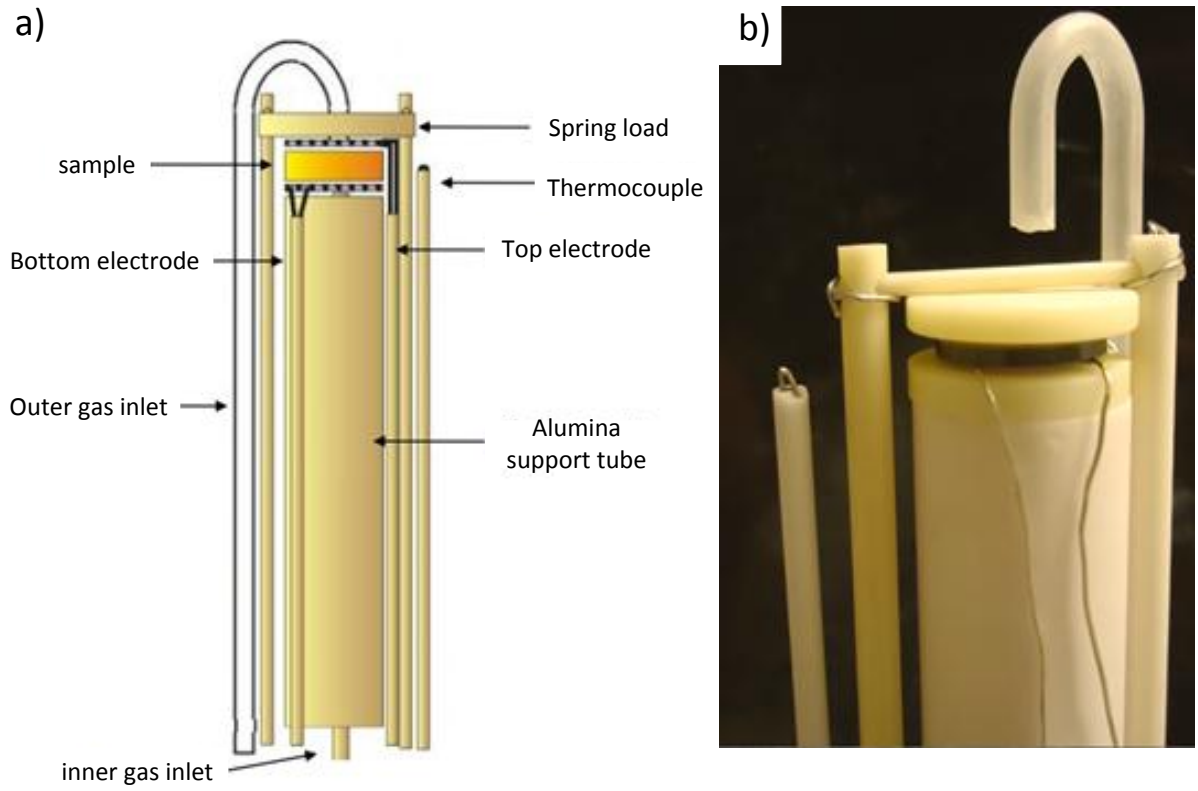

Figure 4.5 a) Schematic of the Probostat cell (without outside quartz tube) used in this work b) a photo of the measuring cell with a mounted sample.

The pellet was located at the top of the alumina support tube accompanied by two electrode contacts linking to the top electrode and bottom electrode separately. The sample was fastened by a series of spring loads. Gas flowed into the system by inner gas inlet and outer gas inlet. The temperature was controlled by an S-type thermocouple (at high temperatures) or a K-type thermocouple (at low temperatures). The setups were sealed by an outer quartz tube with a rubber O-ring.

4.3.2. Gas mixer

The gas atmosphere in the cell was controlled by an in-house build gas mixer, as shown in Figure 4.6. The gas mixer can control the oxygen partial pressure (pO_2) by diluting the gases O_2, 5%H_2 in Ar (Harmix), or hydrogen with several inert gases such as N_2, Ar, and He.

The gas mixer was composed of nine meters (A-I) which were divided into 4 pairs and one single. The two different gases initially flowed into the first pair flow meters A and B followed by the mixed gases. Similarly, the first mixed gas (MIX1) was further diluted in the following pairs MIX2 and MIX3. The last pair of flow meter G/H was used to control the water vapor partial pressure of the mixed gas. The last single flow meter I can adjust the amount of the gases flowed into the cell. Four bubble columns filled with dibutyl phtalate (B1-B4) were connected to MIX1, MIX2, MIX3, and MIX4, respectively. The bubbling in the column can illustrate the pressure of the corresponding mixed gas is constant. After gas one (G1) and gas two (G2) have been mixed for three times, the following mixed gas (MIX3) can be altered to flow through a wetting stage or a drying stage. The wetting stage consists of a series bottles filled with H_2O/D_2O solvent saturated by KBr water/heavy water solution separately. The water vapor partial pressure (pH_2O) of the gas is maintained around 0.03atm after the gas flows through the wetting stage. Similarly, MIX3 can be dried by flowing through a column filled with P_2O_5. The gas flow rate can be observed via the height of the metallic ball in the flow meter. In this work, there are two types of flow meters. One is equipped with a tantalum ball inside and the other one has a much lighter glass ball inside. If the two flow meters show the same flow height, the gas flow rate in flow meter with tantalum ball is around five times as that within glass ball. pO_2 or pH_2O can be calculated by the software Gasmixer 0.5000.

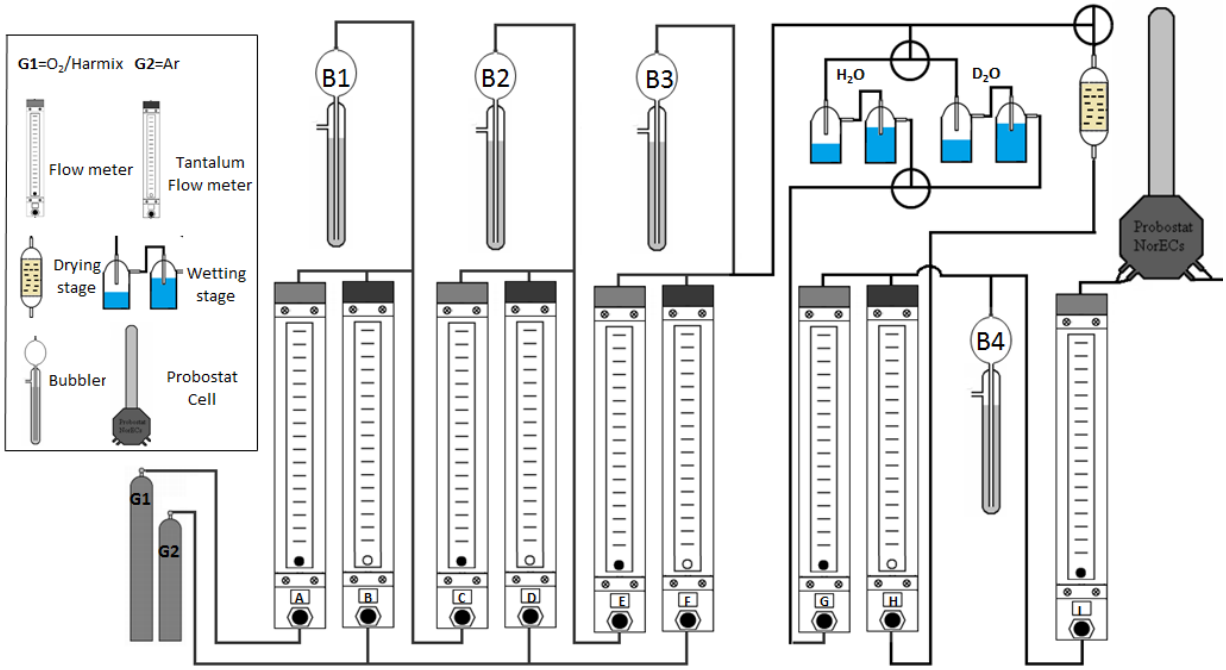

Figure 4.6 Schematic of the in house build gas mixer.

4.3.3. Thermogravimetry

Thermogravimetry was utilized to measure the mass change of the samples in different atmospheres. The instrument used in this work is Netzsch STA 449 F1 Jupiter-simultaneous TGA. The TG system consists of an evacuating system, a high water vapor pressure furnace and a hoisting device. The evacuating system is equipped with three different gas paths. As shown in Figure 4.7, there are three gas paths linking to the chamber. Different types of gases can flow into the TG from purge 1 and purge 2. In this work, purge 2 was closed because measurement was carried out in constant atmosphere. The protective gas path flushed by the dried gas in purge 1/purge2 has the function of protecting the system, especially when the instrument is operated at high temperatures. The type of gases and the flow into purge1/purge2 can be controlled by a gas mixer.

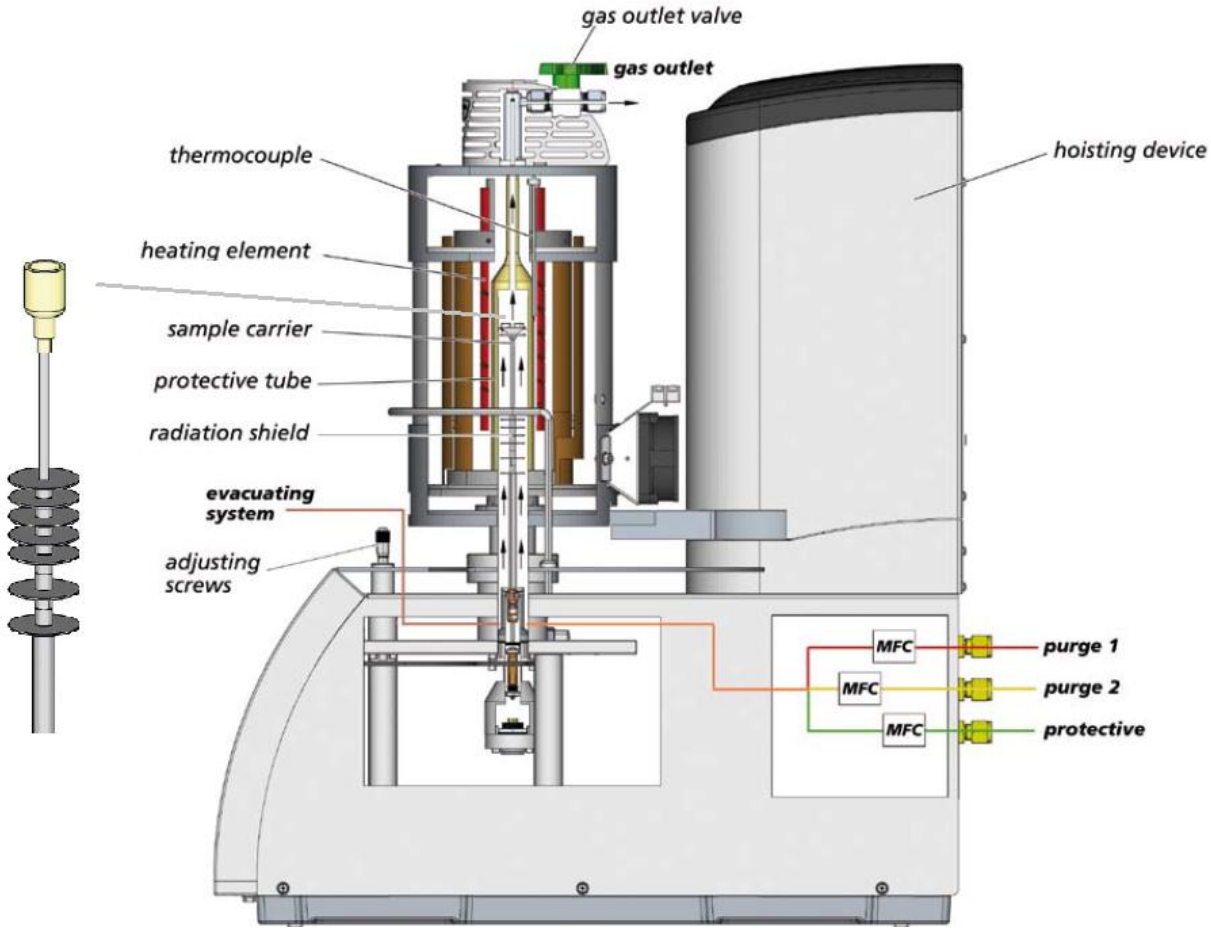

Figure 4.7 Schematic of the thermogravimetric analyzer (TGA) used in this work [95] .

First of all, in order to correct the systematic errors and the buoyancy, blank controls with empty sample holder should be carried out before the measurement. In general, crucible without any samples was measured under the same conditions and temperature profile as normal measurement to check the mass change from the thing except the samples.

Afterward, the powder sample was removed into the crucible. It is worth noting that the mass of the sample must not exceed 2.8g. Taken isothermal TG measurement from 1100°C to 300°C in wet air as an example, the measurement was carried out under wet air (pH_2O=0.02atm) by following the programmed temperature profile, which is described in Figure 4.8. After measurements, results will be analyzed by the software Proteus Analysis.

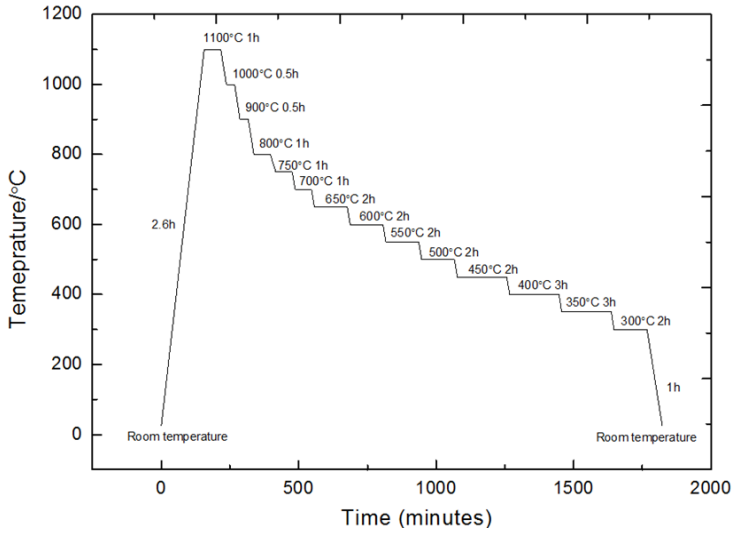

Figure 4.8 Temperature profile in the thermogravimetric measurement of GCO, GCCO5, NCO and NCCO5.

4.4. Electrical measurements

4.4.1. Two-probe four-wire measurement

A two probes four wires method was used in the electrical measurements. In this method, the resistance of the wires in the circuit is removed from the measured impedance. Only the resistance of the electrodes and the samples are measured, as shown in Figure 4.9.

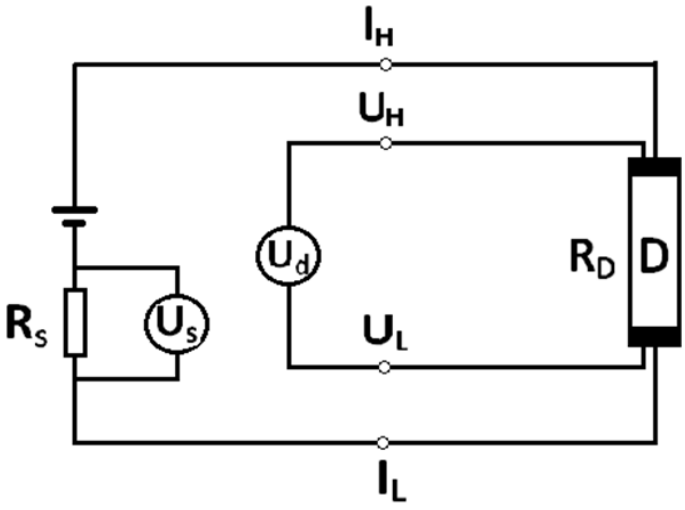

Figure 4.9 Schematic of a two-probe four-wire electrical measurement.

As shown in Table 4.3, the basic instrumental characteristics of the impedance spectrometers in this work are summarized. The conductivity of samples NCO, NCCO5, GCO, and GCCO5 were measured by these devices. Sometimes HP4192A cannot precisely measure the sample with high resistance at low temperatures due to the limitation of the impute impedance. In order to obtain better results, another two impedance spectrometers Novocontrol α-A and Solartron 1260 were also utilized in this work. In practice, the data at the low frequency measured by Novocontrol and Solartron perform much better than the data from the HP4129A. In particular, Novocontrol α-A can measure relatively high resistance samples because of the high imput impedance.

Table 4.3 Instrument characteristics of the impedance spectrometers used in this work.

Device	Frequency range	Imput impedance	DC bias	Ac amplitude
HP4192A	5 Hz – 13 MHz	1 MΩ	up to 40 V	5 mV – 1.1 V (rms)
Solartron1260	10 μHz – 32 MHz	1MΩ	up to 41 V	5 mV – 3 V (rms)
Novocontrol α-A	30 μHz – 20 MHz	1 TΩ	up to 40 V	0.1 – 3 V (rms)

The conductivity of the sample was measured directly with the geometric correction by the system.

$$\sigma_g = G\frac{d}{\pi r^2} \qquad \textbf{Equation 4-5}$$

Where σ_g denotes the conductivity measured by the instrument; G represents the conductance; d is the thickness of the sample and r is the radius of the electrodes. The final conductivity was correct by the relative porosity by the empirical equation, which gives

$$\sigma_f = \frac{\sigma_g}{\rho^2} \qquad \textbf{Equation 4-6}$$

Where σ_f is the conductivity corrected by the relative density, ρ is the relative density. However, the uncertainty of the empirical equation becomes much larger with the reducing relative density.

In addition, the software EQC was utilized to fit the experimentally obtained impedance spectra with respect to the modeled data from the equivalent circuit. Above all, the data can be validated by the Kramers-Kronig (K-K) transformation test in the software. The quality of the test is evaluated by a quality value χ^2which is in the order of 10^{-7}. According to the manual, values below 10^{-6} means good data. This test helps in excluding unreasonable points.

4.4.2. Two-probe three-wire measurement (Sandwich measurement)

GCO and GCCO5 are measured at the same time by using the two points three wires measurement. As shown in Figure 4.10, two samples were stacked on the alumina support tube with separated by an alumina pellet in the middle. It is beneficial to measure the two samples at the same time. However, compared with two-probe four-wire measurement, it can just diminish the resistance of wires at one side. Therefore, the total conductivity should be contributed from the sample, two electrodes and a length of wire in this case. Since the resistance of the sample is generally much higher than that of a length of wire, the errors in this measurement are thereby acceptable. In addition, the thermocouple was located in the middle of the two samples, which will introduce error of temperature reading.

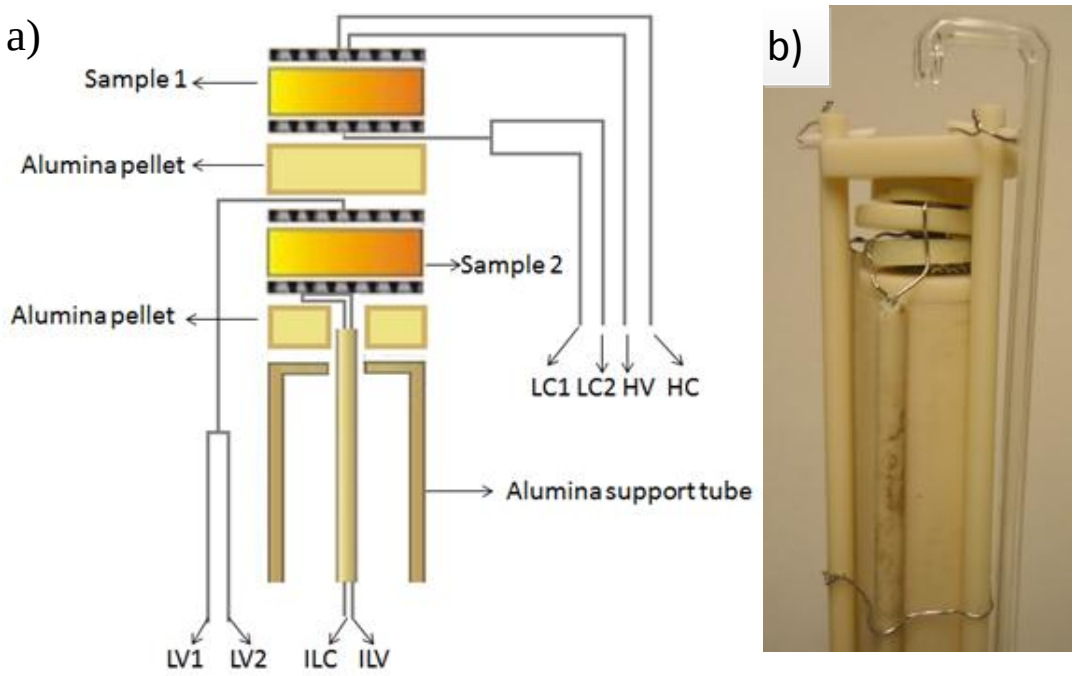

Figure 4.10 a) Schematic of the measurement of two samples by using two-probe three-wire measurement (Sandwich measurement) b) a picture of the sandwich measurement.

4.4.3. Low temperature measurement

Figure 4.11a displays the electrical measurement setup carried out under freezing point and b presents the circuit inside the measurement cell. A low temperature electrical measurement was carried out in order to investigate the electrical properties of samples in low temperatures. Above all, in order to precisely measure the temperature, type-k thermal couple (90% nickel and 10% chromium) was used in the measurement. The ProboStat cell was turned upside down and was inserted into a bottle contains liquid nitrogen.

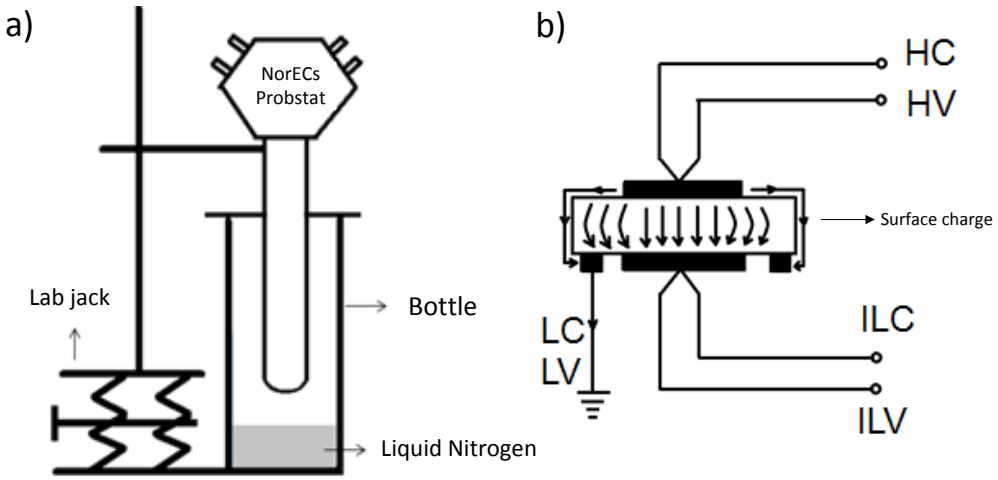

Figure 4.11 a) The schematic of the sample measured under freezing point b) the schematic of the circuit inside the cell

As shown in Figure 4.11a, the temperature can be controlled by adjusting the height between the cell and liquid nitrogen via the lab jack. As shown in Figure 4.11b, the two probe four-wire measurement was carried out to measure the conductivity of the sample and the surface charge results from the water can be conducted through the guard electrode to the ground. The guard electrode can be set open or close by turning corresponding switch in the Probostat Cell. The electrical conductivity was measured by Solartron 1260 at the constant frequency of 10 kHz and the sweep was taken at the frequency range from 32MHz to 1Hz. In this measurement, the data was recorded by the software Omega.

4.5. Errors and uncertainties

During experiments, it is inevitable to introduce some errors and uncertainties. Therefore, it is important to concern these factors and take measures to reduce or even eliminate them. The errors and uncertainties will be discussed with respect to several aspects including gas mixer, thermogravimetry, electrical measurement, XRD and SEM-EDS.

Leakage is a typical problem that always happens in the gas mixer and the Probostat cell. The leakage will attribute to some uncertainties in the composition of the gas which might result in errors in the electrical measurement. In addition, since the permeability of the alumina or quartz tubes, pH_2O in dry gases is estimated to be 3×10^{-5} atm [96, 97] which can be different from the real value. pH_2O can be affected by the temperature of the wetting stage, the uncertainty should be considered if the temperature of wetting stage changes a lot. pH_2O will not influence on the partial pressure of other gases too much. It is estimated that partial pressure of gases will decrease by 3% from dry to fully wet gas [98], which are negligible in this work. In addition, the uncertainties from the gas flow meter also vary

regarding the different flow rates. The uncertainties are about 5% if the flow rate is over 60mm, but the uncertainties jump to 60% if the flow rate is less than 20mm [99]. Therefore, the gas flow rate should keep over 20mm in order to reduce the uncertainties from the flow meter in the measurement.

There are also some uncertainties in the electrical measurement which are necessarily to be aware of. First of all, since the imperfect round shaped electrodes was normally prepared on the samples, some uncertainties might be introduced from the calculation of the electrode areas. However, this uncertainty can be reduced by taking the average value of diameters measured for several times. Also, the unsymmetrical positions or not perfect circle of the two electrodes might also lead to some errors. Secondly, thickness of the sample might not be homogeneous after being polished by the sand paper. The errors from the thickness of the samples can be also reduced by taking the average results measured in different parts. Also, the system errors resulting from the reading values of screw micrometer do exist, but not that significant. Thirdly, the uncertainties from reading the thermocouple was estimated to be $\pm 2.5℃$ for K type from 0°C to -100°C and $\pm 1℃$ for S type from 1000°C to 0°C [100].

There are several systematic errors in the XRD characterization. Firstly, the orientation of the specimen may lead to some errors in the XRD result which is inevitable. Secondly, the instrumental error can result in some deviation of the zero 2θ position. In principle, the best way to diminish the systematic errors is to add some internal standard into the specimen.

The uncertainties from SEM-EDS vary. If the concentration of the secondary phase is low or homogeneously disperses among the sample, the SEM cannot distinguish the secondary phase due to the low resolution. For EDS, the contamination on the detect window can significantly reduce the energy of incoming X-ray and effect the lower energy which will result in erroneous counting with the too low elemental composition [94].The EDS spectrum of samples in this work will be shown in the Chapter 5.

For the thermogravimetry measurement, the buoyancy of the gas in different temperatures varies. If the mass change of the sample is close to the mass change results from buoyancy, the uncertainties of the TG measurement might be larger. Therefore, it is necessary to do a blank control before each measurement. In addition, results of TG are generally with some noise. Smoothing the result by the software (Netzsch Proteus) will introduce some errors. The raw data should be exported and analyzed afterward. Also, the uncertainties of the thermo balance are $\pm 0.05\mathrm{mg}$ which is too small to be taken into account.

5. Results

In this section, XRD patterns and SEM-EDS results of the materials NCO, NCCO5, GCO and GCCO5 are presented. Rietveld refinements give information about the cell parameters of the samples. After that, results about electrical measurement of NCO, NCCO5, GCO and GCCO5 at high and low temperatures are displayed, including selected impedance spectra, temperature dependency, pO_2 dependency, pH_2O dependency and some modeled results. In addition, results regarding thermogravimetry are emphasized on NCO and GCO. In the final part, results measured at low temperatures are presented.

5.1. Sample characterization

5.1.1. XRD patterns

Figure 5.1 presents the XRD pattern of NCO and GCO. The patterns display that the two materials exhibit very similar crystal structure. The crystal structure of NCO is characterized to F-type structure while GCO exhibits a C-type related crystal structure which is a derivative of the F-type structure. The small peaks marked by red circles origin from the superstructure reported by Patwe [41], as previously mentioned in Chapter 3.

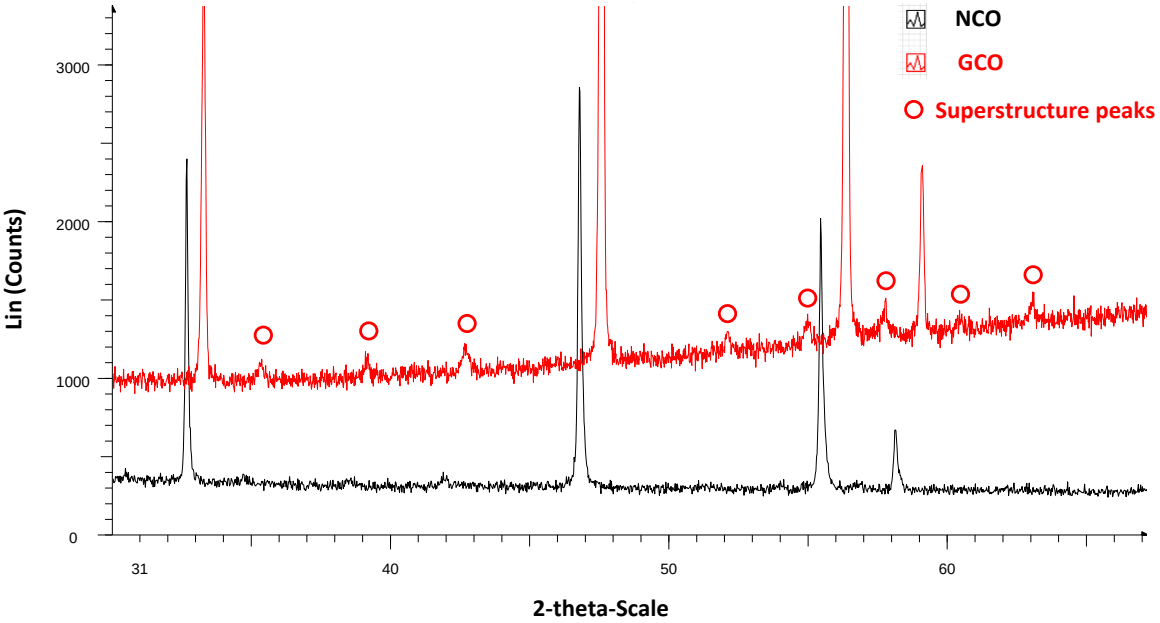

Figure 5.1 XRD patterns of NCO and GCO measured at room temperature.

Figure 5.2 displays the XRD patterns of doped and undoped NCO and NCO synthesized at 800°C for 10 hours. All compositions crystallize in the cubic F-type oxide structures within the Fm-3m space group. All the six samples were synthesized at 800°C for 10 hours. With increasing concentration of dopants, no secondary phase was found from the XRD pattern. Furthermore, not obvious peak shift is detected with respect to NCO and doped NCO.

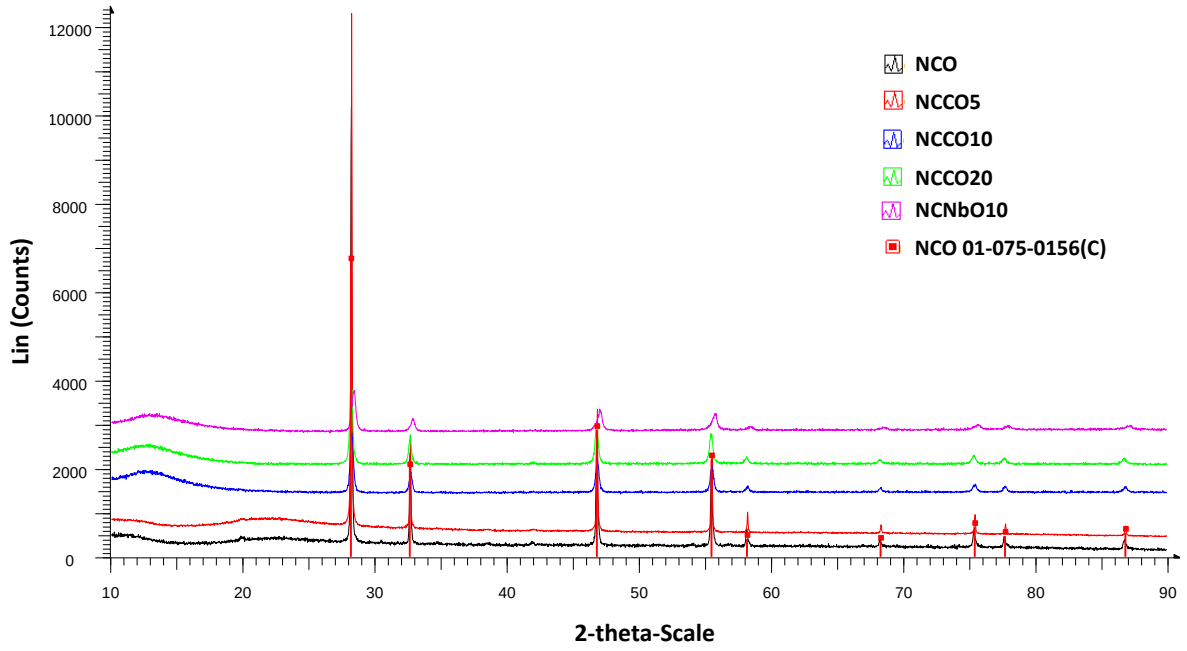

Figure 5.2 XRD patterns of NCO, NCCO5, NCCO10, NCCO20 and NCNbO10 calcined at 800°C for 10 hours.

Figure 5.3 presents the XRD patterns of GCO and doped GCO. All patterns match the reference pattern [39] meaning that the crystal structure change did not change with increasing dopant concentration. Furthermore, no secondary phase can be detected from the XRD patterns. However, some peaks did not appear at the corresponding position of the reference patterns, as marked by the arrows.

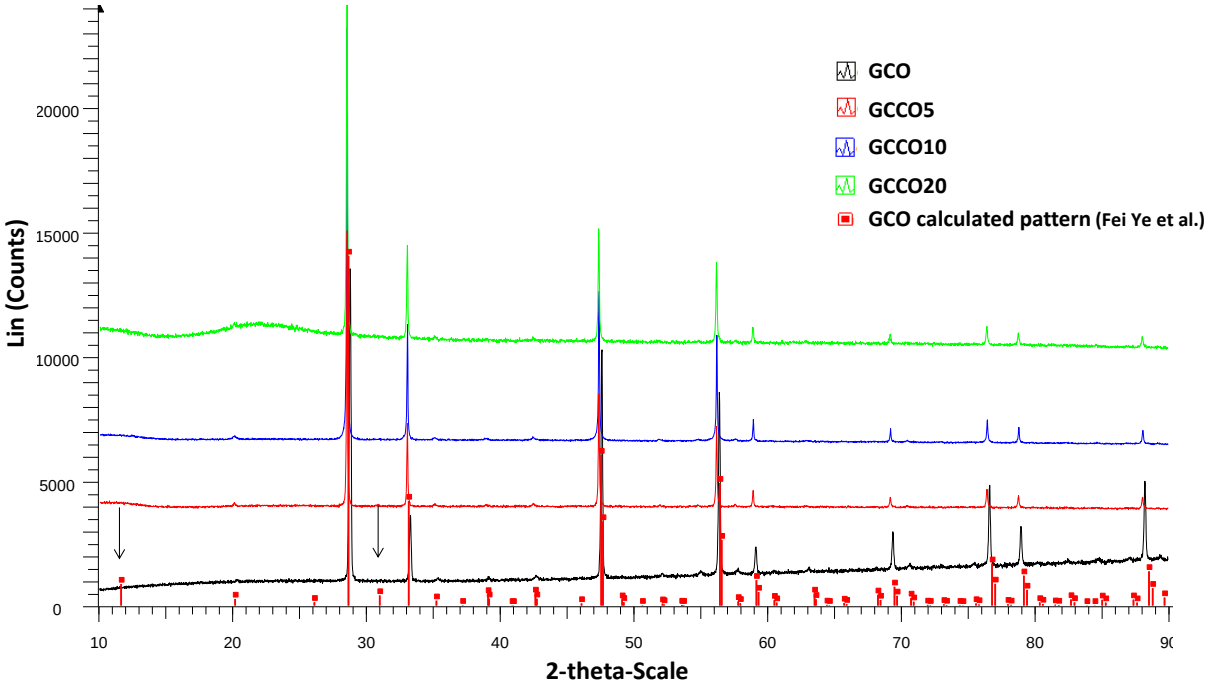

Figure 5.3 XRD patterns of GCO, GCCO5, GCCO10 and GCCO20 measured at room temperature, calcined at 800°C for 10 hours.

This could be expected as some of the superstructure lines are known to be rather weak [28]. Also, those superstructure peaks will weaken if the samples consist of both F-type phase and C-type phase in the material.

5.1.2. X-ray Rietveld refinement

As can be seen from Figure 5.4, the difference between the calculated and measured pattern is small due to the weak noise. Also, quality factors R_p, R_{wp} and χ suggest the result is valid. Therefore, the XRD pattern of NCO can be satisfactorily fitted within the space group Fm-3m. According to the literature [50], the oxygen ions are considered to be totally disordered in the Fm-3m with occupation of 0.875. Since the XRD pattern of NCO can be fitted by this structure model, the oxygen ion in the sublattice can also be regarded as totally disordered as well.

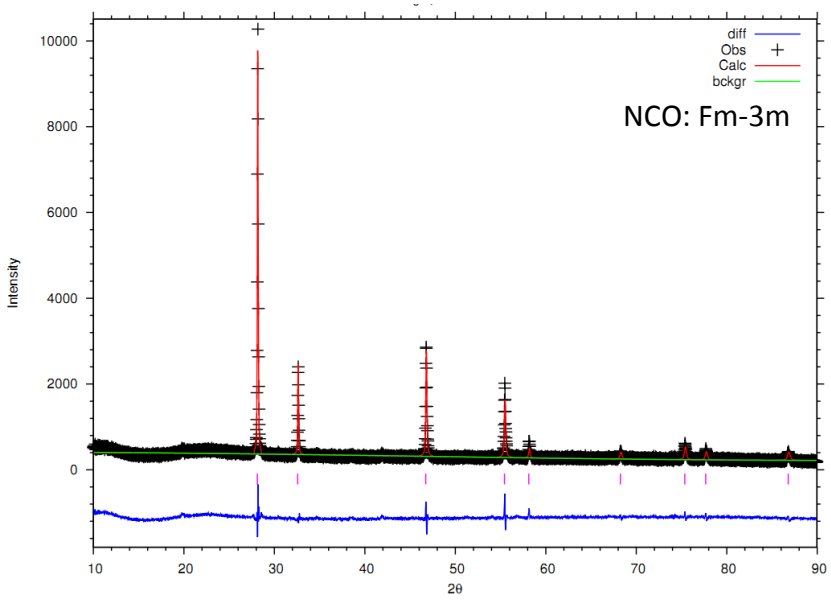

Figure 5.4 Intensity vs. 2θ of the powder XRD patterns of NCO. The vertical red lines mark the Bragg peaks according to the space group Fm-3m. The red line is the calculated pattern, the green line is the background line, and the bottom blue line is the difference.

Table 5.1 Crystal parameters of NCO obtained from the Rietveld refinement corresponding to Figure 5.4.

Atom	Wyck.	x	y	z	U	Occupancy (n)
Nd1	4a	0.0	0.0	0.0	0.29626	0.4923
Ce1	4a	0.0	0.0	0.0	0.02075	0.5032
O1	8c	0.25	0.25	0.25	0.07307	0.8654
a(Å)	5.9287(21)	V(Å^3)	165.729(11)			

Space group $Fm\bar{3}m$, R_p (%) = 15.15, R_{wp} (%) = 10.84, χ^2 =4.051

Figure 5.5 shows the Rietveld refinement of the XRD patterns of GCO recorded at room temperature. The pattern of GCO is fitted by the cubic structure within the space group Fm-3m (a) and $I2_13$ (b), respectively.

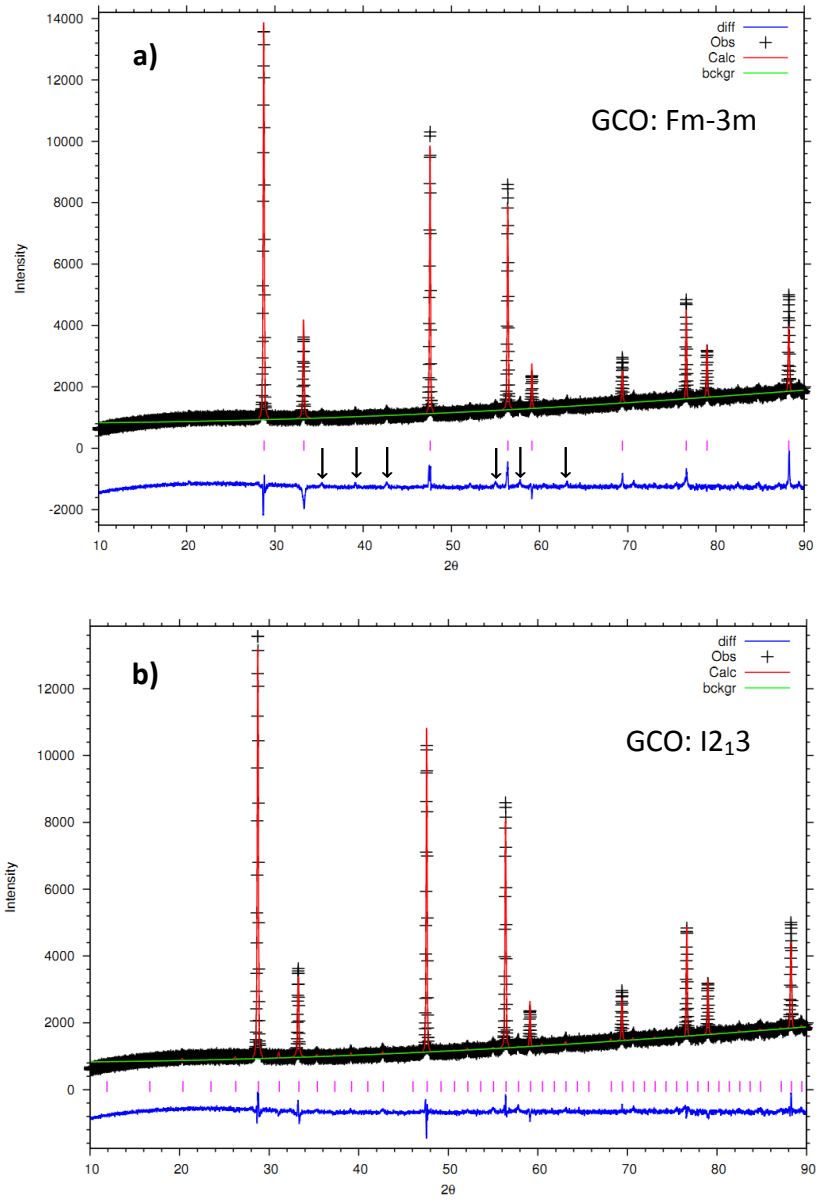

Figure 5.5 Rietveld refinement of $Gd_2Ce_2O_7$ fitted by Fm-3m space group (a) Fm-3m (b) $I2_13$.

In this case, GCO might be formed by mixed F-type and C-type phases, but it is hard to obtain the relative composition of the two phases by fitting. From Figure 5.5, although the main peaks can be well fitted, but there are several low intensity peaks cannot be well fitted (marked by arrows). Furthermore, the lower value of quality factors χ, Rwp, Rp in $I2_13$ reflect that the space group $I2_13$ fit better than Fm-3m. On the other hand, since the strong superstructure peaks were detected in the XRD pattern, C-type was believed to be the predominating phase in GCO. The atomic positions, occupancy and thermal factor obtained from the Rietveld refinement are summarized in Table 5.2 and 5.3.

Table 5.2 Parameters obtained from the Rietveld refinements corresponding to Figure 5.5a, occupancy are kept constant.

Atom	Wyck.	x	y	z	U	Occupancy (n)
Gd1	4a	0.0	0.0	0.0	0.00056	0.500
Ce1	4a	0.0	0.0	0.0	0.02530	0.500
O1	8c	0.25	0.25	0.25	0.02500	0.875
a(Å)	5.43787(8)	V (Å^3)	160.800(4)			

Space group $Fm\bar{3}m$, R_p (%) = 16.11, R_{wp} (%) = 6.27, χ^2 =5.212

Table 5.3 Parameters obtained from the Rietveld refinement corresponding to Figure 5.5b.

Atom	Wyck.	x	y	z	U	Occupancy (n)
Gd1	8a	0.25	0.25	0.25	0.0340	0.30
Ce1	8a	0.25	0.25	0.25	0.0253	0.50
Gd2	12b	0.49	0	0.25	0.0161	0.65
Ce2	12b	1	0	0.25	0.0057	0.80
O1	24c	0.40	0.11	0.38	0.0120	0.96
O2	24c	0.62	0.87	0.62	0.0015	1
O3	8a	0.39	0.39	0.39	0.0016	1
a(Å)	10.87198(20)	V(Å^3)	1285.07(4)			

Space group $I2_13$, Rp (%) = 13.28, R_{wp} (%) = 5.39, χ^2 =3.84

The oxygen ions in C-type phase of GCO tend to occupy three certain sites (cf. Table 5.3) with occupation close to 1. Cations in GCO were also found to be disordered. When fitted to F-type phase of GCO, similar as NCO, oxygen ions in GCO are totally disordered with the occupation of 0.875. Nevertheless, one should note that results from the Rietveld refinement support some information about the crystal, but this refinement is limited by the quality of the XRD pattern. In practice, the thermal factor U will seriously impact on the value of occupation, the uncertainty of the result might be large. Based on the analysis, GCO is believed as C-type structure at room temperature in this work.

The lattice parameters of NCO and GCO obtained by the refinement are plotted as a function of the dopant concentration in Figure 5.6. As can be seen in Figure 5.6a, lattice parameter of NCO increases with increasing doping concentration up to x=0.1 where it flattens out. On the other hand, lattice parameter of GCO (cf. Figure 5.6b) changes as a function of the dopant concentration and the data is linearly fitted by the following formulation:

$$a = 0.015x + 10.87 \qquad \textbf{Equation 5-1}$$

Where a represents the cell parameter, x is the dopant concentration.

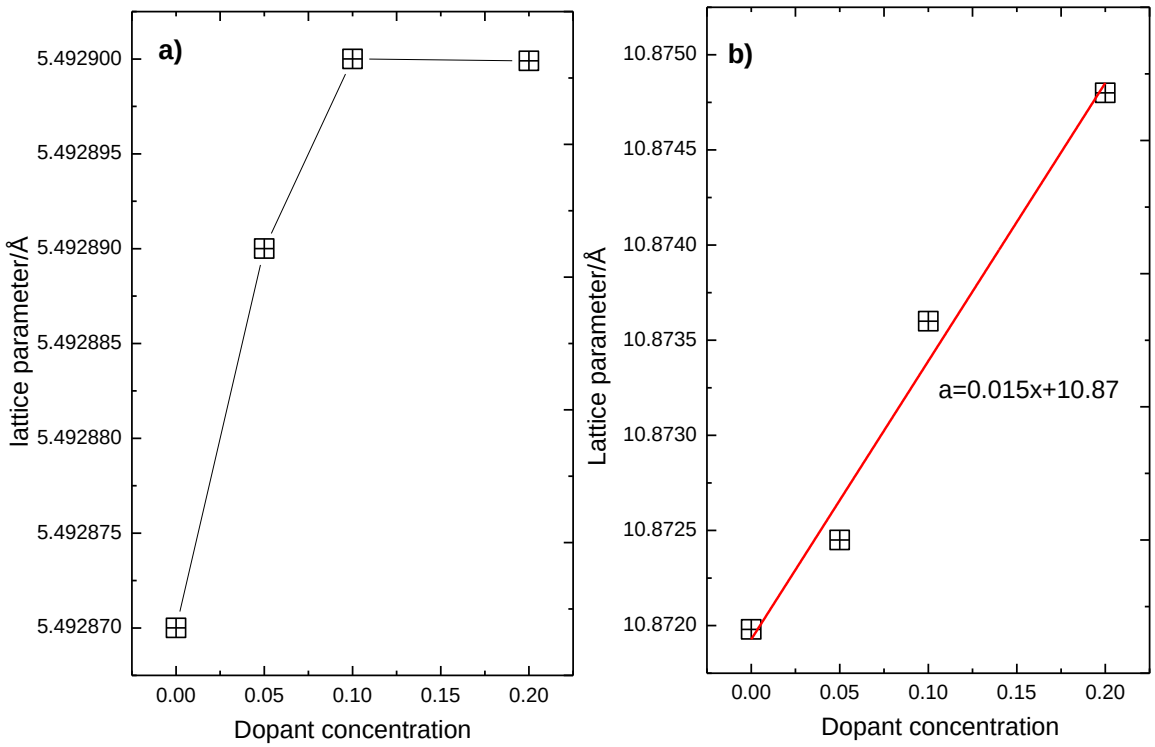

Figure5.6 a) Cell parameter versus concentration of dopant in $Nd_{1-x}Ca_xCe_2O_{7-\delta}$ $(0 \leq x \leq 0.2)$ b) $Gd_{1-x}Ca_xCe_2O_{7-\delta}$ $(0 \leq x \leq 0.2)$.

This result follows Vegard's law which is an empirical principle often found in solid solutions. It demonstrates the unit cell of GCO becomes bigger with increasing dopant concentration when x<0.2. Nevertheless, parameters of NCO indicate the lattice parameter becomes independent of the composition parameter when x>0.1 indicating the calcium cannot doped in the lattice of NCO when it comes to the high concentration.

5.1.3. Scanning electron microscopy (SEM)

Figure 5.7 represents the MIX images (BSE and SE) of NCCO10 and NCCO20 sintered samples whose powders were synthesized by SSR and CPR, respectively. It is obvious that the samples synthesized by SSR (cf. Figure 5.7a and b) are quite porous while the samples prepared by CPR (cf. Figure 5.7c and d) are relatively dense. It is mainly due to the much smaller particles obtained by wet chemical method that helps atomic diffusion when sintering.

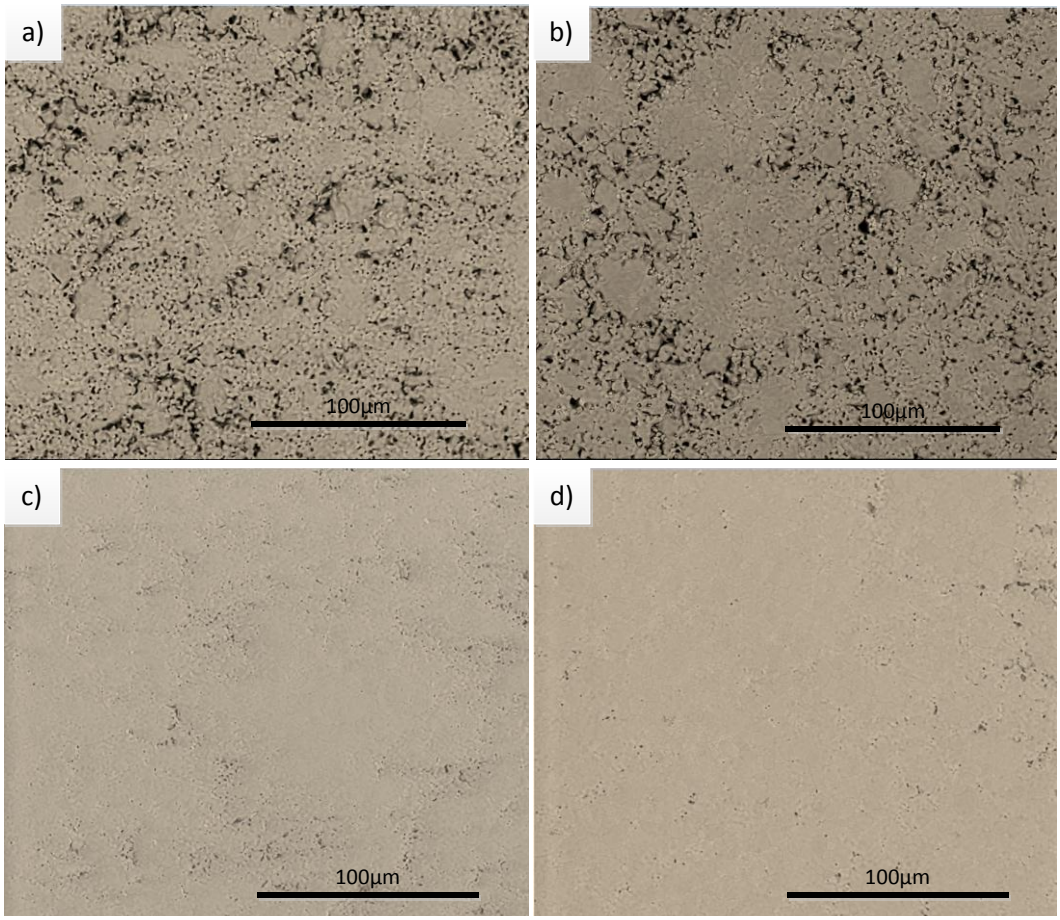

Figure 5.7 a) NCCO10 synthesized by SSR b) NCCO20 synthesized by SSR c) NCCO10 synthesized by CPR d) NCCO20 synthesized by CPR.

Figure 5.8 is MIX images (both BSE and SE images) of NCO and GCO showing the topography of the samples. Many holes distribute though the two samples meaning that both of them are fairly porous.

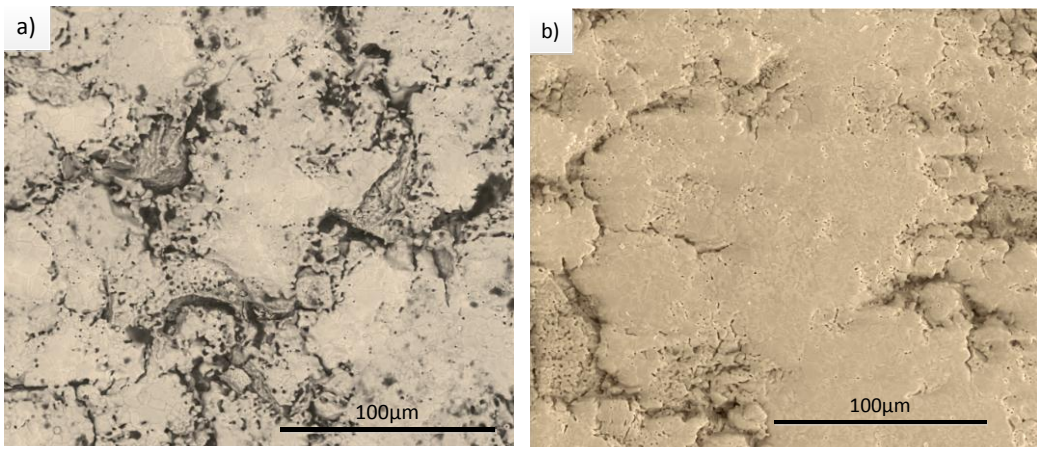

Figure 5.8 MIX images showing the topography of samples a) $Nd_2Ce_2O_7$ b) $Gd_2Ce_2O_7$.

Figure 5.9 displays the samples $Nd_{2-x}Ca_xCe_2O_{7-\delta}$ $(0 \leq x \leq 0.2)$ distributes after sintering at 1400°C for 5 hours. As can be seen in Figure 5.9, the images of 0%, 5% and 10% calcium doped samples illustrate pure single phase. However, some dots (marked by '2') are discovered along the grain boundaries which are identified by EDS as the secondary phases with relatively high composition of the calcium, as shown in Figure 5.10.

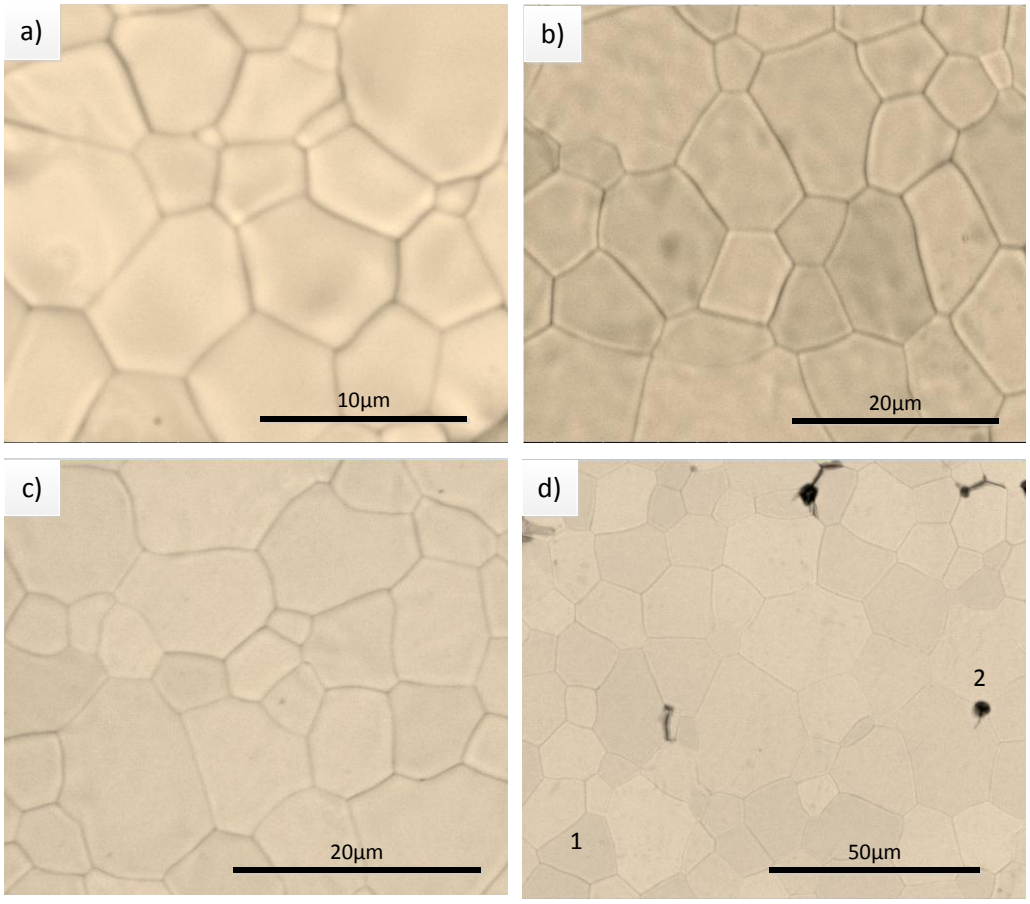

Figure 5.9 SSD images representing the grain size and purity of phases in grains a) NCO b) NCCO5 c) NCCO10 d) NCCO20 (A selected grain is marked by '1' and a black dot is marked by '2').

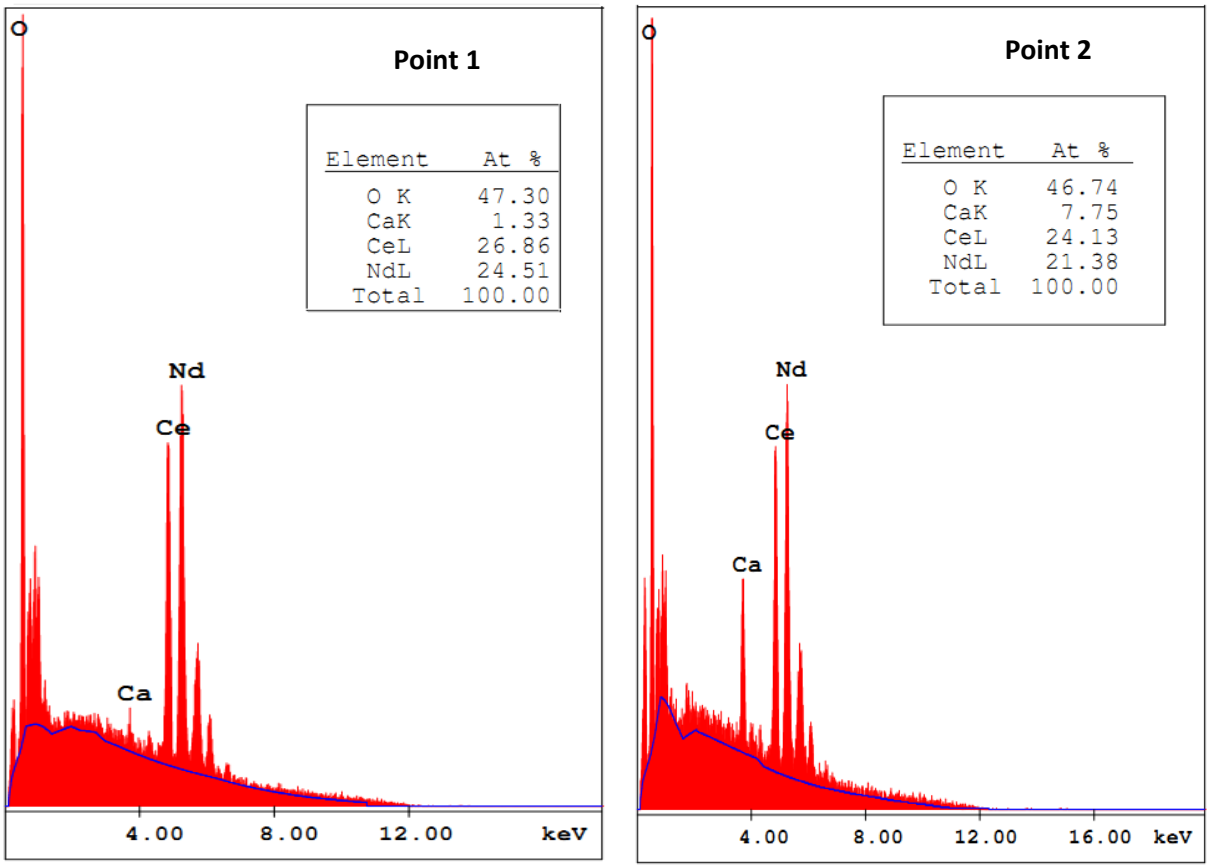

Figure 5.10 EDS results of point 1 and point 2 in Figure 5.9d.

In Table 5.4, the composition of samples of 0-10mole% calcium doped NCO follow the expected stoichiometry, but the bulk composition of 20mole% calcium doped NCO exhibit about 10.3mole% calcium in the bulk. Results indicate that not all the calcium can dissolve in the grain of NCO at 1400°C and solubility is expected up to 10mole%. This result matches the lattice parameter change in Figure 5.6a. Furthermore, the relative density is enhanced in the calcium doped samples because calcium can play a role as sintering aid. Moreover, the average grain size increases with increasing dopant concentration.

Table 5.4 Results from the EDS results of NCO in Figure 5.9.

Composition	Nd atom%	Ce atom%	Ca atom%	O atom%	Relative density%	Average grain size/μm
NCO	26.18	26.04	0(0 mole %)	47.78	74%	7
NCCO5	26.26	27.48	0.61(4.5mole %)	45.48	95%	6
NCCO10	23.86	25.59	1.34(10.6mole %)	49.20	95%	8
NCCO20	24.51	26.86	1.33(10.3mole %)	47.30	95%	15

Figure 5.11 are BSE images representing $Gd_{2-x}Ca_xCe_2O_{7-\delta}$ $(0 \leq x \leq 0.2)$ after sintering at 1400°C for 5 hours and the composition of the grain interior are summarized in Table 5.5.

Due to the contrast of the image, there is single phase in the four samples meaning that calcium completely dissolves in the grain interior.

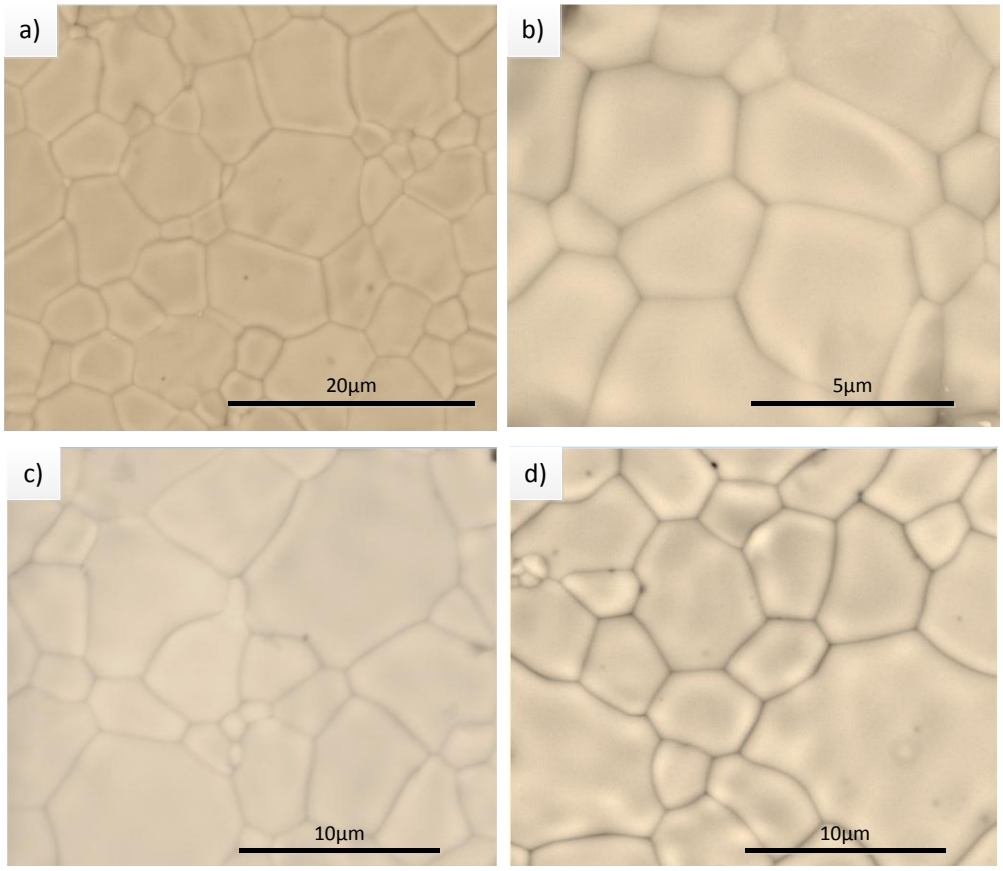

Figure 5.11 SSD images representing the grain size and purity of phase in grain (a) GCO (b) GCCO5 (c) GCCO10 (d) GCCO20.

Table 5.5 shows that the composition in the bulk is well matched with the expected stoichiometry. This result is in accordance the lattice parameter change (cf. Figure 5.6b). Similar as NCO, the relative densities of samples increase with increasing dopant concentration because of the calcium as a sintering aid.

Table 5.5 Results from the EDS results of GCO in Figure 5.11.

Composition	Nd atom%	Ce atom%	Ca atom%	O atom%	Relative density%	Average grain size/µm
GCO	25.59	25.76	0(0 mole %)	48.65	76%	6
GCCO5	24.54	24.99	0.61(4.9mole %)	49.86	87%	3
GCCO10	25.58	27.74	1.33(9.9mole %)	45.35	80%	3
GCCO20	23.57	26.03	2.52(19.3mole %)	47.88	89%	4

5.2. Electrical characterization

5.2.1. Impedance spectroscopy analysis (1000°C-300°C)

Selected impedance spectra of NCO, NCCO5, GCO and GCCO5 were recorded in the temperature range from 300°C to 600°C under various conditions. HP 4192 and Novocontrol were used to carry out the sweep at the frequency range from 1MHz to 1Hz. The constant frequency was chosen at 10 kHz, which are marked in each spectrum. It is worth note that all the spectra are subtracted by the parasitic capacitance from the measurement cell, which is estimated as 0.5pFcm^{-1} in this work.

Figure 5.12 presents the impedance spectra of all samples. In Figure 5.12a and c, from 300°C to 500°C in wet O_2, the impedance spectra was mainly composed of a complete semicircle and the semicircle became smaller with increasing temperature. For the impedance spectra including just one semicircle, the equivalent (R_1Q_1) was used to fit the result. From the deconvolution, the specific capacitance of each semicircle is in the pFcm^{-1} range, which is the typical range for the specific capacitance from the grain interior.

Figure 5.12b and d present the impedance spectra, measured under equilibrium condition in D_2O, H_2O and dry O_2 atmospheres. The two groups of spectra illustrate the distinct isotope effect of NCO at 450°C and GCO at 400°C. In Figure 5.12e, impedance spectra of NCO and GCO recorded in Ar and O_2 at 600°C were plotted in one graph. With increasing temperature, parts of the grain interior semicircle vanished because of the decreasing grain interior resistance. For GCO in Ar and O_2 at 600°C, two incomplete semicircles were found and they were deconvoluted by the circuit (R_1Q_1) (R_2Q_2) where the first section is from grain interior and the second one represents the electrodes. In addition, the impedance spectra in Ar and O_2 are almost overlapped, meaning that conductivity measured in Ar and O_2 were nearly the same. However, in impedance spectra of NCO at 600°C, the semicircle did not start in original point, indicating the grain interior semicircle was completely disappeared. In this case, the equivalent circuit is R_1 (R_2Q_2) where R_1 means the resistance of the grain interior and (R_2Q_2) is the electrodes due to the specific capacitance in the range of μPcm^{-1}. In addition, the impedance spectra over 700°C were generally similar as that of NCO at 600°C which are deconvoluted by R_1 (R_2Q_2).

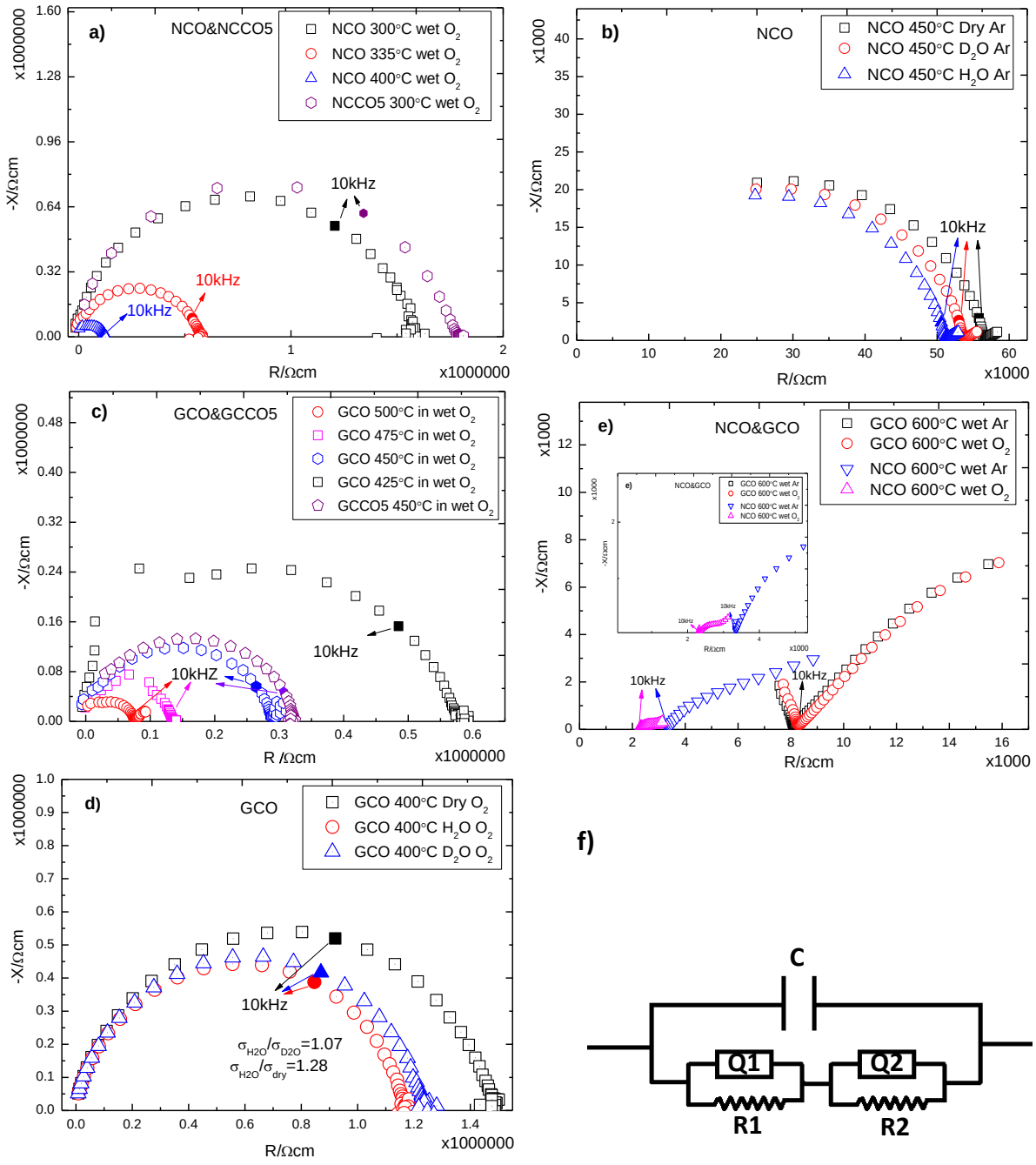

Figure 5.12 a) - e) Impedance spectra of GCO at various atmospheres at the frequency range from 1MHz to 5Hz. 10kHz as the oscillation frequencies were marked in each result. The results are deconvoluted by the equivalent circuit f and results are tabulated in Table 5.6.

According to the impedance spectra, no obvious semicircles originating from the grain boundaries are found in NCO and GCO. This indicates that the grain boundaries resistance is lower than the grain interior resistance. According to the literature [101, 102], both $Ce_{1-x}Nd_xO_{7-\delta}$ and $Ce_{1-x}Gd_xO_{7-\delta}$ ($0<x<0.2$) exhibited much higher grain boundary resistance than grain interior. Furthermore, the electrical conductance of grain boundary is proportional to the dopant concentration [103], so the low grain boundary resistance of NCO

and GCO might be ascribed to the relatively high doping level if they are treated as 50% Nd/Gd doped ceria. In particular, the impedance spectra of NCCO5 in 300°C was fitted by the parallel circuit $(R_1Q_1)(R_2Q_2)$, where the first one should be from the grain interior within specific capacitance around 3pFcm^{-1}, but the specific capacitance of the second circuit is close to 100pFcm^{-1} which is in the range of the capacitance of the grain boundary.

Table 5.6 presents the mean value of the specific capacitance and the relative permittivity of the bulk of these materials. The relative permittivity of GCO is higher than NCO and the permittivity of doped materials are lower than the undoped materials.

Table 5.6 Mean value of the specific capacitance and relative static permittivity of bulk obtained by deconvolution of the impedance spectra presented in Figure 5.12.

Composition	$\overline{C_{bulk}}$/pFcm^{-1}	$\bar{\varepsilon}$
NCO	4.58	52
NCCO5	3.05	34
GCO	5.77	65
GCCO5	4.78	54

5.2.2. Temperature dependency of the conductivity

Figure 5.13 displays the logarithm of the conductivity (10 kHz) as a function of inverse temperature in both wet and dry oxygen from 1100°C to 300°C. GCO and GCCO5 were measured in the "sandwich" setup. The data under 350°C is rather noisy because of the relatively high resistance. The four samples exhibit fairly similar behaviors: the total conductivity decreased with decreasing temperature and the slope become less steep at lower temperatures compared with higher temperatures. The conductivity of NCO and NCCO5 exhibit no difference in wet and dry oxygen meaning that humidity did not affect the conductivity. For the sample GCO and GCCO5, there is insignificant difference between wet and dry O_2 from 1100°C to 600°C, but a small difference can be detected under 600°C in GCO and GCCO5, meaning that total conductivity may be affected by humidity. In addition, as the impedance spectra analysis in section 5.2.1, conductivity of the four samples measured at 10 kHz is ascribed to be grain interior from 1100°C to 300°C.

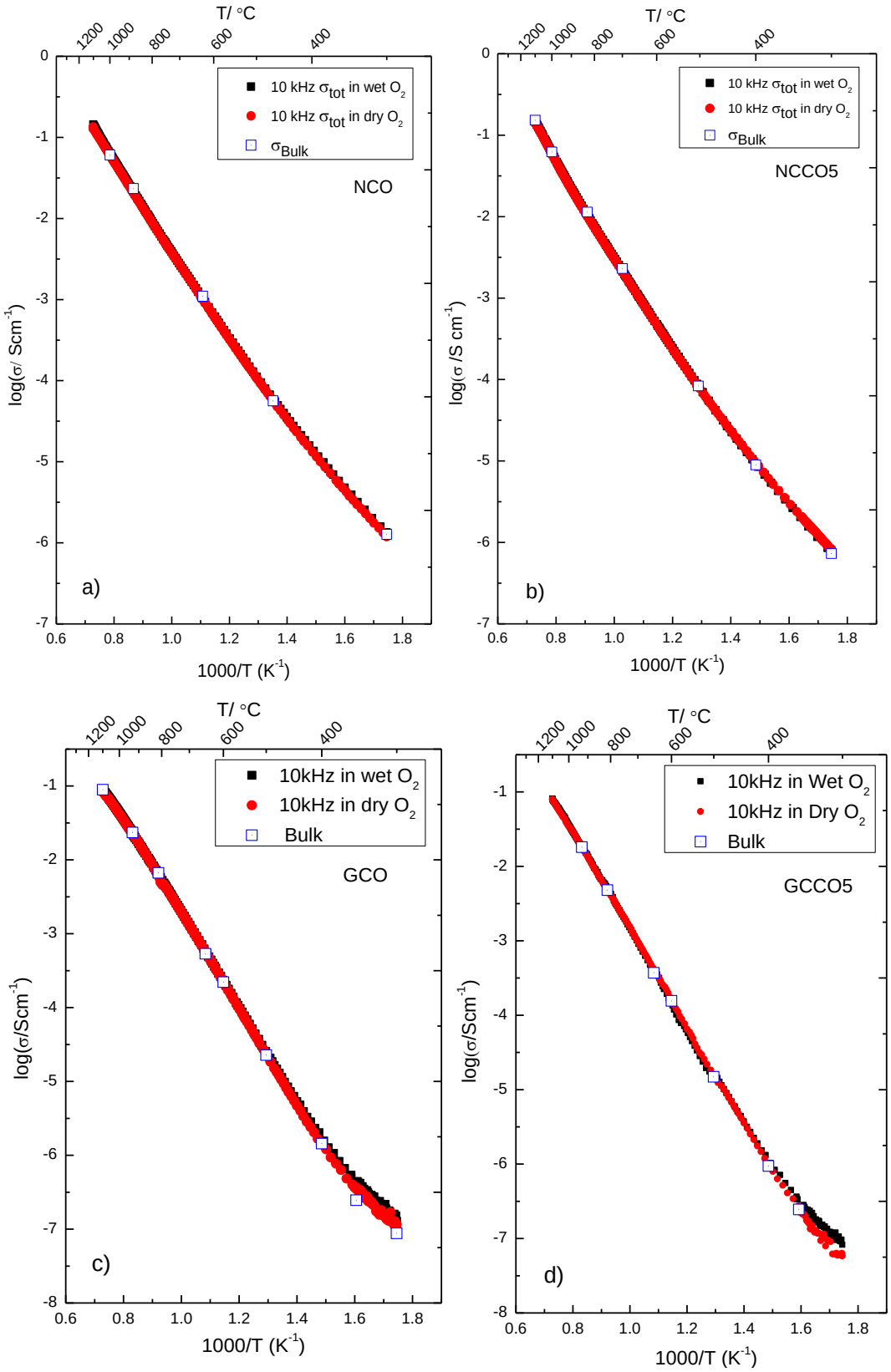

Figure 5.13 Logarithm of conductivity versus reciprocal of temperature of a) NCO b) NCCO5 c) GCO d) GCCO5.

5.2.3. pO_2 dependency of the conductivity

Figure 5.14 displays the logarithm of the conductivity (10 kHz) versus the logarithm of pO_2 of NCO, NCCO5, GCO and GCCO5 from 1100°C to 600°C in wet oxygen.

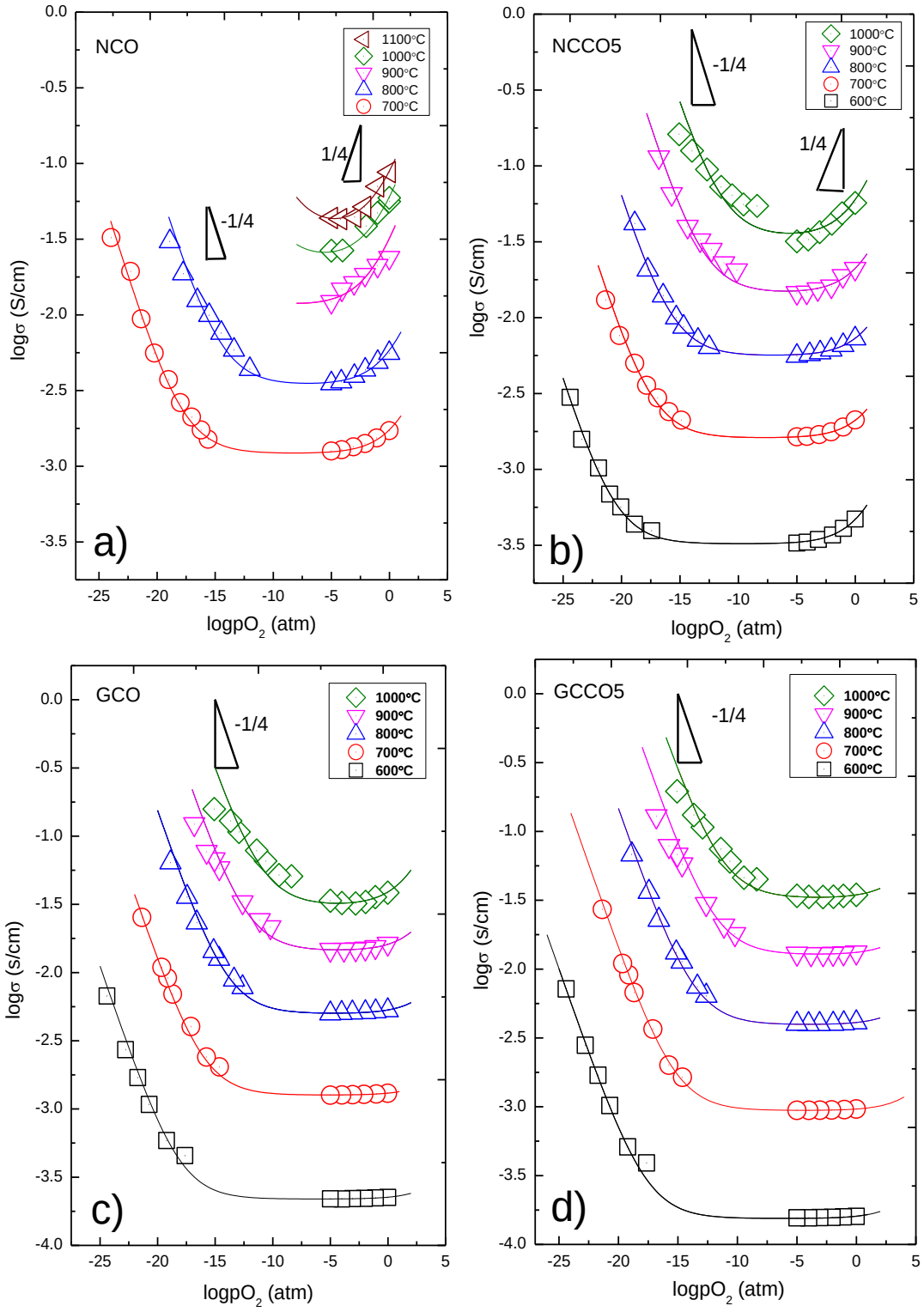

Figure 5.14 pO_2 dependencies of the conductivity and fitted results by the defect chemistry model a) NCO b) NCCO5 c) GCO d) GCCO5.

In reducing atmosphere, log conductivity of the four samples were inversely proportional to the logarithm pO_2 with a slope of around -1/4. This is in accordance with the slope demonstrated in the Brouwer diagram in section 2.2. For NCO and NCCO5, the conductivity increased with increasing pO_2 in oxidizing atmosphere with a slope approaching to 1/4 at high temperatures; the slope became smaller at lower temperatures. In the middle part of the graph, there was a plateau where the total conductivity was independent of the oxygen partial pressure, corresponding to the oxygen ion conductivity. On the other hand, the total conductivity of GCO and GCCO5 were independent of pO_2 below 800°C in oxidizing atmospheres. The conductivity data were fitted by to a chemistry model derived from the Brouwer diagram in Chapter 2. Derivations of this equation are summarized in Chapter 9.

$$\log\sigma_{\mathrm{tot}} = \log\left[\sigma_{O2-} + \mathrm{B}(\mathrm{pO_2})^{-\frac{1}{4}} + \mathrm{C}(\mathrm{pO_2})^{\frac{1}{4}} + \sigma_{\mathrm{H+}}\right] \qquad \textbf{Equation 5-2}$$

At high temperatures, proton conductivity is estimated to be minor compared with other charge carriers, so the proton conductivity can be neglected in the model. Based on the model, the isothermal electronic and oxygen ion conductivity can be obtained which can be used in the modeled results in 5.2.6.

5.2.4. pH_2O dependency

According to pO_2 dependency, GCO and GCCO5 are pure ionic conductor under oxidizing condition below 600°C. Therefore, pH_2O dependency of GCO and GCCO5 were measured at wet O_2. However, since NCO and NCCO5 are mixed p-type and ionic conductor under oxidizing condition, their pH_2O dependency were carried out in the Ar in order to reduce the relatively high p-type conductivity.

Figure 5.15 displays the a.c. conductivity of the samples as a function of pH_2O. As can be seen from the four graphs, the dependency becomes gradually weaker with increasing temperature. When the temperature is above 600°C, the conductivity measured in dry and wet atmospheres are almost the same, suggesting that the conductivity is independent of pH_2O. The pH_2O dependency at low temperatures indicates that the proton conduction becomes significant, but the slope was substantially smaller than ½. This can be explained by the relatively more predominating oxygen ion conductivity compared to the proton conductivity, resulting in a depression of the slope of the sum of the proton and oxygen ion conductivity.

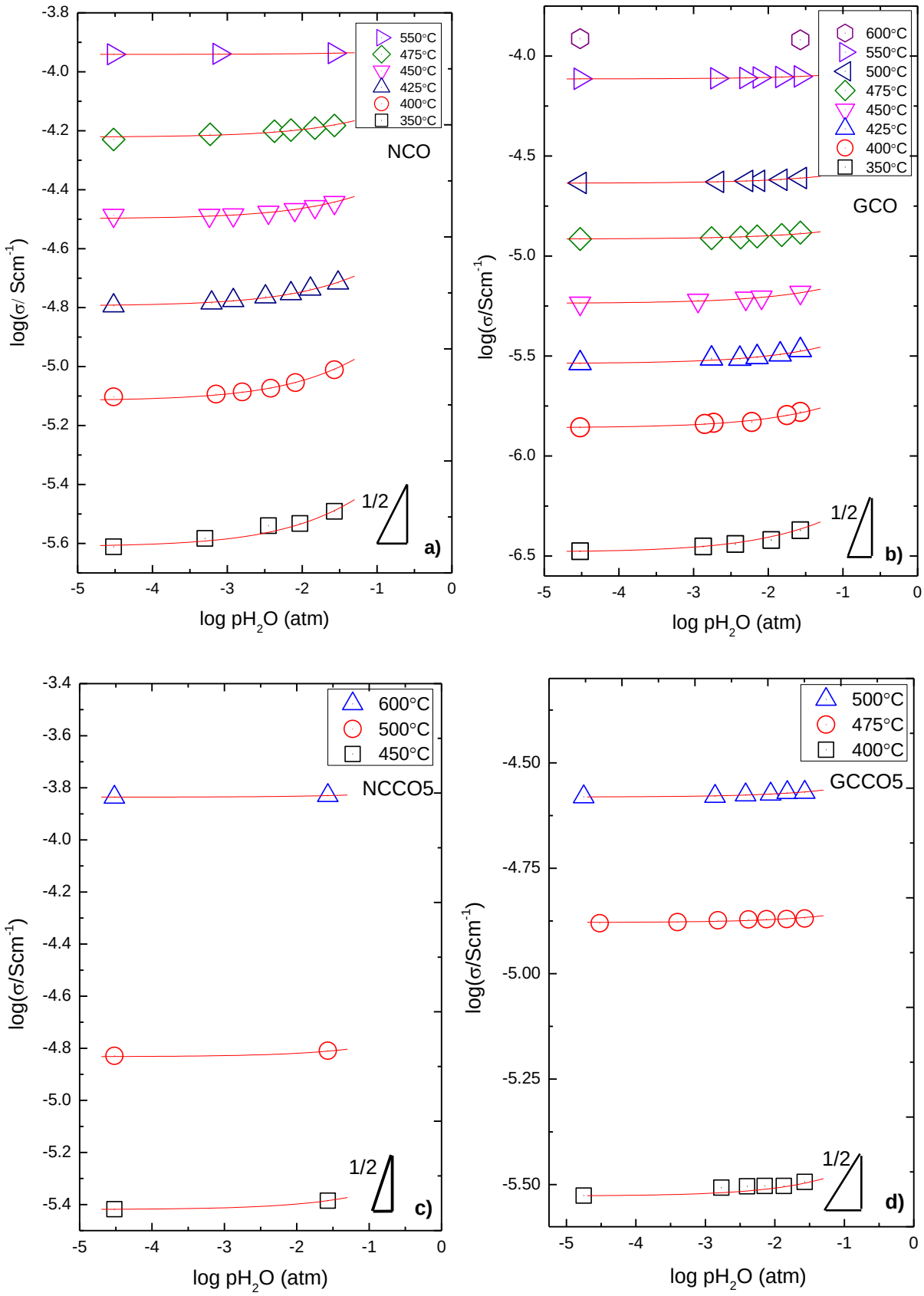

Figure 5.15 pH_2O dependency of the conductivity a) NCO b) GCO c) NCCO5 d) GCCO5.

The results in Figure 5.15 were fitted by a defect chemistry model as follow

$$\log\sigma_{tot} = \log\left[\sigma_{O2-} + \sigma_p + (7K_H)^{\frac{1}{2}}P_{H_2O}^{\frac{1}{2}}\right] \quad \textbf{Equation 5-3}$$

The proton conductivity at maximum humidity (pH_2O=0.027atm) and the H^+/D^+ isotope effect as a function of reciprocal temperature is plotted in Figure 5.16. The ratio between σ_{H2O} and σ_{D2O} increases gradually with decreasing temperature and the proton conductivity follows Arrhenius behavior. At same temperature, the proton conductivity and $\sigma_{D2O}/\sigma_{H2O}$ of NCO are higher than those of GCO.

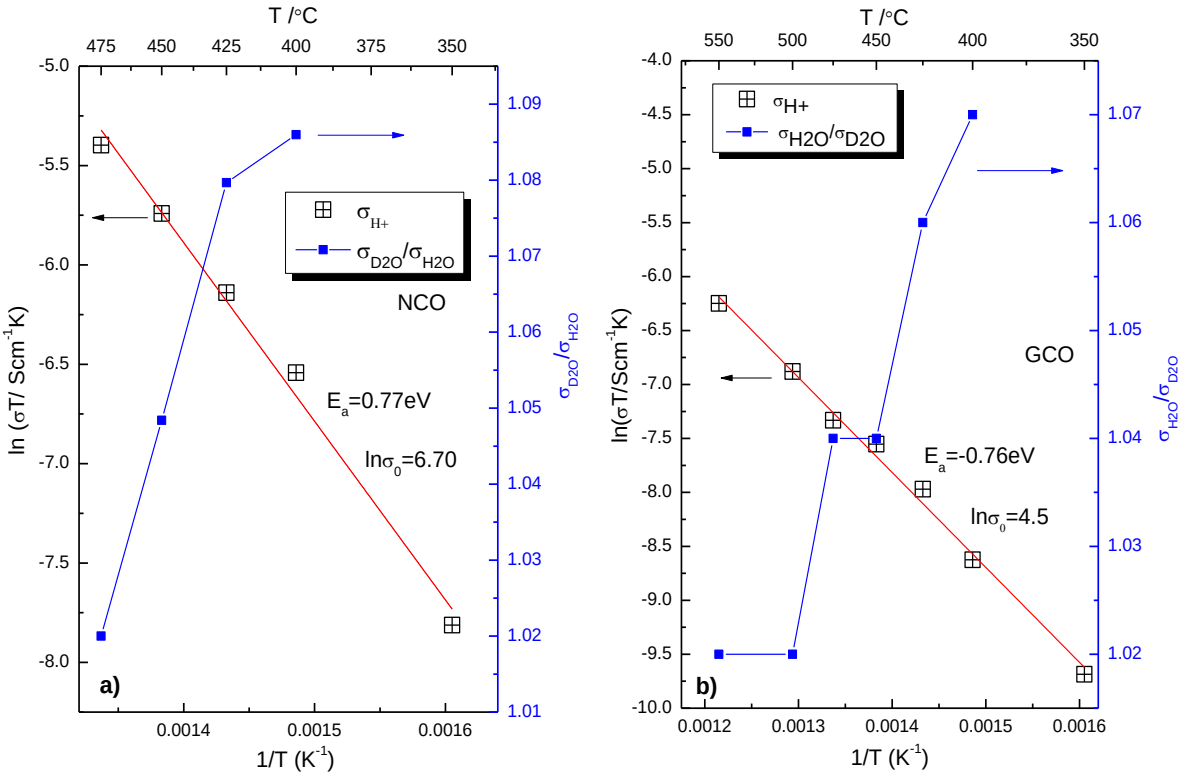

Figure 5.16 Modeled proton conductivity at pH_2O=0.027atm and H^+/D^+ isotope effect as a function of reciprocal temperature of (a) NCO (b) GCO.

5.2.5. Calculated transport number

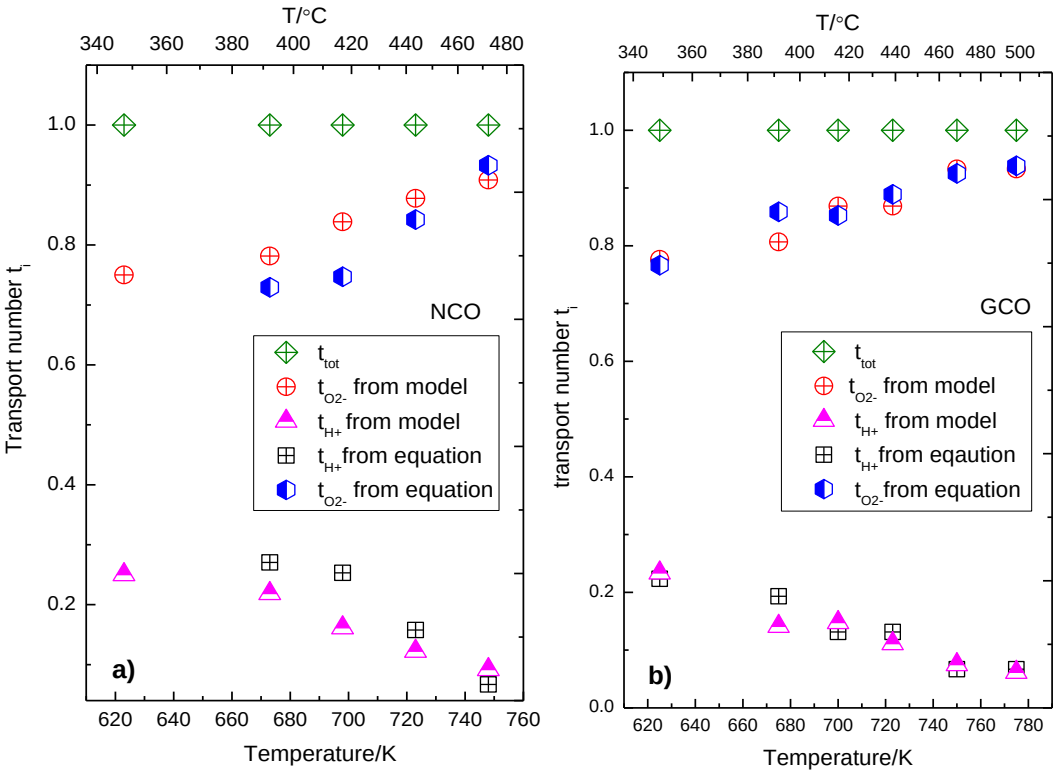

Figure 5.17 Calculated transport number of protons, oxygen ions and the value derived by the H^+/D^+ isotope (a) NCO (b) GCO.

Under wet oxidizing conditions, both oxygen ions and protons contribute to the total conductivity. Transport numbers of the charge carriers under fully wet condition were calculated based on the modeled results in Figure 5.17 by using the equation 5-4 as follow

$$t_{H+} = \frac{\sigma_{H+}}{\sigma_{tot}} \qquad \textbf{Equation 5-4}$$

On the other hand, the transport number of protons can be estimated by a formula as proposed by Bonanos [104] regarding the ratio $\alpha = \sigma_{H2O}/\sigma_{D2O}$ obtained in the isotope exchange measurement. Another parameter $\beta \equiv \sigma_{H+}/\sigma_{D+}$ is the ideal isotope effect which is estimated as the classical value of $\sqrt{2}$. The formula gives

$$t_{H+} = \frac{(1-\alpha)\beta}{(1-\beta)\alpha} \qquad \textbf{Equation 5-5}$$

From Figure 5.17, the transport numbers obtained by the formula is close to that calculated from the modeled results, revealing that the modeled results are acceptable. At the low temperature, protons and oxygen ion are the dominating charge carriers, but the oxygen ion conduction becomes predominating with increasing temperature.

5.2.6. Parameters for thermodynamics and transport

Figure 5.18 displays the modeled results of the samples and the parameters obtained by the model are summarized in Table 5.7.

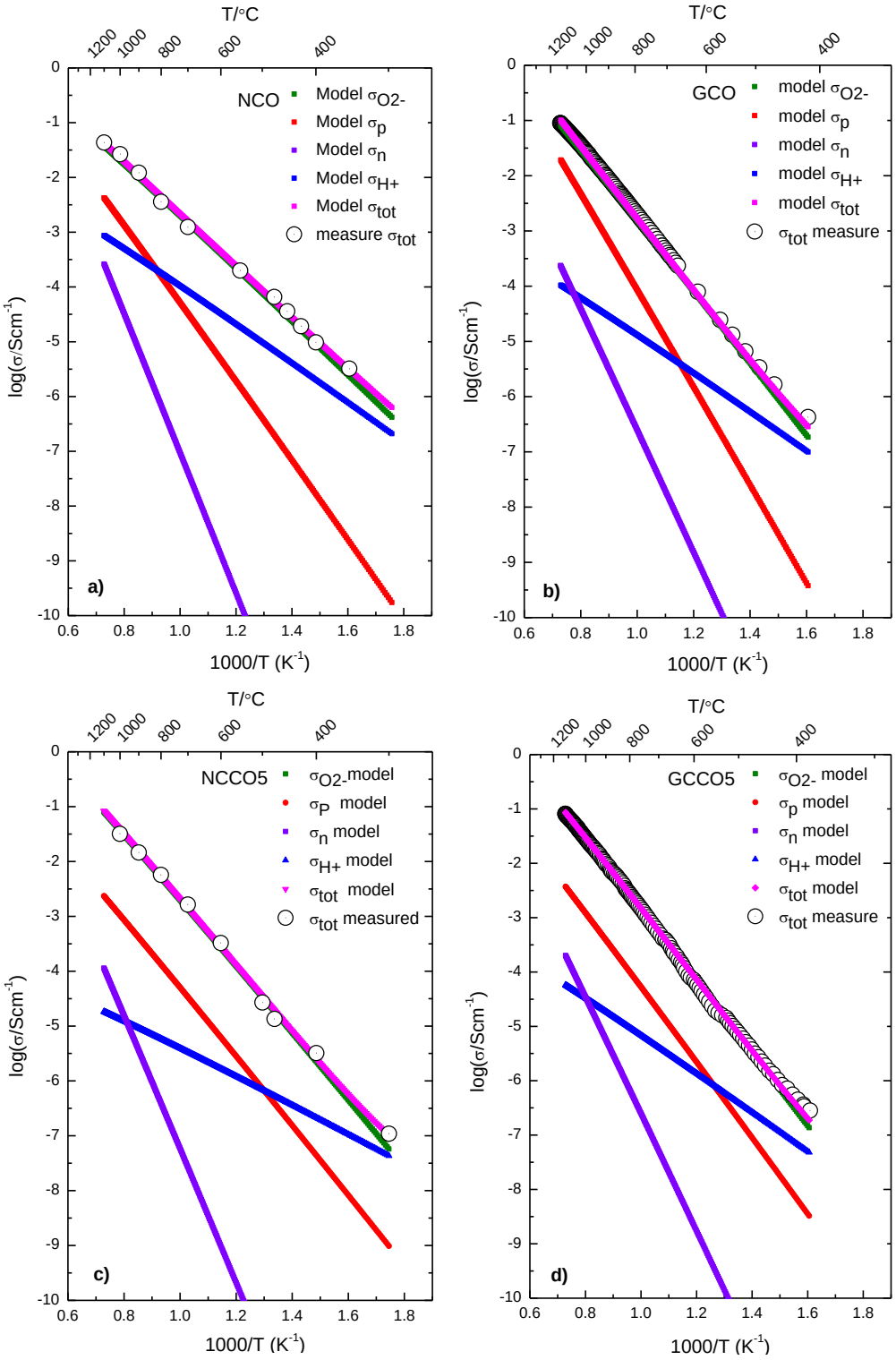

Figure 5.18 Open circles are bulk conductivity measured from 1100°C to 300°C in wet O_2 (pH_2O= 0.027atm), red lines are modeled electron hole conductivity, blue lines are proton conductivity, green lines are oxygen ion conductivity (a) NCO (b)GCO (c) NCCO5 (d) GCCO5

Three assumptions are made with respect to the model. Firstly, protons were assumed to be minor above 500°C. Secondly, the isothermal electronic conductivity and oxygen ion conductivity above 600°C are obtained by fitting the pO_2 dependency with equation 5-2. Below 600°C, assuming that electronic conductivity is minor, isothermal oxygen ion conductivity and proton conductivity under fully wet condition are obtained by fitting pH_2O dependency by equation 5-3. In sum, the isothermal electronic and ionic conductivity were linear fitted from 1100°C to 300°C.

Table 5.7 Thermodynamic and transport parameters extracted from the modeled results.

Sample	$1/2\ \Delta H_{Red} + \Delta H_{mob}$ [kJ·mol^{-1}]	$1/2\ \Delta H^{0}_{Hyd} + \Delta H_{m,H}$ [kJ·mol^{-1}]	$K_{ox}^{1/2}\mu_0\ T$ [kJ·mol^{-1}]	$1/2\ \Delta H_{ox} + \Delta H_{mob,p}$ [kJ·mol^{-1}]	$u_{0,O^{2-}}$ [cm^2·K·V^{-1}·s^{-1}]	$\Delta H_{m,O^{2-}}$ [kJ·mol^{-1}]
NCO	252 ± 1	74±5	939±50	147±5	1277±100	99±2
GCO	219 ± 1	73±5	3709±100	175±5	28418±1000	127±2
NCCO5	241 ± 1	57±5	110±20	127±5	22026±2000	123±2
GCCO5	214 ± 1	75±5	29±10	140±5	55227±2000	133±2

5.3. TG results

Figure 5.19a shows the background TG curve measured in dry O_2 and Figure 5.19b displays the isothermal mass change of NCO in dry O_2 from 1100°C to 300°C. TG data like Figure 5.19b are obtained by subtracting the background data from raw data.

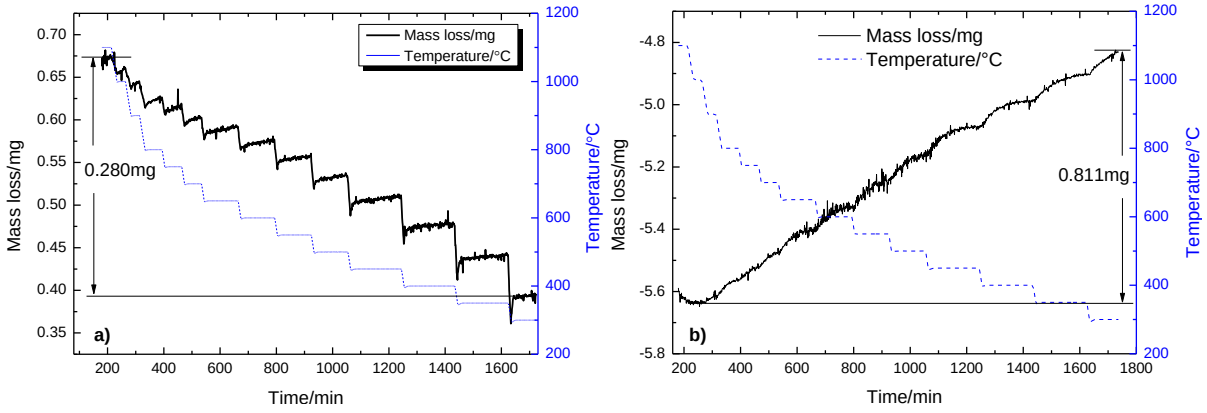

Figure 5.19 a) Background of NCO measured in dry O_2 from 1100°C to 300°C b) Thermogravimetric measurement of NCO in dry O_2 from 1100°C to 300°C.

In Figure 5.19b, the net mass increase is about 0.811mg, which is about three times the mass decrease of the background. According to the author's experience, the background data varies in different dates. Since the mass change of the sample is comparable to the mass change of the background, the results should be conservatively treated in this work.

Figure 5.20a and b present the relative mass change of NCO and GCO as a function of temperature from 1100°C to 300°C. The mass change of NCO and GCO under wet conditions is slightly higher than that under dry conditions. However, since the dry condition is not the ideal case, there is still a little water in the dry conditions that can be absorbed by the samples. Even though, no water is assumed to be absorbed under the dry conditions.

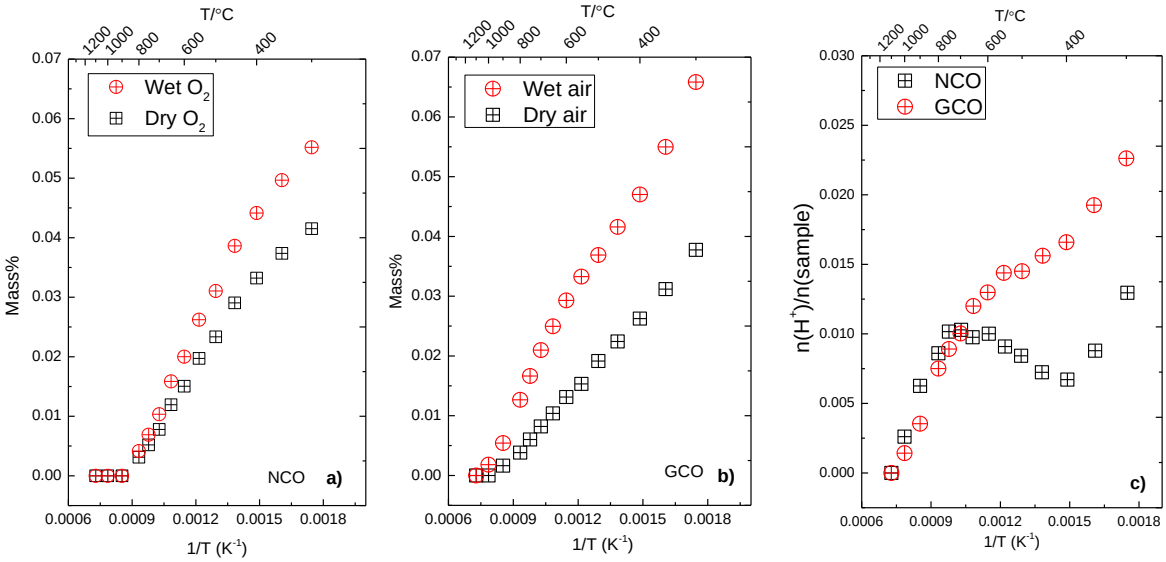

Figure 5.20 a) Percent of mass increase of NCO from 1000°C to 300°C in wet and dry O_2 b) Percent of mass increase of GCO from 1000°C to 300°C in wet and dry air c) molar concentration of NCO and GCO.

The net mass difference between wet and dry conditions should be attributed to water absorption. Figure 5.20c is the mole of proton per mole of sample as a function of inverse temperature. The absorbed water is assumed to hydrate oxygen vacancy to form protons, following the chemical equation 2-21.

Figure 5.21 displays the isothermal mass change in wet Ar, wet O_2 and dry O_2 at 550°C.The result is not corrected by the background data. From the results, mass firstly increase from wet Ar to wet O_2 (pO_2 increase), and then decreases from wet O_2 to dry O_2 (pH_2O decrease). Moreover, mass change from changing pO_2 is much larger than that from changing pH_2O.

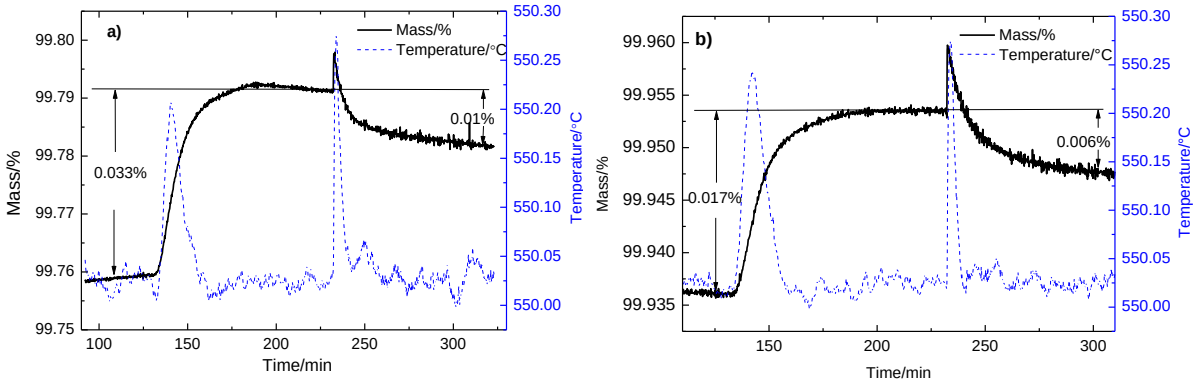

Figure 5.21 Mass change measured in wet Ar, wet O_2 and dry O_2 for (a) NCO (b) GCO.

Figure 5.22 displays the mass change during a hydrogen isotope exchange carried out at 400°C by swapping between H_2O-wetted and D_2O-wetted air/O_2.

Mass difference between H_2O-wetted and D_2O-wetted gas from the exchange between deuterons and protons is considered very small. It is worthwhile to note that the equilibrium constant of hydration is expected to be different in D_2O and H_2O, but is considered as negligible for this work.

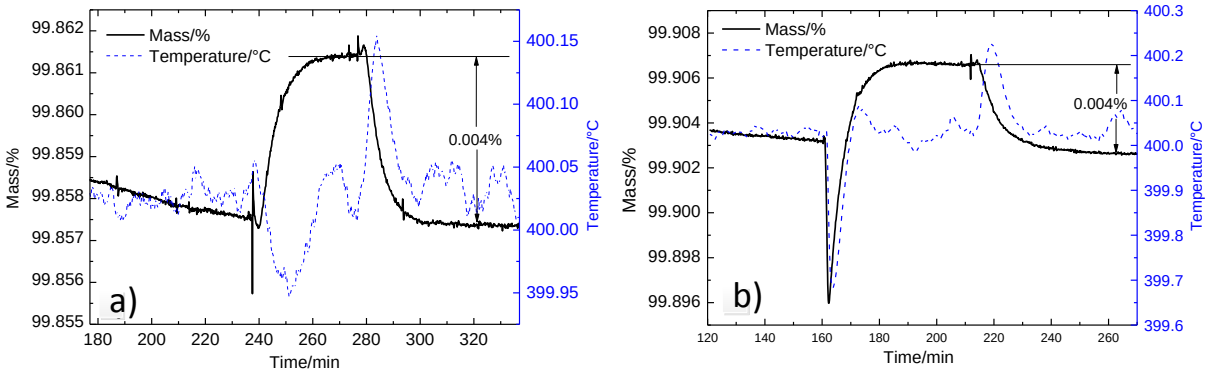

Figure 5.22 Mass change of swapping from D_2O-wetted to H_2O-wetted condition (a) NCO (b) GCO.

5.4. Electrical characterization at low temperatures

5.4.1. Temperature dependency from 450°C to 25°C

Figure 5.23 displays the a.c. conductivity as a function of inverse temperature of NCO (a), GCO (b) and GCCO5(c) measured in wet O_2 from 450°C to 25°C. In Figure 5.23a and b, some points between 200°C and 100°C miss because the corresponding conductivity of these points are too low to be measured by HP 4192.

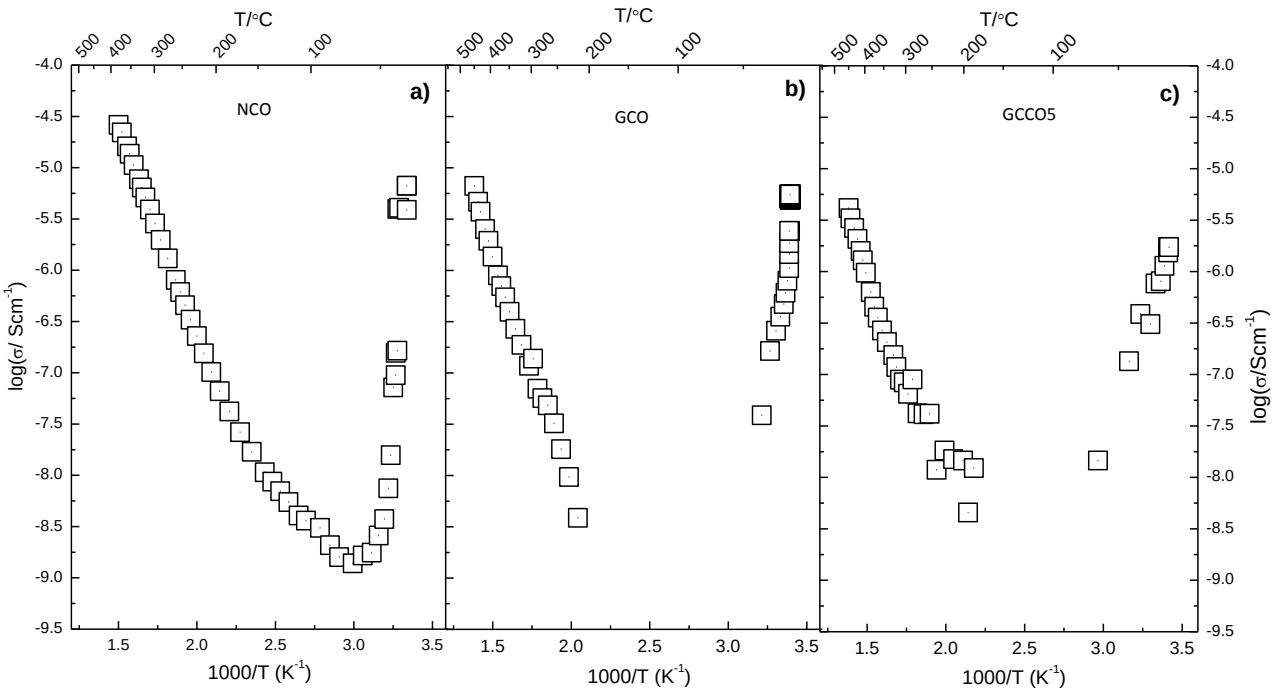

Figure 5.23 a) Logarithm conductivity vs. 1000/T from 450°C to 25°C a) NCO b) GCO c) GCCO5.

All the samples exhibited similar behavior that the electrical conductivity first decreases from 450°C to 100°C and then increases from 100°C to 25°C. In addition, the conductivity of GCO and NCO in room temperature was close to 1×10^{-5} Scm^{-1} that is almost equal to the total electrical conductivity in 450°C. However, the electrical enhancement behavior cannot be detected under dry conditions. This phenomenon will be discussed in the Chapter 6.

Figure 5.24 presents selected impedance spectra from GCO and NCO measured under wet oxygen (0.027atm) at room temperature with frequency from 1MHz to 5Hz. The data were fitted by an equivalent circuit (RQ), as summarized in Table 5.8. The specific capacitance of the semicircle is in the range of $pFcm^{-1}$. The relative static permittivity ε_r of NCO and GCO at 25°C is much higher than those above 300°C.

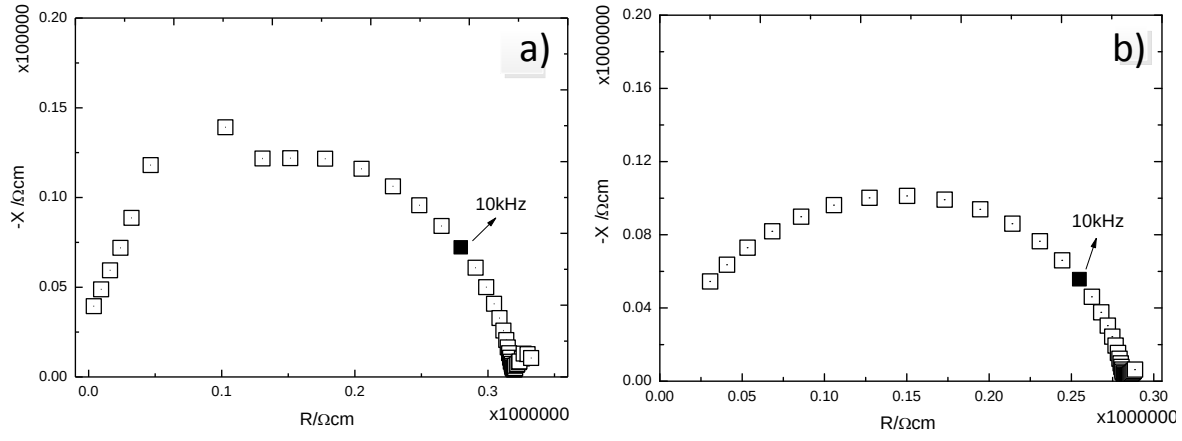

Figure 5.24 Impedance spectra of GCO (a) and NCO (b) recorded at room temperature.

Table 5.8 Results of deconvolution of impedance spectra in Figure 5.24.

T/°C	Condition	Sample	ρ1/kΩ cm	n_1	C1/pFcm^{-1}	ε_r
25	Wet O_2	NCO	2.89×10^5	0.82	8.0	90
25	Wet O_2	GCO	3.22×10^5	0.77	9.0	102

5.4.2. Characterization of surface charge conduction

Figure 5.25 shows the a.c. conductivity measured when the guard electrode is switched off and switched on. Results show the conductivity increases immediately when the guard electrode is turned off and decreases back when the guard electrode is turned on. Surface charge exhibited from the surface charge can be a possible reason for the conductivity increase when the guard electrode is off. The surface charge will be shielded when the guard electrode is turned on.

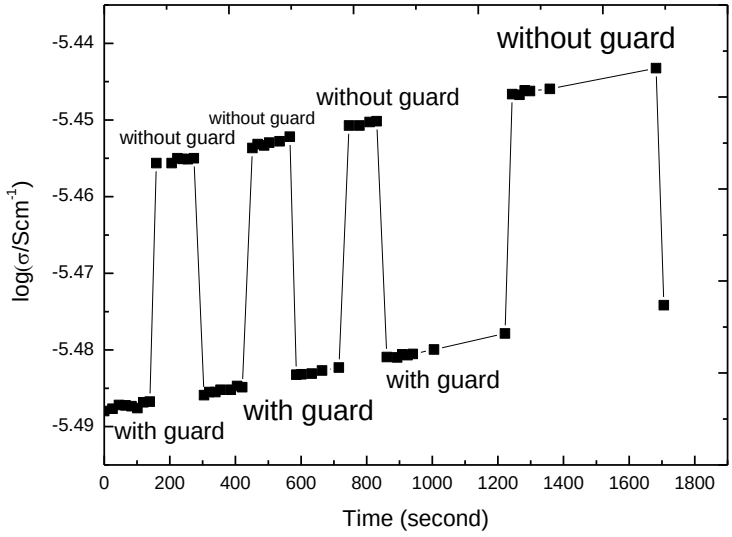

Figure 5.25 Difference of conductivity with and without the guard electrode.

5.4.3. pH_2O dependency

Figure 5.26 displays the a.c. conductivity (10 kHz) versus pH_2O at 25°C and 30°C, respectively. Slopes obtained from the linear fit of selected points at 25°C and 30°C are 2.72 and 2.8, respectively. It is worth noting that the conductivity in minimum pH_2O at 25°C was 10^{-10}Scm^{-1}, which is rather uncertain because it is close to the limitation of the instrument. Similarly, the conductivity under dry condition at 30°C is too low to be measured. The fairly high slope at 25°C and 30°C in wet O_2 presents that the electrical conductivity is strongly dependent of pH_2O.

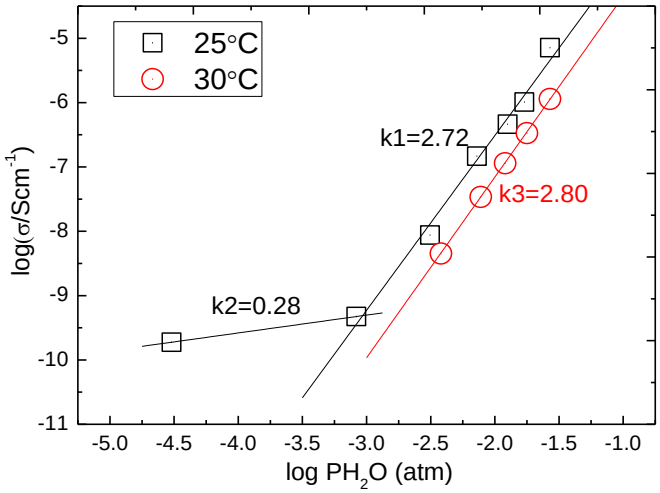

Figure 5.26 pH_2O dependency of GCO at 25°C and 30°C with linear fit.

5.4.4. Isotope effect

Figure 5.27a represents the a.c. conductivity (10 kHz) measured by swapping from H_2O-wetted O_2 to D_2O-wetted O_2 .Figure 5.27b displays the impedance spectra recorded in the corresponding equilibrium state in Figure 5.27a. The conductivity increases a little changing from H_2O-wetted to D_2O-wetted O_2. Impedance spectra are deconvoluted by the equivalent circuit (RQ) whose specific capacitance is around 8.2pFcm^{-1}. Also, the relative permittivity of the bulk conduction is around 92.

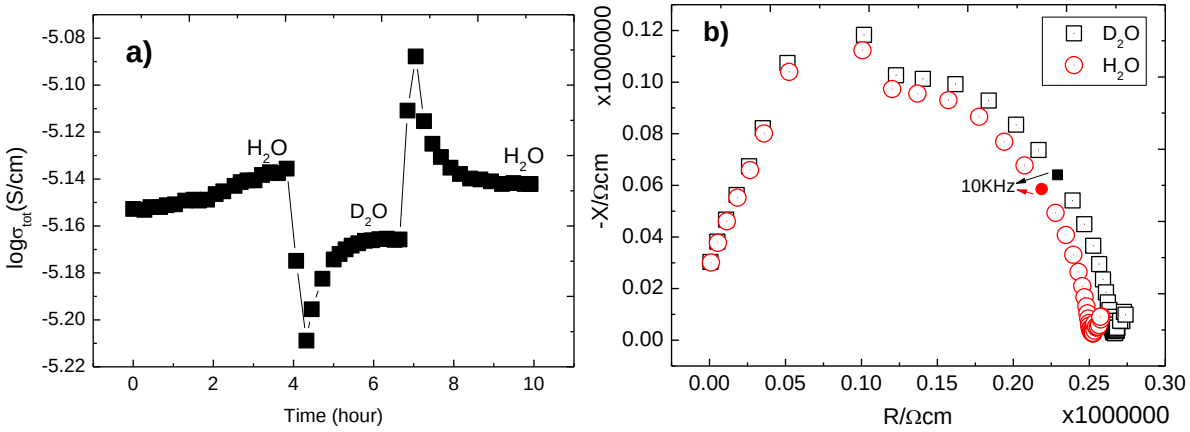

Figure 5.27 a) Conductivity in wetted D_2O and wetted H_2O oxygen b) impedance spectra recorded in wetted-D_2O and wetted H_2O in a).

Table 5.9 Results of deconvolution of impedance spectra in Figure 5.27b.

T/°C	Condition	Sample	ρ1/kΩ cm	n_1	C1/pFcm^{-1}	ε_r
25	Wet O_2	GCO	2.54×10^5	0.81	8.2	92
25	D_2O O_2	GCO	2.69×10^5	0.81	8.2	92

5.4.5. Thermogravimetry

Figure 5.28 displays the thermogravimetry of GCO measured in wet air from 100°C to 25°C. The mass increase below 100°C reflects the amount of the chemisorbed and physical absorbed water in the sample. The mass increased with decreasing temperature and the maximum water absorption happened at room temperature. The process indicates the hydration below 100°C is an exothermic reaction.

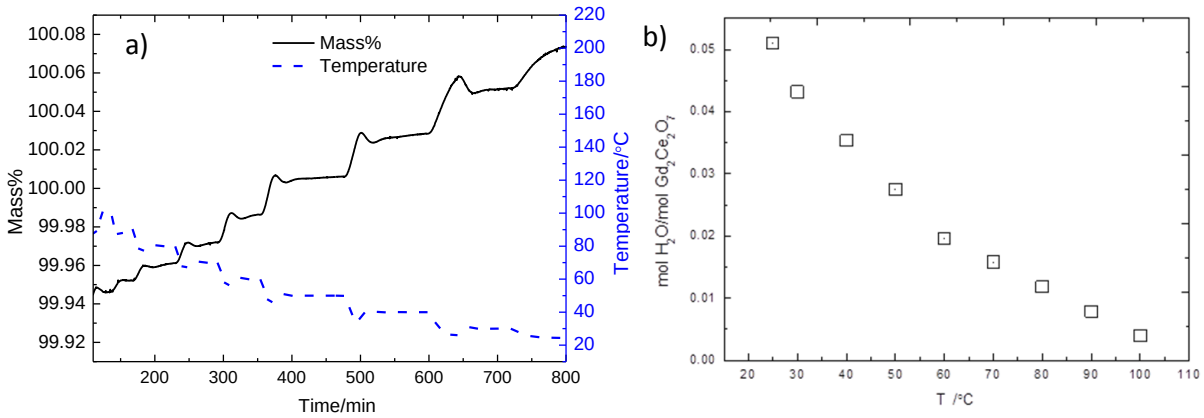

Figure 5.28 a) Thermogravimetry from 100°C to room temperature b) mole of water per mole of GCO as a function of temperature.

5.4.6. Electrical characterization below freezing point

Figure 5.29 presents the a.c. conductivity (10 kHz) of GCO versus inverse temperature in H_2O-wetted and D_2O-wetted oxygen.

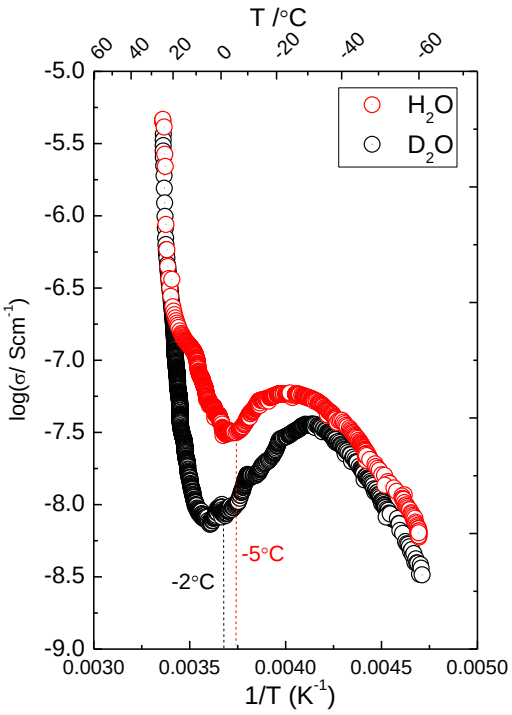

Figure 5.29 Electrical conductivity of GCO as a function of reciprocal temperature in H_2O-wetted and D_2O-wetted O_2 from room temperature to -60°C.

Electrical measurements were carried out in a closed cell filled with H_2O- wetted and D_2O-wetted oxygen from 25°C to -60°C at the cooling rate of 3°C per hour. Results were recorded by the impedance spectrometer Solartron 1260. As can be seen from Figure 5.30, impedance spectra measured in H_2O and D_2O atmospheres at freezing point were recorded.

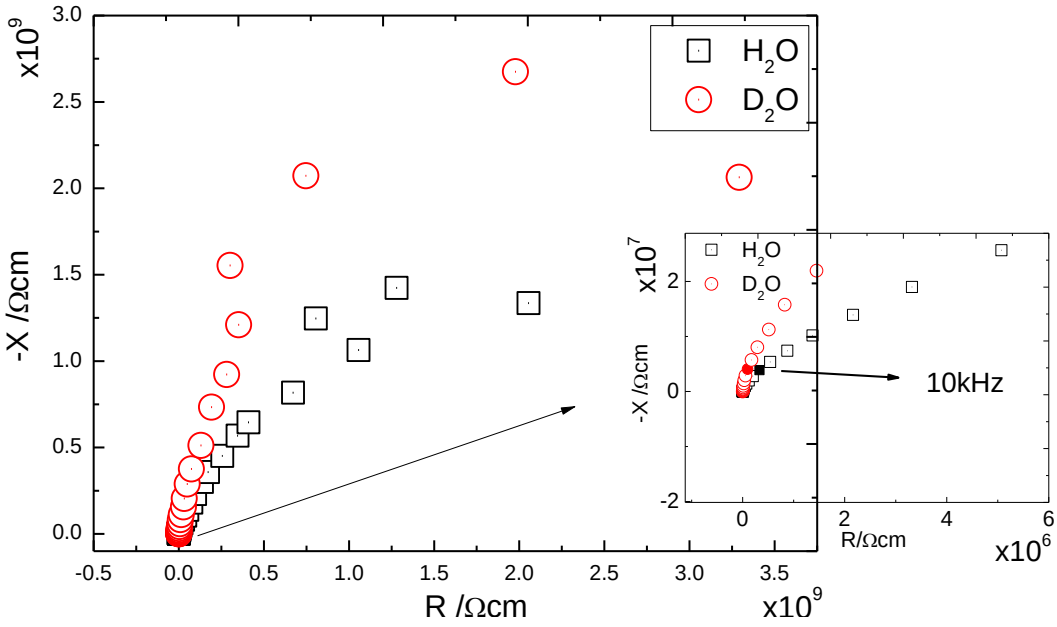

Figure 5.30 Impedance spectra of GCO recorded in H_2O-wetted and D_2O wetted oxygen at 0°C.

An equivalent circuit (R_1Q_1) was used to fit the impedance spectra. In Table 5.10, results from the deconvolution were summarized. From the results, the capacitance is in the range of $pFcm^{-1}$ and the relative static permittivity in H_2O-wetted O_2 is relatively higher than that in D_2O-wetted O_2.

Table 5.10 Results of deconvolution of given impedance spectra in Figure 5.30.

T/°C	Condition	ρ1/kΩ cm	n_1	C1/$pFcm^{-1}$	ε_r
0	O_2 with H_2O	1.71×10^6	0.89	7.7	87
0	O_2 with D_2O	4.10×10^6	0.99	4.0	45

6. Discussion

In this section, results of the electrical measurements, TG and XRD Rietveld refinement will be discussed to address the defects and diffusion in the NCO and GCO materials at a wide range of temperatures. In addition, several results are selected from publications to compare with the results in this work. Finally, two valid models are presented to explain electrical behaviors at low temperatures.

6.1. Crystal structures and defects in NCO and GCO

The XRD results show that NCO and NCCO5 crystallize in the disordered fluorite structure and XRD Rietveld results confirm that the oxygen sublattice in NCO and NCCO5 are partially occupied by oxygen ions. Thus, defects in NCO and NCCO5 can be appropriately described by the compatible Kröger-Vink nomenclature introduced in section 2.1.3. Furthermore, the XRD pattern at room temperature and Rietveld refinement demonstrate that GCO crystallizes in a C-type structure with ordered oxygen ions. Minervini's atomistic computer calculation [48] reveals that the anion Frenkel formation energy between 48f and 8a is so low for GCO that these sites tend to disorder. Also, Bjørheim's DFT calculation [105] demonstrates the anion Frenkel formation energy of 48f-8a migration and 8b-8a migration are almost the same negative value suggesting that the oxygen sites in GCO are disordered. GCO exhibited reversible phase transition from F-type to C-type phase between 1200°C and room temperature [10]. Since the logarithm electrical conductivity decreases linearly with decreasing temperature from 1100°C to 300°C (cf. Figure 5.13), thereby, the transition is estimated to happen below 300°C. Hence, oxygen ions in GCO are assumed to be disordered above 300°C. It is thus valid to use the compatible KV-notation to describe the defects in NCO and GCO. Another two approaches, which is used to express the defects in pyrochlore and doped oxides, are not precise to describe the defects in disordered fluorite.

One approach is to consider inherent partial occupied oxygen sites as an anion Frenkel reaction with a high equilibrium constant, i.e. the oxygen ion can easily jump to the structurally vacant interstitial sites. This approach is appropriate for pyrochlore related materials with an ordered oxygen sublattice e.g. $La_2Zr_2O_7$. The electronuetrality follows the relationship $[V_O^{2\bullet}] = [O_i^{2/}]$. However, such an approach is not appropriate to describe the intrinsic defects in $Ln_2Ce_2O_7$ system. First of all, for the $Ln_2Ce_2O_7$ with fairly close size of cations, the cations and anions will disorder in the sublattice at higher temperatures meaning that the phase exhibits an order-disorder phase transformation with increasing temperature, e.g. GCO. Therefore, it is neither necessary nor appropriate to describe order-disorder phase transition in terms of anion Frenkel reaction.

The alternative approach is to consider $Ln_2Ce_2O_7$ as 50% Ln^{3+} doped into CeO_2. The electronuetrality reads $2[V_O^{2\bullet}] = [Ln_{Ce}^{/}]$ =constant. However, this consideration also introduces some problems. Firstly, the electroneutrality is not always true in such heavy acceptor doped samples because the negatively charged acceptor dopant will inevitable associate with oxygen vacancies, thereby, forming clusters $[Ln_{Ce}^{/}V_O^{2\bullet}Ln_{Ce}^{/}]^X$ or $[Ln_{Ce}^{/}V_O^{2\bullet}]^{\bullet}$. If the temperature of cluster dissociation is higher than the maximum measured temperature, the oxygen vacancies in the clusters are trapped and cannot move freely. In that case, one cannot obtain the correct electroneutrality. On the other hand, one should mention that this approach just consider about totally disordered cations. It cannot reflect the situation of disordered anions by just using $V_O^{2\bullet}$. Due to such analysis, it is also not precise to believe $Ln_2Ce_2O_7$ as ceria is 50% substituted with an acceptor.

In sum, it is fairly appropriate to describe the defects in these samples by using the compatible KV- notation and the following discussion will be emphasized on this special defect notation.

6.2. NCO, GCO, NCCO5 and GCCO5- Conductivity and TG

The electrical conductivity of NCO and GCO presents similar features with respect to the influence of the charge carriers as a function of and under various measuring conditions. As can be seen from modeled results (cf. Figure 5.18), the total electrical conductivity of the materials is dominated by oxygen ion conductivity and proton conductivity below 500°C. Moreover, they exhibit p- type electronic conduction in oxidizing and n- type electronic conduction in reducing atmospheres at high temperatures. The presented pO_2 dependency, pH_2O dependency of the bulk properties and the modeled results can be explained by the full electrical neutrality condition

$$\frac{3}{4}\left[OH_{\frac{7}{8}O}^{\frac{3}{4}\bullet}\right] + \frac{7}{4}\left[V_{\frac{7}{8}O}^{\frac{7}{4}\bullet}\right] + p = \frac{1}{4}\left[O_{\frac{7}{8}O}^{\frac{1}{4}/}\right] + [Acc^{/}] + n \qquad \textbf{Equation 6-1}$$

where $[Acc^{/}] = 0$ for NCO and GCO.

6.2.1. Electronic conductivity

From 600°C to 1100°C, the conductivity of all materials approaches $pO_2^{-\frac{1}{4}}$ dependency under reducing conditions (cf. Figure 5.14), corresponding to the left part of region 3 in the Brouwer diagram (cf. Figure 2.1)

$$\frac{7}{4}\left[V_{\frac{7}{8}O}^{\frac{7}{4}\bullet}\right] = \frac{1}{4}\left[O_{\frac{7}{8}O}^{\frac{1}{4}/}\right] + n \qquad \textbf{Equation 6-2}$$

The predominating electronic conductivity is mainly resulting from the high mobility of the electronic species. Furthmore, the n-type conduction in these materials can be a result of reduction Ce^{4+} to be Ce^{3+} under reducing conditions [106] at high temperature. Hence, $Ln_2Ce_2O_7$ will be non-stoichiometric under reducing conditions. The defect reaction is described in equation 2-10. It is worth noting that the pO_2 dependency seems to deviate from the modeled line at 1100°C with a weaker slope than expected. One possible explanation is that the dominating electroneutrality changes to a situation corresponding to region 2, $\frac{7}{4}\left[V_{\frac{7}{8}O}^{\frac{7}{4}\bullet}\right] = n$, in the Brouwer diagram (cf. Figure 2.1) with decreasing pO_2. However, such transition may happen in the fairly low pO_2. On the other hand, at high temperatures, the resistance of the sample can be comparable to the resistance of electrodes. In that case, the total conductivity will be seriously affected by electrodes.

The conductivity of NCO and NCCO5 exhibit a strong pO_2 dependency under oxidizing conditions while GCO and GCCO5 show a relatively weaker pO_2 dependency at high temperatures (cf. Figure 5.14). The pO_2 dependency indicates mixed p-type and oxygen ion conductions in these materials. Under dry oxidizing conditions, electron holes form on the expense of oxygen vacancies electron, as described in equation 2-14. The negatively charged oxygen sites will be fully compensated by the positively charged oxygen vacancies and electron holes, which correspond to right part of region 3 in Brouwer diagram (cf. Figure 2.1). The electroneutrality is then given as

$$\frac{7}{4}\left[V_{\frac{7}{8}O}^{\frac{7}{4}\bullet}\right] + p = \frac{1}{4}\left[O_{\frac{7}{8}O}^{\frac{1}{4}\prime}\right] \qquad \textbf{Equation 6-3}$$

Furthermore, this result is in good agreement with the TG results (cf. Figure 5.20a and b) where the isothermal mass increase under dry oxidizing conditions can be ascribed to oxygen vacancies oxidation. The mass increase from Ar to dry O_2 (cf. Figure 5.21) can further confirm oxidation reaction.

According to Figure 5.21, the site fraction of oxygen vacancy being oxidized is calculated to be 1.8×10^{-3} for NCO and 1×10^{-3} for GCO, which is far less than 0.125, the expected site fraction of oxygen vacancies. This means that the concentration of oxidized oxygen vacancies is far lower than that of intrinsic oxygen vacancies that the oxidization can be further confirmed to be in the region 3 from the Brouwer diagram (cf. Figure 2.1) as expected. Also, higher mass increase in NCO suggests more oxygen vacancies are oxidized in NCO, thereby, higher concentration of electron hole in NCO. This estimation is in agreement with the relative high pO_2 dependency of NCO and the higher modeled p-type conductivity (cf. Figure 5.14a) of NCO above 600°C. In $Ln_2Ce_2O_7$ (Ln=Lanthanide), $Nd_2Ce_2O_7$ exhibits

considerably high p-type conductivity under oxidizing conditions [36]. Similarly, the relatively high p-type conductivity was also found in Nd_6WO_{12} from Ln_6WO_{12} (Ln=La, Nd, Gd, Er) family [76]. The band gap of NCO is expected to be lower than GCO because NCO is green and GCO is white. Therefore, it is no surprise for NCO to show higher p-type conductivity due to the narrower band gap.

As can be seen in Table 5.7, activation energy of n- type ($1/2\Delta H_{red}+H_{m,n}$), p-type ($1/2\Delta H_{ox}+H_{m,p}$) conductivity decrease when NCO and GCO is acceptor doped. The concentration of electrons and electron holes follow

$$np = \exp\left(-\frac{\Delta E_g}{RT}\right) = K'_{o,i}\exp\left(-\frac{\Delta H_g}{RT}\right) \qquad \textbf{Equation 6-4}$$

where ΔE_g is the band gap, ΔH_g denotes enthalpy of ionization and $K'_{o,i}$ represents the equilibrium constant. Furthermore, ΔH_g can be determined by combining equation 2-13, 2-16 and 6-4, as can be written as follow

$$\Delta H_g = \frac{1}{2}(\Delta H_{red} + \Delta H_{ox}) \qquad \textbf{Equation 6-5}$$

As we know, band gap of oxides will decrease when doped by a much lighter cation. So it is plausible that band gaps of NCO and GCO decrease when doped by calcium. Hence, ΔH_g decreases in the doped samples. Based on equation 6-5, the decreasing sum of $1/2\Delta H_{red}+H_{m,n}$ and $1/2\Delta H_{ox}+H_{m,p}$ may be a result of the decreasing band gap in the calcium doped NCO and GCO.

6.2.2. Ionic conductivity

Oxygen ion conductivity

At intermediate pO_2, the conductivity is essentially independent of pO_2 which may reflect that the total conductivity is predominated by ionic charge carriers. The oxygen ion conductivity of NCO and GCO was curve fitted to a model based on total conductivity composed of a pO_2 and pH_2O dependent contribution, respectively (cf. Fig. 5.18a and b). It was shown that oxygen ion conductivity is predominating from high to low temperature. The relatively high oxygen ion conductivity in GCO and NCO can be a result of the high concentration of intrinsic oxygen vacancies and high oxygen vacancy mobility.
In addition, enthalpy of oxygen ion mobility for NCO is lower than those of GCO. The results indicate that oxide ions in NCO has more favorable path than GCO.

If one compares the conductivity characteristics of undoped and acceptor doped NCO and GCO, e.g. as in the temperature dependency (cf. Figure 5.13) and pO_2 dependency (cf. Figure

5.14) of the conductivity, there are no significant changes , indicating only minor effects of the doping in both materials. For acceptor dopants, the negative charged dopant will modify the electroneutrality and more oxygen vacancies will form to compensate the dopants, as shown in equation 2-18. However, one should note that the concentration of oxygen ion and oxygen vacancy is far greater than the dopants. Small doping concentration like 5% will not change the concentration of oxygen vacancies too much (1.05mol oxygen vacancies/1mol $Ln_{1.95}Ca_{0.05}Ce_2O_{7-\delta}$ vs. 1mol oxygen vacancies/1mol $Ln_2Ce_2O_7$).

Another possible reason for the insignificant effect of doping can be that the acceptor is charge compensation by internal antitsite defects between the disordered cations rather than with formation of oxygen vacancies [60] e.g.

$$2MlO + 3Ln_2Ce_2O_7 = 2Ml'_{Ln} + 2Ce^{\bullet}_{Ln} + 4Ce^{X}_{Ce} + 14O^{X}_{O} + 3Ln_2O_3 + 2V^{X}_{Ln_{Ln}} + 2V^{X}_{Ce_{Ce}} + 7V^{X}_{O_O} \quad \textbf{Equation 6-6}$$

The acceptor dopant will then be charge compensated by the cation antitsite donor dopant accompanied by forming the phase rich in Ln_2O_3. Indeed, from SEM-EDS on GCO, the concentration of Gd was found to be higher than the expected stoichiometry in some grains of GCO while no such grains were found in NCO. Hence, this result implies the cation disorder may be valid for the insignificant effect of doping.

From Table 5.7, $\Delta H_{m,O2-}$ of NCCO5 is much higher than that of NCO and GCCO5 also exhibits slight increase compared with GCO as well. Also, the pre-exponential constants also increase upon doping. The main reason for the effect of doping between the doped sample and undoped sample can be due to defects association between the acceptor dopant and the oxygen vacancies. This has been reported for many doped ceria containing materials, such as $Ce_{1-x}Nd_xO_{2-x/2}$, $Ce_{1-x}Gd_xO_{2-x/2}$ and $Ce_{1-x}Y_xO_{2-x/2}$ where the activation energy for oxygen ion conductivity increases with increasing amount of dopant [107-109]. The acceptor dopants in NCCO5 and GCCO5, Ca'_{Ln} may eventually associate with the oxygen vacancies and thus the activation energy can be considered as the sum of the enthalpy of the oxygen ion mobility $\Delta H_{m,o^{2-}}$ and the association enthalpy ΔH_a. The expression for the defect association model should be

$$\sigma = \frac{\sigma_0}{T}\exp\left(-\frac{\Delta H_{m,o^{2-}} + \Delta H_a}{kT}\right) \quad \textbf{Equation 6-7}$$

where $\Delta H_{m,o^{2-}}$ is independent of temperature and doping concentration. With the temperature increasing, the force between the associated defects becomes weak so that increases the likelihood of breaking up the complex. If such, the pre-exponential will be rather uncertain because the slope will become lower with increasing temperature and the

real pre-exponential constants will tend to smaller compared with the modeled ones. Although Ca is expected to substitute Nd sites, some Ca may also substitute Ce in NCO because of the total disordered cations. Such double charged dopant $Ca_{Ce}^{//}$ tends to seriously associate with oxygen vacancy due to the high coulombic force. Such might be the explanation for the higher increase of oxygen ion mobility in NCCO5.

Protonic conductivity

As shown in Figure 5.15, electrical conductivity is independent of the pH_2O above 550°C meaning that proton conductivity is minor, which can be further confirmed by the minor proton transport number (cf. Figure 5.17) above 475°C. However, pH_2O dependency becomes stronger with decreasing temperature, but far lower than $pH_2O^{\frac{1}{2}}$, which corresponds to the Brouwer diagram (cf. Figure 2.3). The increasing dependency is in agreement with the increasing water absorption according to the TG measurement (cf. Figure5.20c). The H/D isotope effects below 500°C (cf. Figure 5.16) indicates the protonic conduction, which can be further confirmed by the TG isotopic shift at 400°C (cf. Figure 5.22). One should note that the mass change is too small for a quantitative determination of proton concentration. Also, the estimated transport number of protons in NCO and GCO is about 0.2 at 350°C, indicating that proton conductivity is significant at 350°C.

In addition, the pH_2O dependency at 350°C indicates that NCO and GCO are not fully hydrated, which is in agreement with the TG measurements (cf. Figure 5.20c). As shown in equation 2-27, 8 oxygen sites are randomly occupied by 6 oxygen ions and 2 hydroxide ions when the sample is fully hydrated. Thus, the maximum site fraction of the protons is 0.25. The site fractions of protons in NCO and GCO are 0.0016 and 0.0028 at 300°C according to the TG results (cf. Figure 5.20c). Based on this calculation, the amount of water absorbed at 300°C is far away from the level of fully hydration. In other words, the materials start to dehydrate below 300°C. Based on these results, the hydration enthalpy should be fairly low in NCO and GCO.

These results confirm undoped NCO and GCO can be hydrated and exhibit proton conduction. This means that there is a distinct difference between the material of the present investigation and nominally undoped $La_2Zr_2O_7$, which exhibits only minor proton conductivity in wet atmosphere. The reason for the different functional characteristics between the material classes originates in the structural difference. The disordered oxygen sublattice NCO and GCO will promote the presence of intrinsic oxygen vacancies which are likely to be hydrated, whereas $La_2Zr_2O_7$ cannot accommodate any appreciable amount of

protons because there are so few intrinsic oxygen vacancies available to be hydrated due to the fully ordered oxygen sublattice.

6.3. Ionic conduction in pyrochlore related compounds

Oxygen ion conduction

Figure 6.1a presents the oxygen ion conductivity of $Ln_2Ce_2O_7$ (Ln=La, Nd, Sm, Gd, Yb) at 900°C and enthalpy of oxygen ion mobility ($\Delta H_{m,O2-}$) versus the radii of Ln^{3+}.

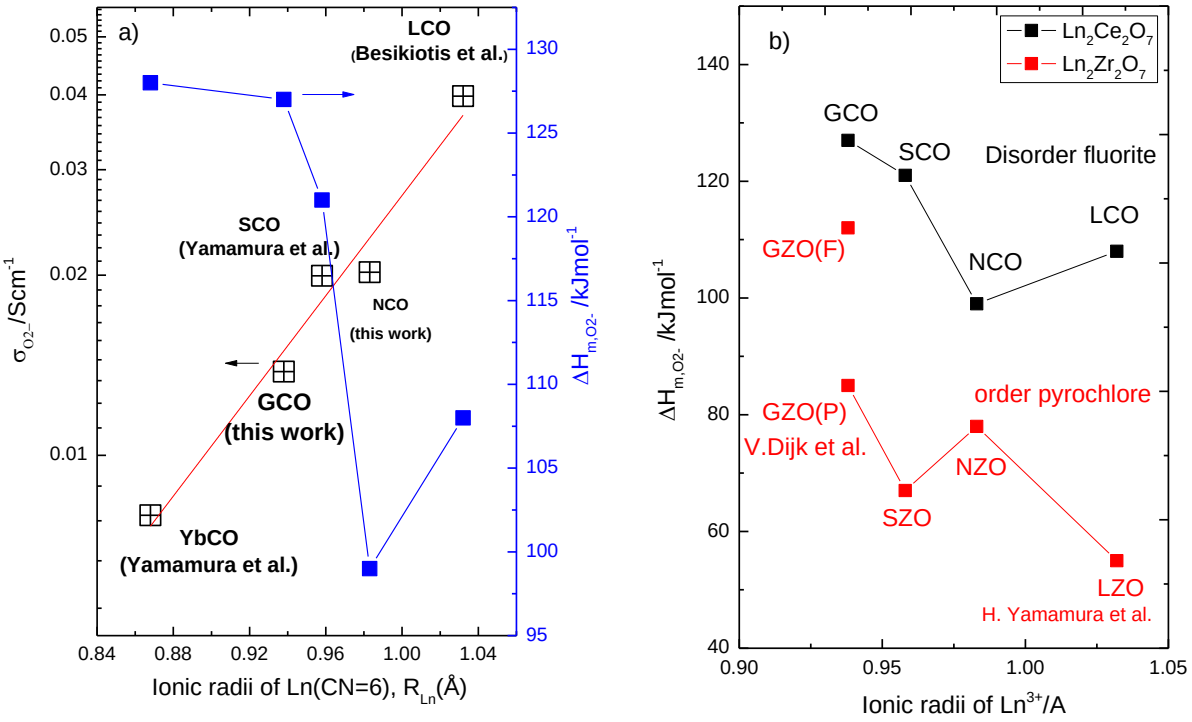

Figure 6.1 a) Oxygen ion conductivity at 900°C (left axis) and enthalpy of mobility vs. ionic radii of Ln^{3+} in $Ln_2Ce_2O_7$ (right axis). Besikiotis's [71] Yamamura's [28] works are included for comparison b) comparison of enthalpy of oxygen ion mobility between $Ln_2Ce_2O_7$ and $Ln_2Zr_2O_7$ pyrochlore [53].

The oxygen ion conductivity increases linearly with increasing ionic radius of Ln^{3+} whereas $\Delta H_{m,O2-}$ is lower for the larger radius of Ln^{3+}. These trends are in accordance with Eurenius's findings for the in $A_2Sn_2O_7$ (A=La, Sm, Gd, Y) pyrochlore system [67]. The trend suggests that it is more favorable for oxygen ion to transport in $Ln_2Ce_2O_7$ with larger lanthanide site. Figure 6.1b displays the comparison between disordered fluorite $Ln_2Ce_2O_7$ and ordered pyrochlore $Ln_2Zr_2O_7$ with respect to the enthalpy of oxygen ion mobility. Due to the smaller cations at the B site, materials as $Ln_2Zr_2O_7$ tend to be stabilized as pyrochlore phase. Similar as $Ln_2Ce_2O_7$, $\Delta H_{m,O2-}$ of $Ln_2Zr_2O_7$ is also inversely proportional to the size of Ln^{3+}. The possible explanation for the trend is that the larger lanthanide will attribute to larger cell volume which possesses a relative large space facilitating oxygen ion mobility. Moreover, since anion

disorder slightly changes with changing the radius of Ln^{3+} in $Ln_2B_2O_7$ [48], the decreasing $\Delta H_{m,O2-}$ with decreasing radius of Ln^{3+} is not due the anion disorder, but the cell volume.

In addition, it is interesting that $\Delta H_{m,O2-}$ of disordered fluorite $Ln_2Ce_2O_7$ (including F-type GZO) is much higher than that of pyrochlore $Ln_2Zr_2O_7$. Yamamura's [53] and Dijk's studies [50] also proposed that anion disorder may enhance $\Delta H_{m,O2-}$ in pyrochlore oxides. Furthermore, Pirzada's calculation [51] shows that pyrochlore oxides with higher degrees of anion disorder display higher activation energy, which is in accordance with the trend in $Ln_2Ce_2O_7$ and $Ln_2Zr_2O_7$. The variation of $\Delta H_{m,O2-}$ in order and disorder GZO suggests that degree of anion disorder may play a vital role in the transport of oxygen ions rather than cell volume. Since anion disorder will increase considerably with an increase in the B cation radius in $Ln_2B_2O_7$ [48], thereby, the main reason for difference of $\Delta H_{m,O2-}$ in $Ln_2Ce_2O_7$ and $Ln_2Zr_2O_7$ is the large difference in degree of anion disorder. As shown in Figure 6.2, there are three available pathways for the oxygen ion to migrate: 48f to 48f, 48f to 8a and 48f to 8b. According to the calculation from Dijk's model [50], the 48f to 48f is the most favorable paths and the oxygen ion consequently jump along this energetically preferential trajectory. Nevertheless, for disordered fluorite (cf. Figure 6.2 left), there is solely 8c oxygen sublattice which is as an average site of 48f, 8a, 8b site. In that case, there is no favorable pathway 48f-48f in the disordered fluorite. The energy barrier for migration of oxygen ions in terms of pathway 8c-8c in disordered fluorite should be much higher than that in 48f-48f hopping. Therefore, it is valid for the higher enthalpy of oxygen ion mobility in the disordered fluorite.

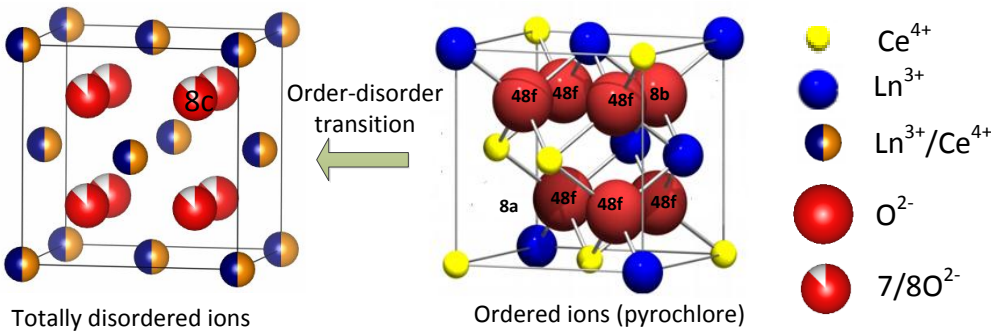

Figure 6.2 1/8 of unit cell transition from pyrochlore to disordered fluorite.

On the other hand, cation disorder might also affect the mobility of oxygen ions. As Figure 6.2 shows, the cations become disordered from pyrochlore to disordered fluorite. With the increasing degree of cation disorder, disordered cations start to hinder the migration of oxygen ions because oxygen vacancies can be easily trapped by the surrounding negatively charged cation anti site defects. In that case, the jump barrier for the disordered fluorite will be higher than the pyrochlore due to the defect association. In sum, combining $Ln_2Ce_2O_7$ and

$Ln_2Zr_2O_7$ system, the cation and anion disorder will determine the oxygen ion mobility in the pyrochlore related materials.

Proton conduction

Figure 6.3a displays the proton conductivity of $Ln_2Ce_2O_7$ (with and without calcium dopants), while Figure 6.3b shows the water uptake in mol H_2O per mol sample, versus ionic radius of Ln^{3+}. As for the oxide ion conductivity, the proton conductivity of both doped and undoped samples increase linearly with increasing radius of Ln^{3+}. Figure 6.3b indicates that also the proton dissolution is more favorable for $Ln_2Ce_2O_7$ with larger lanthanides, however, with a less pronounced dependency on the Ln^{3+} radius. According to DFT calculation from Bjørheim et al. [110], the absolute value of hydration enthalpy of $Ln_2Ce_2O_7$ decreases with decreasing ionic radius of lanthanides, indicating that proton dissolution may less favorable in smaller size lanthanides, which is in agreement with findings in this work.

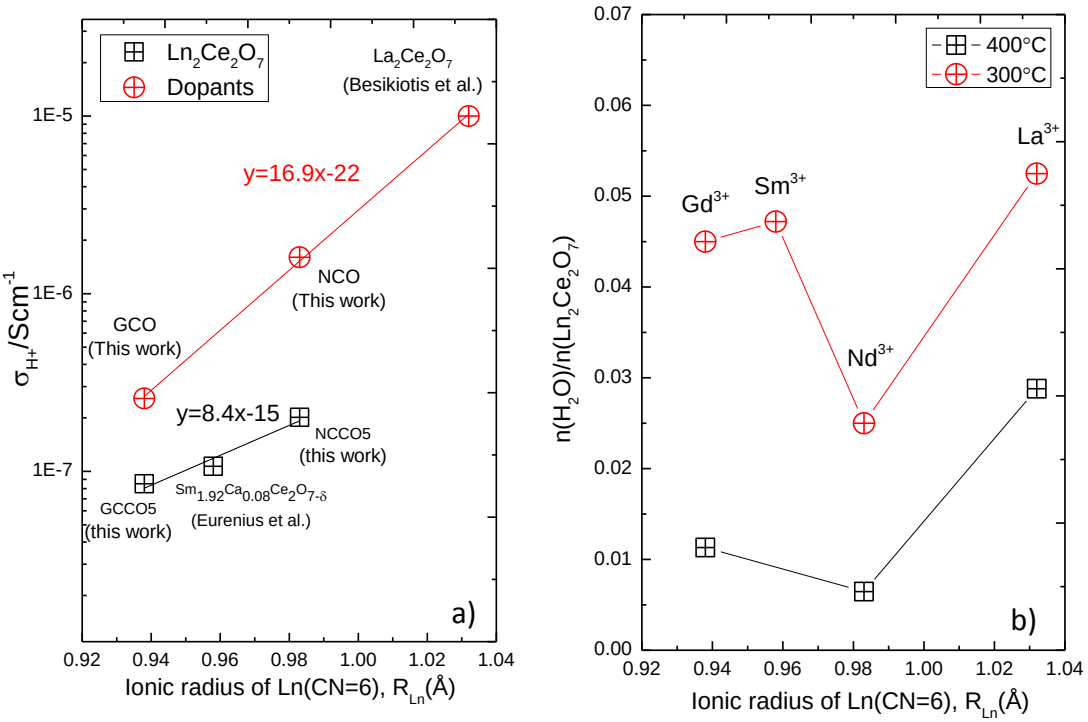

Figure 6.3 a) Proton conductivity at 400°C vs. ionic radii of Ln^{3+} in $Ln_2Ce_2O_7$ b) water uptake per mol sample of $Ln_2Ce_2O_7$ at 300°C and 400°C. $La_2Ce_2O_7$ done by Besikiotis et al. [71] and $Sm_{1.92}Ca_{0.08}Ce_2O_{7-\delta}$ done by Eurenius et al. [68] are included for comparison.

Hence, one may conclude that the $Ln_2Ce_2O_7$ with larger lanthanides exhibit the higher proton mobility. In the $Ln_2Ce_2O_7$ system, both the proton concentration and proton mobility decrease with decreasing lanthanide size. The trend presented in this work in accordance with Eurenius's findings in pyrochlores $Ln_{1.96}Ca_{0.04}Sn_2O_{7-\delta}$ (Ln=La, Sm, Yb) [66]. Furthermore, this relationship were also found in many other families of materials, such as Ln_6WO_{12} (Ln=La,

Nd, Gd, Er) [76], 1% calcium doped Ln_2O_3 (Ln=Sm, Gd, Er, Yb) [79]. $Ln_{1-x}Ca_xNbO_4$ (Re=La, Nd, Gd, Tb, Er, Y, x=0.01-0.05) [77] shows the similar trend in proton mobility.

The decrease encountered in the mobility can be due to the decreasing polarizability of lattice and the proton hosting oxide ion sublattice. A smaller and stiffer lattice gives less dynamics and the oxygen ions will have less chance of being momentarily very close so that proton can transfer. In addition, the decreasing size of lanthanide will decrease the symmetry of $Ln_2Ce_2O_7$ (cf. Table 3.4), which might be another possible reason for the decreasing mobility.

On the other hand, it is possible that anion disorder may affect the proton transport. As discussed about oxygen ion mobility, the migration pathway of oxygen ion is different in disordered fluorite and pyrochlore. Protons jumps through the Grotthuss mechanism in which it jumps from one oxygen ion to a neighboring one and reorients before the next jump. It is therefore plausible that the transport of protons will change with the changing of the migration pathway of oxygen ions. As introduced in 3.2.2, for the pyrochlore oxides, the most favorable site for the H-O is the 96g site [65] and protons diffuse in path between two neighboring 96g sites. Since all oxygen sites are almost indistinguishable in disordered fluorite, the pathway for each jump will be shorter compared with that in pyrochlore. The shorter pathway may not necessary to enhance the proton mobility, but it will affect the proton transport.

In addition, the levels of proton conductivity of NCO and GCO are reduced upon acceptor doping , in-line with Besikiotis's recent study [72] on $La_2Ce_2O_7$ is lower than undoped sample. Due to the linear fit of logarithm proton conductivity and ionic radius of lanthanides, it is valid to predict that proton conductivity of calcium doped $Sm_2Ce_2O_7$ is lower than that of undoped sample. Hence, the family of $Ln_2Ce_2O_7$ materials exhibit negative effect of doping in proton conduction. The fluorite related La_6WO_{12}, which also are dominated by oxygen disorder [111, 112], similarly exhibits a negative effect of doping on the proton conductivity upon acceptor doping [76]. In all these systems with dominating intrinsic disorder, a small acceptor concentration does not affect the concentration of protons as it does in order oxides. Moreover, protons could be trapped by the acceptor dopant yielding to lower mobility and, accordingly, lower proton conductivity. Although we cannot get direct evidence of trapping protons from activation energy ($1/2\Delta H^0_{hydr}+\Delta H_m$), the indication of trapping of oxygen vacancies suggests protons may also associate with the acceptor dopant. Furthermore, since the cations are so similar in disordered fluorites, the calcium can substitute both the Ln^{3+} and Ce^{4+} sites. In that case, the substitution on Ce^{4+} sites with double charge may seriously trap the protons due to the higher coulombic force. In addition

to trapping the protons, substitution of calcium on the Ln^{3+} site may change the environment of the oxygen vacancies on the oxygen sublattice, resulting in less favorable dissolution of protons or fewer numbers of paths the proton may follow by in local ordering of the oxygen lattice.

On the other hand, the decreased basicity with the introduction of Ca^{2+} in $Ln_2Ce_2O_7$ may decrease the sticking probability as a jumping proton exhibits weaker interaction with the surrounding oxygen ions, which may be a result of reducing the proton mobility. In sum, the trapping of proton may be the overriding reason for the negative effect of doping.

6.4. Defects and diffusion at low temperatures (100°C to -60°C)

6.4.1. Protonic conduction at room temperature

NCO, GCO and GCCO5 (Figure 5.23) all exhibit enhanced conductivity from 100°C to room temperature under wet conditions. From the results, the conductivity does not show the effect of doping because the close conductivity between GCO and GCCO5. According to the modeled results in the high temperature (cf. Figure 5.18), oxide ion and p-type conductivity must not be significant in room temperature because of the large activation energy of charge mobility.

In addition, this enhanced conductivity cannot be detected in the dry atmosphere. Also, TG data (cf. Figure 5.28) displays that GCO takes up 0.05 mole water per mole sample which is much larger than the water absorption in 300°C (cf. Figure 5.20c). Hence, water is believed to play a vital role in the electrical behavior at room temperature. Based on these results, such significant enhanced conductivity below 100°C is ascribed to the presence of protons in the materials.

As can be seen from Figure 5.25, charges conducting on the surface will be shield by the guard electrode and the shielded surface electrical conductivity is at most 7% of the total conductivity at room temperature which can be neglected. Hence, conductivity can attribute to internal parts of the sample. The impedance spectra measured at room temperature was deconvoluted by the equivalent circuit (R_1Q_1) whose capacitance is in the range of $10^{-12}Fcm^{-1}$ that follows the typical value of specific capacitance from grain interior.

In Figure 5.26, the slope from linear fit of logarithm conductivity versus log pH_2O is approximately around 2.8, far higher than the relative slope in the high temperatures. In the Brouwer diagram (cf. Figure 2.3), the maximum value of the slope regarding logarithm proton concentration versus log pH_2O is up to 0.5. The bulk conductivity measured in D_2O-wetted oxygen is a little higher than the value measured in H_2O-wetted oxygen within the

ratio around 1.07, indicating H^+/D^+ isotope effect. Nevertheless, since there is a little difference between pH_2O and pD_2O when changing from H_2O-wetted to D_2O-wetted atmosphere, assuming 0.027atm to 0.025atm, the ratio can be a result of the conductivity change with changing between pD_2O and pH_2O. The ratio is approximate 1.25 derived from the pH_2O dependency of 2.8, which is comparable to the ratio 1.07 from measurement. This estimation indicates there is insignificant isotope effect in the protonic conduction. Based on the relatively strong pH_2O dependency and insignificant isotope effect, the protonic concentration does not follow the expected Brouwer diagram (cf. Figure 2.3).

6.4.2. Parallel grain boundary brick layer model

Figure 6.4 displays the protonic conductivity of nanocrystalline gadolinium-doped ceria (GDC), yttrium stabilized zirconia (YSZ), CeO_2 and microcrystalline materials studies in this work at 30°C as a function of grain size.

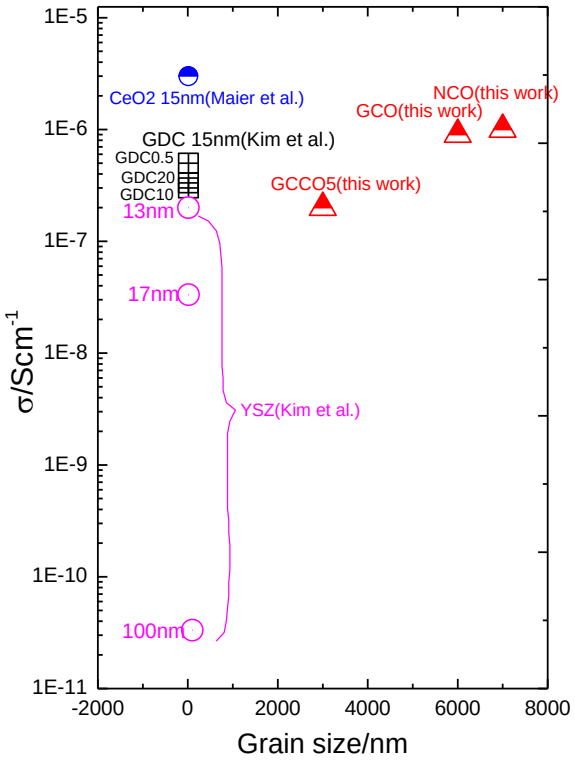

Figure 6.4 Protonic conductivity of GDC [81], YSZ [81], ceria [82] and materials in this work at 30°C as a function of grain size.

As shown in Figure 6.4, besides on the microcrystalline compounds in this work, the similar electrical behaviors are also found in some nanocrystalline materials with fluorite related crystal structure, such as gadolinium doped ceria [84], yttrium stabilized zirconia [81], ceria [82]. Assuming that the defects and the diffusion mechanisms are the same in microcrystalline materials and nanocrystalline materials, the size of the grain may not reveal any necessary relationship with the protonic conduction. Moreover, the protonic conduction

is determined by the material because the ceria related materials exhibit much higher conductivity than zirconia related materials (cf. Figure 6.4).

One possible explanation for the low temperature protonic conduction is the so called parallel brick layer model [84, 85]. In this model, protons were assumed to conduct in the pathway of the parallel grain boundary as introduced in section 3.3, in other words, the grain boundary short circuit the grain interior. Therefore, in this case, the total circuit will be simplified to be just one parallel circuit, which reads ($R_{gb,\parallel}C_t$). Since the total capacitance of the circuit in Figure 2.7 gives

$$C_{tot} = C_{gb,\parallel} + \frac{C_{Bulk}C_{gb,\perp}}{C_{Bulk} + C_{gb,\perp}} \qquad \textbf{Equation 6-8}$$

Since the $C_{gb,\perp} \gg C_{Bulk} \gg C_{gb,\parallel}$ for the microcrystalline ceramics, the following relationship can be derived as $C_{tot} \approx C_{Bulk}$. Thereby, the capacitance for this model should be close to the capacitance from the bulk. As shown in Table 5.9, the capacitance deconvoluted by the equivalent circuit (RQ) is in the range of $pFcm^{-1}$ that may follow the relative value of capacitance from the parallel grain boundary brick layer model. Furthermore, according to Maier's estimation [82], the concentration of protons hydrated at the grain boundary core within 1nm should be 3 orders of magnitude higher than the bulk, which suggests the electrical conductivity of the parallel grain boundary can be 1000 times as the bulk if the proton mobility are the same in the two pathways. Based on these assumptions, we may know the relatively high protonic conductivity in room temperature might be a result of large concentration of protons diffusing along the grain boundary.

Nevertheless, although the impedance spectra match the estimating results based on this model, the extremely high parallel grain boundary conductivity is still controversial because the reason for the high proton mobility diffusing along the grain boundary cannot be well explained in this work. On the other hand, since the oxygen vacancies in the grain boundary core are hydrated to form the protons, such hydration should be consistent with defect chemistry in the bulk. However, in this work, the strong dependency in pH_2O (cf. Figure 5.26) and insignificant isotope effects (cf. Figure 5.27) cannot be well explained due to the brick layer model. In that case, the brick layer model is inappropriate to explain the protonic conduction at low temperatures in this work.

6.4.3. Pore model

Protons can diffuse in the form of hydronium ions (H_3O^+) by forming hydrogen bond between protons and water molecules. In the porous materials, the water can chemisorbed or physisorbed into the pores or cracks in the sample.

In Figure 6.5, water can interact with the surface by following acid/base reactions of Lewis acid site. Protonation reaction will happen if surface show strong Lewis acid/base activity [86]. For instance, CeO_2 has been confirmed to be a solid acid [113] showing a tendency to donate a proton or accept an electron pair, while ZrO_2, as a solid base, tends to presence strong activity accept hydrogen. In the ceria based materials, the protons in the absorbed water will be delocalized due to the surface catalyst effect so that proton will transport in the form of hydronium ions. Furthermore, the phase behavior of liquids can be greatly affected by the presence of solid surfaces [114] and the large internal surface will play a role in heterogeneous catalyst. In the pore model, water condensed inside the pore is assumed to support the pathway for the diffusion of the protons and more water will be absorbed in the pore in higher pH_2O.

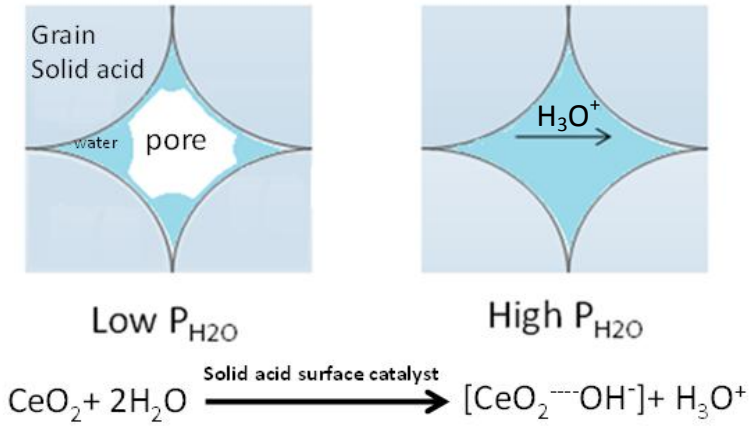

Figure 6.5 Schematic of the condensed water in the pore model.

The relative density of NCO and GCO is around 75%, which demonstrates that the two samples are quite porous, as is evident from the SEM images of NCO and GCO (cf. Figure 5.8). According to the previous study, the water molecules tend to interact with the surface hydroxyl groups of CeO_2 [115], so it is valid to consider hydronium ions as the predominating charge carrier conducts in the water condensed in NCO and GCO. The enhancement of the conductivity from 100°C to 25°C can be ascribed to the content of water in the pore, which is inversely proportional to the temperature (cf. Figure 5.23). The linear pH_2O dependency at 25°C and 30°C may be attributed to the big change of the content of condensed water with the changing pH_2O. Furthermore, Shirpour et al. [82] proposed that the water in the pore might be a possible reason for the low temperature because the relative dielectric constant of the impedance spectra of ceria differ considerably between wet and dry condition below 250°C. As shown in Figure 6.6, the relative dielectric constant of NCO, GCO and CeO_2 at room temperature are much higher than that at 400°C. Moreover, the enhanced dielectric constant of NCO, GCO and ceria at room temperature is close to that of water. The change in

dielectric constants of these compounds indicates a different conduction mechanism in room temperature. Since the relative dielectric constant of NCO, GCO and ceria is close to that of water, water is thereby suggested to be the pathway for protonic defects transport at low temperatures.

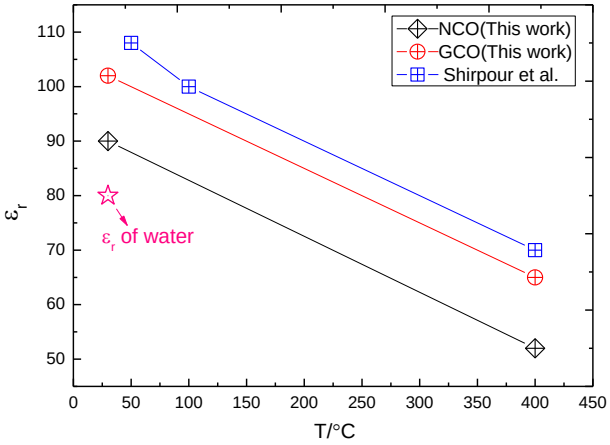

Figure 6.6 Relative dielectric constant (ε_r) obtained from the capacitance values relative to the single semicircle at 25°C and 400°C in this work and CeO_2 nanocrystalline from Shirpour et al. [82].

The electrical measurement carried out under freezing point support the evidence for pore model. As can be seen from Figure 5.29, the sharp decline of the total conductivity from room temperature to freezing point might be attributed to the dramatical decline of the pH_2O in the close cell. With decreasing temperature, the water can not only condense inside the pore but also condense on the surface of other things, such as inner surface of the quartz tube. So, it is valid to estimate the water condensed in the pore can be seriously captured by the surrounding things with decreasing temperature. Therefore, it is no surprises for such conductivity decline combining the strong pH_2O dependency (cf. Figure 5.26). In addition, the conductivity transition point in H_2O-wetted O_2 is around -2°C which is a little below the theoretical freezing point. One possible reason for the deviation that the freezing point water condensed in the pore might be impacted by the surrounding environment, such as capillary pressure from internal surface. Another possible reason is due to the kinetics that the conductivity did not reach the equilibrium at 0°C. Furthermore, the deviation of the freezing point also happened in D_2O-wetted O_2. One should note that the relative difference between the transition points in H_2O-wetted O_2 and D_2O-wetted O_2 is approximate 3°C which is in agreement with the difference between the freezing points of H_2O and D_2O. This isotopic check experiments not only demonstrate the results measured in normal water are not coincidence, but also suggest the transition of the electrical conductivity at around freezing point might be ascribed to the phase transition from water to ice. Since proton mobility in water is much lower than that in ice [116], the regression of

the conductivity below 0°C might be ascribed to the proton mobility change with changing the phases of H_2O. Since the mobility of proton is inversely proportional to the temperature, so it is valid for conductivity to decline after reaching a maximum point.

The pore model may satisfactorily explain the enhanced conductivity at room temperature and it can furthermore verified by the measurement carried out under freezing point. Furthermore, pore model was confirmed by using the in-situ Infrared spectroscopy on the investigation of the nano-YSZ ceramics at H_2O and CH_3OH [87]. If so, accordingly, the electrical conductivity in room temperature will be determined by the properties of the inner surface, size and distribution of the pore.

In summary, combining the results carried out in low temperature in this work with the previous studies on this low temperature behavior, pore model tend to be more favorable explanation than the parallel brick layer model. Accordingly, the low temperature protonic conduction is not a result of bulk, but contributed from the water in the pores.

6.5. Proton diffusion mechanisms from 1100°C to -60°C

Based on the discussion about the protonic conduction at high and low temperatures, various proton transport mechanisms are summarized from high to low temperature in this work. Figure 6.7 displays the temperature dependency of conductivity of GCO from 1100°C to -60°C.

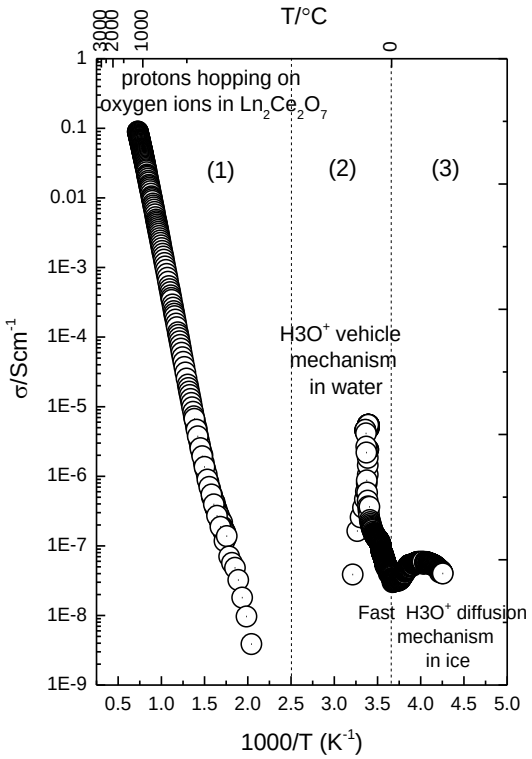

Figure 6.7 Full overview of protonic conduction of GCO from 1100°C to -60°C.

In region 1, from 1100°C to 200°C, diffusion of protons follows the free transport mechanism that proton jumps from an oxide ion to a neighboring one in the crystal lattice. From 100°C to 25°C, proton transport follows the vehicle mechanism that H_3O^+ serve as vehicles for proton diffusion. Under freezing point, fast proton transport happen in ice. Protons may diffuse by means of successive proton jumps (Grotthuss mechanism) or the orentational defects (Bjerrum defects) [117] in ice.

6.6. Future work

First of all, since the phases in the samples are not completely determined in this work, the main extension of this work should be emphasized on the structure investigation. TEM or Neutron diffraction is available to determine the crystal structure, especially on the occupation of cations and anions. It is suggested that GCO exhibits phase transition from C-type to F-type in elevated temperature. Thus, high temperature XRD can be used to investigate the crystal structure concerning the order-disorder phase transition at elevated temperature.

Secondly, TG-DSC can be utilized to investigate the hydration enthalpy of samples in this work. Furthermore, TG measurement regarding isothermal pO_2 and pH_2O dependency can help to determine the thermodynamic constants. The stoichiometry of the samples can be due to the existing Ce^{3+}. It is interesting to introduce XPS to analysis the relative concentration of Ce^{3+} and Ce^{4+}. In addition, it is necessary to use Electron probe micro-analyzer (EPMA) to investigate if there are some domains which is rich in rare earth elements. This may support the indication whether the insignificant doping effect is due to cation disorder.

Thirdly, for the protonic conductor in room temperature, it is interesting to measure the single crystal sample at low temperatures to confirm the pore model. As discussed in 6.4.3, since internal surface plays vital role in the hydronium ions concentration or mobility, samples with nano-sized porous might enhance the protonic conduction due to the large internal surface area. The extension of work is to characterize the protonic conduction of the nano-sized ceramic. Electromotive force (EMF) can be utilized to measure the transport number of hydronium or hydroxide ions in the nano-sized ceramics. Furthermore, in order to clarify mechanism of protonic conduction at low temperatures, solid state NMR (nuclear magnetic resonance) and in-situe FTIR (Fourier Transform infrared spectroscopy) may be utilized to analyze protons in the samples. In addition, the protonic conduction of ceria based material is higher than that zirconia based materials. It is interesting to measure the protonic conduction of other oxides e.g. Fe_2O_3, ZnO, TiO_2 etc. This work may help to find potential materials used in low temperature fuel cell.

7. Conclusions

From the XRD results and Rietveld refinement, $Nd_2Ce_2O_7$ crystallizes in a cubic F-type structure with the oxygen occupancy of around 0.875 while $Gd_2Ce_2O_7$ crystallizes in a C-type structure with oxygen occupancy close to 1. Based on the SEM-EDS results and lattice parameters obtained from Rietveld refinement, the solubility of calcium in $Nd_2Ce_2O_7$ is below 10% but larger than 20% in $Gd_2Ce_2O_7$.

Based on the modeling results of pO_2 and pH_2O dependency of conductivity, it can be concluded that oxygen vacancies dominate under a wide range of oxidizing conditions. The calcium doped and undoped compounds show a mixed n-type and oxygen ion conduction under reducing conditions and a mixed p-type and oxygen ion conduction under oxidizing conditions. Enthalpies of mobility of oxygen ions conduction of $Nd_2Ce_2O_7$ and $Gd_2Ce_2O_7$ are 99 ± 2 kJmol^{-1} and 127 ± 2 kJmol^{-1}, respectively. Enthalpy of mobility of oxygen ion of 5% calcium doped $Nd_2Ce_2O_7$ and $Gd_2Ce_2O_7$ increase to 123 ± 2 kJmol^{-1} and 133 ± 2 kJmol^{-1}, respectively, indicating association between oxygen vacancies and acceptor dopants. Electrical measurement and thermogravimetry confirmed the proton conduction in $Nd_2Ce_2O_7$ and $Gd_2Ce_2O_7$ under wet conditions. It can be concluded that proton is formed by hydration of the intrinsic oxygen vacancies. The lower proton conduction in 5% calcium doped compounds than undoped samples is suggested to be due to trapping of protons by the acceptor dopants.

Proton mobility and dissolution decrease with decreasing ionic radius of lanthanides in $Ln_2Ce_2O_7$. The decreasing proton mobility can be due to the decreasing polarization of lattice or symmetry. The decreasing enthalpy of oxygen ion mobility with increasing Ln^{3+} in $Ln_2B_2O_7$ (B=Ce, Zr) is due to the larger cell volume space facilitating oxygen mobility. The higher enthalpy of oxygen ion mobility in $Ln_2Ce_2O_7$ than that in $Ln_2Zr_2O_7$ is suggested to be related to the cation and anion disorder. The pathway of proton diffusion is related to the anion disorder. It can therefore be concluded that the migration of oxygen ions and protons are affected by the degree of disorder in $Ln_2B_2O_7$ (B=Ce, Zr).

The conductivity dependency of temperature below 100°C and thermogravimetry suggest the enhanced total conductivity in $Nd_2Ce_2O_7$ and $Gd_2Ce_2O_7$ blow 100°C is due to protonic conduction which is independent of dopant concentration and grain size. It is suggested that the pathway of protons is neither in the bulk nor along grain boundaries due to the result $\sigma \propto pH_2O^{2.8}$ and insignificant isotope effect. Protons are expected to migrate in water condensed in micro-sized pores or cracks in the form of hydronium ions. The electrical measurement below 0°C suggested phase transition of water in the pore around 0°C,

further confirming that low temperature protonic conduction results from hydronium ions transport in the water.

8. References

1. Intergovernmental Panel on Climate change. IPCC Fourth Assessment Report Climate change, 2007.
2. International Energy Agency, CO_2 emission from fuel combustion highlights, 2011.
3. Full Manua Loa CO_2 record, www.esrl.noaa.gov/gmd/ccgg/trends/(2012).
4. *Comparison of Fuel Cell Technologies*, www.eere.energy.gov/informationcenter(17.01.2011)
5. Lefebvre-Joud, F., Gauthier, G., and Mougin, J., *Current status of proton-conducting solid oxide fuel cells development.* J. Appl. Electrochem. , 2009. **39**(4): p. 535-543.
6. Norby, T. and Larring, Y., *Mixed hydrogen ion-electronic conductors for hydrogen permeable membranes.* Solid State Ionics, 2000. **136-137**(2): p. 139-148.
7. Norby, T. and Kofstad, P., *Defects and transport in crystalline solids*, 2007, University of Oslo. p. 5.14.
8. Norby, T. *Electrical measurements*. Compendium for the advanced level course: Experimental methods KJM-MENA4010 Module 2, 2009, University of Oslo.
9. Tilley, R.J.D., *Defects in Solid,* 2008, Canada, John Wiley & Sons, Inc.
10. Chavan, S.V. and Tyagi, A.K., *Phase relations and lattice thermal expansion studies in the $Ce_{0.50}RE_{0.5}O_{1.75}$ (RE=rare-earths).* Mater. Sci. Eng. A, 2005. **404**(1–2): p. 57-63.
11. Norby, T., *A Kröger-Vink Compatible Notation for Defects in Inherently Defective Sublattices,* J. Korean Ceram. Soc., 2010. **47**(1): p. 19-25.
12. Fjeld, H., *Impedance spectroscopy: with emphasis on applications towards grain boundaries and electrodics*, 2008, University of Oslo.
13. Haile, S.M., West, D.L., and Campbell, J., *The role of microstructure and processing on the proton conducting properties of gadolinium-doped barium cerate.* J. Mater. Res., 1998. **13**(6): p. 1576-1595.
14. Brauer, G. and Gradinger, H., *Die Oxydsysteme des Cers und des Praseodyms.* Z. Anorg. Allg. Chem., 1954. **277**: p. 89-95.
15. Stanek, C.R., *Atomic Scale Disorder in Fluorite and Fluorite Related Oxides, Department of Materials,* 2003, Imperial College of Science, p. 20.
16. Cai, L., Arias, A.L., and Nino, J.C., *The tolerance factors of the pyrochlore crystal structure.* J. Mater. Chem., 2011. **21**(11): p. 3611-3618.
17. J., E., Harvey, K.R.W., Gregory, R.L., Ronald, I.S., and Simon, A.T., Redfern J. Solid state chem., 2005. **178**: p. 800.
18. Wuensch, B. and Eberman, K., *Order-disorder phenomena in pyrochlore oxides.* J.O.M. , 2000. **52**(7): p. 19-21.
19. Mandal, B.P. and Tyagi, A.K., *Pyrochlores: Potential multifunctional materials.* Mater. Res. Bull, 2010(313): p. 6-13.
20. Heremans, C., Wuensch, B.J., Stalick, J.K., and Prince, E., *Fast-Ion Conducting $Y_2(Zr_yTi_{1-y})_2O_7$ Pyrochlores: Neutron Rietveld Analysis of Disorder Induced by Zr Substitution.* J. Solid State Chem., 1995. **117**(1): p. 108-121.
21. Wuensch, B.J., Eberman, K.W., Heremans, C., Ku, E.M., Onnerud, P., Yeo, E.M.E., Haile, S.M., Stalick, J.K., and Jorgensen, J.D., *Connection between oxygen-ion conductivity of pyrochlore fuel-cell materials and structural change with composition and temperature.* Solid State Ionics, 2000. **129**(1–4): p. 111-133.
22. Zhang, F.X., Lian, J., Becker, U., Wang, L.M., Hu, J., Saxena, S., and Ewing, R.C., *Structural distortions and phase transformations in $Sm_2Zr_2O_7$ pyrochlore at high pressures.* Chem. Phys. Lett., 2007. **441**(4–6): p. 216-220.
23. Zhang, F.X., Lian, J., Becker, U., Ewing, R.C., Hu, J., and Saxena, S.K., *High-pressure structural changes in the $Gd_2Zr_2O_7$ pyrochlore.* Phys. Rev. B, 2007. **76**(21): p. 214104.
24. Zhang, F.X., Manoun, B., and Saxena, S.K., *Pressure-induced order-disorder transitions in pyrochlore $RE_2Ti_2O_7$ (RE = Y, Gd).* Mater. Lett. , 2006. **60**(21-22): p. 2773-2776.

25. Lian, J., Zu, X.T., Kutty, K.V.G., Chen, J., Wang, L.M., and Ewing, R.C., *Ion-irradiation-induced amorphization of $La_2Zr_2O_7$ pyrochlore.* Phys. Rev. B, 2002. **66**(5): p. 054108.
26. Adachi, G., Imanaka, N., and Kang, Z.C., *Binary Rare Earth Oxides,* 2004, The Netherlands., Kluwer Academic.
27. Bommer, H., *Die Gitterkonstanten der C-Formen der Oxyde der seltenen Erdmetalle.* Zeitschrift fuer Anorganische und Allgemeine Chemie, 1939. **241**: p. 273.
28. Yamamura, H., Nishino, H., Kakinuma, K., and Nomura, K., *Crystal Phase and Electrical Conductivity in the Pyrochlore-Type Composition Systems, $Ln_2Ce_2O_7$ (Ln=La, Nd, Sm, Eu, Gd, Y and Yb).* J. Ceram. Soc. Jpn., 2003. **111** (1300): p. 902-906
29. Shanon, R.D., *Revised effective ionic radii and systematic studies of interatomic distances in halides and chalcogenides.* Acta Cryst., 1976. **A32**(part 5): p. 751-757.
30. Maki, Y., Matsuda, M., and Kudo, T., *SOLID ELECTROLYTE FUEL CELL*, 1971: U.S. patent.
31. Sachdeva, A., Chavan, S.V., Goswami, A., Tyagi, A.K., and Pujari, P.K., *Positron annihilation spectroscopic studies on Nd-doped ceria.* J. Solid State Chem., 2005. **178**(6): p. 2062-2066.
32. Brauer, G. and Gradinger, H., *Ueber heterotype Mischphasen bei Seltenerdoxyden. I.* Z. Anorg. Allg. Chem., 1954. **276**: p. 209-226.
33. Mandal, B.P., Grover, V., Roy, M., and Tyagi, A.K., *X-Ray Diffraction and Raman Spectroscopic Investigation on the Phase Relations in Yb_2O_3- and Tm_2O_3-Substituted CeO_2.* J. Am. Ceram. Soc., 2007. **90**(9): p. 2961-2965.
34. Liu, Z.G., Ouyang, J.H., and Sun, K.N., *Electrical Conductivity Improvement of $Nd_2Ce_2O_7$ Ceramic Co-doped with Gd_2O_3 and ZrO_2.* Fuel Cells, 2011. **11**(2): p. 153-157.
35. Chakraborty, K.R., Krishna, P.S.R., Chavan, S.V., and Tyagi, A.K., *A neutron diffraction study on ceria - neodia solid solutions.* Powder Diffr., 2006. **21**(01): p. 36-39.
36. Takeshi, H., Zuiho, K., Akitaka, M., and Hiroshi, Y., *Formation of C-type rare earth structures in the $Ce_{1-x}Nd_xO_{2-\delta}$ system: a factor in the decrease in oxide-ion conductivity.* J. Ceram. Soc. Jpn., 2009. **117**(12): p. 1306-1310.
37. Chavan, S.V., Mathews, M.D., and Tyagi, A.K., Mater. Res. Bull., 2005. **40**: p. 1558.
38. Pieczulewski, C.N., Kirkpatrick, K.S., and Mason, T.O., *1000°C Phase Relations and Superconductivity in the (Nd-Ce-Cu)-O Ternary System.* J. Am. Ceram. Soc., 1990. **73**(7): p. 2141-2143.
39. Ye, F., Mori, T., Ou, D.R., Zou, J., and Drennan, J., *A structure model of nano-sized domain in Gd-doped ceria.* Solid State Ionics, 2009. **180**(26–27): p. 1414-1420.
40. Li, Z.-P., Mori, T., Ye, F., Ou, D.R., Zou, J., and Drennan, J., *Structural phase transformation through defect cluster growth in Gd-doped ceria.* Phys. Rev. B, 2011. **84**(18): p. 180-201.
41. Patwe, S.J., Ambekar, B.R., and Tyagi, A.K., *Synthesis, characterization and lattice thermal expansion of some compounds in the system $Gd_2Ce_xZr_{2-x}O_7$.* J. Alloys Compd., 2005. **389**(1-2): p. 243-246.
42. Wang, B., Lewis, R.J., and Cormack, A.N., *Computer simulations of large-scale defect clustering and nanodomain structure in gadolinia-doped ceria.* Acta Mater., 2011. **59**(5): p. 2035-2045.
43. Grover, V. and Tyagi, A.K., *Phase relations, lattice thermal expansion in CeO_2–Gd_2O_3 system, and stabilization of cubic gadolinia.* mater. Res. Bull., 2004. **39**(6): p. 859-866.
44. Scavini, M., Coduri, M., Allieta, M., Brunelli, M., and Ferrero, C., *Probing Complex Disorder in $Ce_{1-x}Gd_xO_{2-x/2}$ Using the Pair Distribution Function Analysis.* Chem. Mater., 2012. **24**(7): p. 1338-1345.
45. Bevan, D.G., Barker, W.W., and Martin, R.L., *The Fourth Conference on Rare Earths Research*. 1965. New York.
46. van Dijk, T., de Vries, K.J., and Burggraaf, A.J., *Electrical conductivity of fluorite and pyrochlore $Ln_xZr_{1-x}O_{2-x/2}$ (Ln = Gd, Nd) Solid Solutions.* physica status solidi A, 1980. **58**(1): p. 115-125.
47. Moon, P.K. and Tuller, H.L., *Ionic conduction in the $Gd_2Ti_2O_7$–$Gd_2Zr_2O_7$ system.* Solid State Ionics, 1988. **28–30, Part 1**(0): p. 470-474.

48. Minervini, L., Grimes, R.W., and Sickafus, K.E., *Disorder in Pyrochlore Oxides.* J. Am. Ceram. Soc., 2000. **83**(8): p. 1873-1878.
49. Wilde, P.J. and Catlow, C.R.A., *Defects and diffusion in pyrochlore structured oxides.* Solid State Ionics, 1998. **112**(3–4): p. 173-183.
50. Dijk van, M.P., Vries de, K.J., and Burggraaf, A.J., *Oxygen ion and mixed conductivity in compounds with the fluorite and pyrochlore structure.* Solid State Ionics, 1983. **9-10**(2): p. 913-919.
51. Pirzada, M., Grimes, R.W., Minervini, L., Maguire, J.F., and Sickafus, K.E., *Oxygen migration in $A_2B_2O_7$ pyrochlores.* Solid State Ionics, 2001. **140**(3–4): p. 201-208.
52. Wilde, P.J. and Catlow, C.R.A., *Molecular dynamics study of the effect of doping and disorder on diffusion in gadolinium zirconate.* Solid State Ionics, 1998. **112**(3–4): p. 185-195.
53. Yamamura, H., Nishino, H., Kakinuma, K., and Nomura, K., *Electrical conductivity anomaly around fluorite–pyrochlore phase boundary.* Solid State Ionics, 2003. **158**(3–4): p. 359-365.
54. Norby, T., *Fast oxygen ion conductors-from doped to ordered systems.* J. Mater. Chem. , 2001. **11**(1): p. 11-18.
55. Yu, T.-H. and Tuller, H.L., *Ionic conduction and disorder in the $Gd_2Sn_2O_7$ pyrochlore system.* Solid State Ionics, 1996. **86–88**(0): p. 177-182.
56. Tuller, H.L., *Mixed ionic-electronic conduction in a number of fluorite and pyrochlore compounds.* Solid State Ionics, 1992. **52**(1–3): p. 135-146.
57. Moriga, T., Yoshiasa, A., Kanamaru, F., Koto, K., Yoshimura, M., and Sōmiya, S., *Crystal structure analyses of the pyrochlore and fluorite-type $Zr_2Gd_2O_7$ and anti-phase domain structure.* Solid State Ionics, 1989. **31**(4): p. 319-328.
58. Shlyakhtina, A.V., Knotko, A.V., Boguslavskii, M.V., Stefanovich, S.Y., Kolbanev, I.V., Larina, L.L., and Shcherbakova, L.G., *Effect of non-stoichiometry and synthesis temperature on the structure and conductivity of $Ln_{2+x}M_{2-x}O_{7-x/2}$.* Solid State Ionics, 2007. **178**(1–2): p. 59-66.
59. Moon, P.K., *Electrical conductivity and structural disorder in $Gd_2Ti_2O_7$-$Gd_2Zr_2O_7$ and $Y_2Ti_2O_7$-$Y_2Zr_2O_7$ solid solutions, Department of Materials science and engineering,* 1988, Massachusetts Institute of Technology , p. 132.
60. Xing, W., Toyoura, K., and Norby, T., *Effect of cation disorder on the solubility and result of doping in oxides*, 2012: Sumitted to Int. J. Hydrogen Energy.
61. Shimura, T., Komori, M., and Iwahara, H., *Ionic conduction in pyrochlore-type oxides containing rare earth elements at high temperature.* Solid State Ionics, 1996. **86–88**(0): p. 685-689.
62. Labrincha, J.A., Frade, J.R., and Marques, F.M.B., *Protonic conduction in $La_2Zr_2O_7$-based pyrochlore materials.* Solid State Ionics, 1997. **99**(1–2): p. 33-40.
63. Omata, T. and Otsuka-Yao-Matsuo, S., *Electrical properties of proton-conducting Ca^{2+}-doped $La_2Zr_2O_7$ with a pyrochlore-type structure.* J. Electrochem. Soc., 2001. **148**(6): p. 252-261.
64. Omata, T., Okuda, K., Tsugimoto, S., and Otsuka-Matsuo-Yao, S., *Water and hydrogen evolution properties and protonic conducting behaviors of Ca^{2+}-doped $La_2Zr_2O_7$ with a pyrochlore structure.* Solid State Ionics, 1997. **104**(3–4): p. 249-258.
65. Björketun, M.E., Knee, C.S., Nyman, B.J., and Wahnström, G., *Protonic defects in pure and doped $La_2Zr_2O_7$ pyrochlore oxide.* Solid State Ionics, 2008. **178**(31–32): p. 1642-1647.
66. Eurenius, K.E.J., Ahlberg, E., and Knee, C.S., *Proton conductivity in $Ln_{1.96}Ca_{0.04}Sn_2O_{7-\delta}$ (Ln=La, Sm, Yb) pyrochlores as a function of the lanthanide size.* Solid State Ionics, 2010. **181**(27–28): p. 1258-1263.
67. Eurenius, K.E.J., Ahlberg, E., and Knee, C.S., *Proton conductivity in $Sm_2Sn_2O_7$ pyrochlores.* Solid State Ionics, 2010. **181**(35–36): p. 1577-1585.
68. Eurenius, K.E.J., Ahlberg, E., and Knee, C.S., *Role of B-site ion on proton conduction in acceptor-doped $Sm_2B_2O_{7-\delta}$ (B = Ti, Sn, Zr and Ce) pyrochlores and C-type compounds.* Dalton Trans., 2011. **40**(15): p. 3946-3954

69. Fjeld, H., Haugsrud, R., Gunnæs, A.E., and Norby, T., *Proton and oxide ion conductivity in grain boundaries and grain interior of Ca-doped $Er_2Ti_2O_7$ with Si-impurities.* Solid State Ionics, 2008. **179**(33–34): p. 1849-1853.
70. Haugsrud, R. and Norby, T. , *26th Risø International Symposium on Materials Science*. 2005. Denmark, Solid State Electrochem.
71. Besikiotis, V., Knee, C.S., Ahmed, I., Haugsrud, R., and Norby, T., *Ionic conductivity and hydration of inherently oxygen-deficient $La_2Ce_2O_7$*, To be submitted, 2012.
72. Besikiotis, V., *Study on $La_2Ce_2O_7$*, Unpublished work, 2009.
73. Chang, L.L.Y., Scroger, M.G., and Phillips, B., *High temperature phase equilibria in the systems Sm_2O_3-WO_3 and Sm_2O_3-W-WO_3.* J. Inorg. Nucl. Chem. , 1966. **28**(5): p. 1179-1184.
74. Aleshin, E. and Roy, R., *Crystal Chemistry of Pyrochlore.* J. Am. Ceram. Soc., 1962. **45**(1): p. 18-25.
75. Diot, N., Larcher, O., Marchand, R., Kempf, J.Y., and Macaudière, P., *Rare-earth and tungsten oxynitrides with a defect fluorite-type structure as new pigments.* J. Alloys Compd., 2001. **323-324**: p. 45-48.
76. Haugsrud, R., *Defects and transport properties in Ln_6WO_{12} (Ln=La, Nd, Gd, Er).* Solid State Ionics, 2007. **178**(7–10): p. 555-560.
77. Haugsrud, R. and Norby, T., *Proton conduction in rare-earth ortho-niobates and ortho-tantalates.* Nat. Mater., 2006. **5**(3): p. 193-196.
78. Zhu, B., Albinsson, I., and Mellander, B., *Electrical properties and proton conduction of gadolinium doped ceria.* Ionics, 1998. **4**(3): p. 261-266.
79. Norby, T., Dyrlie, O., and Kofstad, P., *Protonic Conduction in Acceptor-Doped Cubic Rare-Earth Sesquioxides.* J. Am. Ceram. Soc., 1992. **75**(5): p. 1176-1181.
80. Xia, X.L., Liu, Z.G., Ouyang, J.H., Gao, S., and Liu, X.M., *Effect of Ce substitution for Zr on electrical property of fluorite-type $Gd_2Zr_2O_7$.* Solid State Sci., 2011. **13**(6): p. 1328-1333.
81. Avila-Paredes, H.J., Barrera-Calva, E., Anderson, H.U., De Souza, R.A., Martin, M., Munir, Z.A., and Kim, S., *Room-temperature protonic conduction in nanocrystalline films of yttria-stabilized zirconia.* J. Mater. Chem., 2010. **20**(30): p. 6235-6238.
82. Shirpour, M., Gregori, G., Merkle, R., and Maier, J., *On the proton conductivity in pure and gadolinium doped nanocrystalline cerium oxide.* P.C.C.P, 2011. **13**(3).
83. Kim, S., Anselmi-Tamburini, U., Park, H.J., Martin, M., and Munir, Z.A., *Unprecedented Room-Temperature Electrical Power Generation Using Nanoscale Fluorite-Structured Oxide Electrolytes.* Adv. Mater., 2008. **20**(3): p. 556-559.
84. Avila-Paredes, H.J., Chen, C.-T., Wang, S., De Souza, R.A., Martin, M., Munir, Z., and Kim, S., *Grain boundaries in dense nanocrystalline ceria ceramics: exclusive pathways for proton conduction at room temperature.* J. Mater. Chem., 2010. **20**(45): p. 10110-10112.
85. Kim, S., Avila-Paredes, H.J., Wang, S., Chen, C.-T., De Souza, R.A., Martin, M., and Munir, Z.A., *On the conduction pathway for protons in nanocrystalline yttria-stabilized zirconia.* P.C.C.P, 2009. **11**(17): p. 3035-3038.
86. Shu, Y., Shogo, M., and Takashi, T., *Surface protonic in amorphous film and nanocrystllites*, *7th Petite workshop on the defect chemical nature of energy materials* 2011, Kongsberg, Norway.
87. Pietrowski, M.J., De Souza, R.A., Kim, S., Munir, Z.A., and Martin, M., *Dehydration kinetics of nano-YSZ ceramics monitored by in-situ infrared spectroscopy.* Solid State Ionics, (0).
88. Dai, H., Zhong, X., Li, J., Meng, J., and Cao, X., *Neodymium-cerium oxide as new thermal barrier coating material.* Surf. Coat. Technol., 2006. **201**(6): p. 2527-2533.
89. Zhang, H., Liao, S., Dang, X., Guan, S., and Zhang, Z., *Preparation and thermal conductivities of $Gd_2Ce_2O_7$ and $(Gd_{0.9}Ca_{0.1})_2Ce_2O_{6.9}$ ceramics for thermal barrier coatings.* J. Alloys Compd., 2011. **509**(4): p. 1226-1230.
90. Rietveld refinement, http://en.wikipedia.org/wiki/Rietveld_refinement.(05.27.2012).

91. Rietveld, H.M., *A profile refinement method for nuclear and magnetic structures* J.Appl. Cryst., 1969. **2**: p. 65-71.
92. Rietveld, H.M., *Line profiles of neutron powder-diffraction peaks for structure refinement* Acta Cryst., 1967. **22**: p. 151.
93. Allen, C.L., Robert, B., and Von, D., *GSAS TECHNICAL MANUAL,* 2004.
94. Huse, M., *Transport and hydration in acceptor doped proton conducting oxide-effects of proton-acceptor asscitations*, *Faculty of Mathematics and Natural Sciences,* 2011, University of Oslo. p. 50.
95. *Simultaneous Thermal Analysis Method, Tchnique, Applications*, NETZSCH, 2012.
96. Norby, T. and Kofstad, P., *Electrical Conductivity and Defect Structure of Y_2O_3 as a Function of Water Vapor Pressure.* J. Am. Ceram. Soc., 1984. **67**(12): p. 786-792.
97. Norby, T. and Kofstad, P., *Direct-Current Conductivity of Y_2O_3 as a Function of Water Vapor Pressure.* J. Am. Ceram. Soc., 1986. **69**(11): p. 780-783.
98. *ProGasMixer^{TM} user manual,* NorECs, 02.12.2011.
99. Tyholdt, F., *Electrical conductivity and defect structure of Sr-substituted $LaPO_4$, Department of Chemistry,* 1999, University of Oslo.
100. Thermocouple Accuracy, http://www.microlink.co.uk/tctable.html.(26.01.1996)
101. Avila-Paredes, H.J., Choi, K., Chen, C.-T., and Kim, S., *Dopant-concentration dependence of grain-boundary conductivity in ceria: A space-charge analysis.* J. Mater. Chem., 2009. **19**(27): p. 4837-4842.
102. Zhu, J.X., Zhou, D.F., Guo, S.R., Ye, J.F., Hao, X.F., Cao, X.Q., and Meng, J., *Grain boundary conductivity of high purity neodymium-doped ceria nanosystem with and without the doping of molybdenum oxide.* J. Power Sources, 2007. **174**(1): p. 114-123.
103. Maier, J., *Physical chemistry of ionic materials-Ions and electrons in Solids,* 2004, England, John Wiley & Sons, Ltd.
104. Bonanos, N., *Oxide-based protonic conductors: point defects and transport properties.* Solid State Ionics, 2001. **145**(1-4): p. 265-274.
105. Bjørheim, T.S., *Unpublished work*, 2012.
106. Kofstad, P., *Nonstoichiometry, Diffusion, and Electrical Conductivity in Binary Metal Oxides,* 1972, New York , Wiley-Interscience,.
107. Stephens, I.E.L. and Kilner, J.A., *Ionic conductivity of $Ce_{1-x}Nd_xO_{2-x}$.* Solid State Ionics, 2006. **177**(7–8): p. 669-676.
108. Omar, S., Wachsman, E.D., Jones, J.L., and Nino, J.C., *Crystal Structure–Ionic Conductivity Relationships in Doped Ceria Systems.* J. Am. Ceram. Soc., 2009. **92**(11): p. 2674-2681.
109. Wang, D.Y., Park, D.S., Griffith, J., and Nowick, A.S., *Oxygen-ion conductivity and defect interactions in yttria-doped ceria.* Solid State Ionics, 1981. **2**(2): p. 95-105.
110. Bjørheim, T.S., Besikioti, V., and Norby, T., *Hydration thermodynamics of pyrochlore structure oxides from TG and first principle caculation*, 2012: To be submitted.
111. Magraso, A., Frontera, C., Marrero-Lopez, D., and Nunez, P., *New crystal structure and characterization of lanthanum tungstate "La_6WO_{12}" prepared by freeze-drying synthesis.* Dalton Trans., 2009(46): p. 10273-10283.
112. Erdal, S., Kalland, L.-E., Hancke, R., Polfus, J., Haugsrud, R., Norby, T., and Magrasó, A., *Defect structure and its nomenclature for mixed conducting lanthanum tungstates $La_{28-x}W_{4+x}O_{54+3x/2}$.* Int. J. Hydrogen Energy, 2012. **37**(9): p. 8051-8055.
113. Tanabe, K., *New solid acids and bases: their catalytic properties*1971, Netherland, Elsevier sicence publishers.
114. Liu, Y., Panagiotopoulos, A.Z., and Debenedetti, P.G., *Finite-size scaling study of the vapor-liquid critical properties of confined fluids: Crossover from three dimensions to two dimensions.* J. Chem. Phys., 2010. **132**(14): p. 144107.
115. Mamontov, E., *Observation of fragile-to-strong liquid transition in surface water in CeO_2.* J. Chem. Phys., 2005. **123**(17): p. 1-4.

116. Kunst, M. and Warman, J.M., *Proton mobility in ice.* Nature, 1980. **288**(5790): p. 465-467.
117. Bjerrum, N., *Structure and Properties of Ice.* Science, 1952. **115**(2989): p. 385-390.

9. Appendix

9.1. Diffusion and conductivity of $Ln_2Ce_2O_7$ (Ln=Nd, Gd)

The appendix summarizes the defect equilibria used to model the pH_2O and pO_2 dependencies of conductivity of NCO, NCCO5, GCO and GCCO5. The total conductivity is given

$$\sigma_{tot} = \sigma_{ion} + \sigma_e + \sigma_p + \sigma_{H+}$$

$$\sigma = C\mu ze$$

In this equation σ=Conductivity (Scm^{-1})

C= Concentration of defects (cm^{-3})

ze= charge of defects (C)

μ= defect mobility ($cm^2V^{-1}S^{-1}$)

$$\sigma_p = C_p \mu_p e$$

$$D_{v_o^{\bullet\bullet}} = \left(1 - X_{v_o^{\bullet\bullet}}\right) a S_{o-o}{}^2 \gamma_o \exp\frac{\Delta S_m}{k} \exp\frac{-\Delta H_m}{kT}$$

Where $X_{v_o^{\bullet\bullet}}$= the fractional oxygen vacancy concentration

γ_o= the jump attempt frequency

ΔS_m= the migration entropy

S_{o-o}= the jump distance

a= the geometrical factor

H_m= enthalpy of oxygen ion conduction

$$D_{0,v_o^{\bullet\bullet}} = a S_{o-o}{}^2 \gamma_o \exp\frac{\Delta S_m}{k}$$

$$D_{O^{2-}} = X_{v_o^{\bullet\bullet}} a S_{o-o}{}^2 \gamma_o \exp\frac{\Delta S_m}{k} \exp\frac{-\Delta H_m}{kT} = X_{v_o^{\bullet\bullet}} D_{0,v_o^{\bullet\bullet}} \exp\frac{\Delta S_m}{k}$$

$$D_{O^{2-}} N_{O^{2-}} \equiv D_{v_o^{\bullet\bullet}} N_{v_o^{\bullet\bullet}}$$

$$\sigma_{O^{2-}} = \sigma_{v_o^{\bullet\bullet}} = \frac{4e^2 C_o X_{v_o^{\bullet\bullet}} D_{v_o^{\bullet\bullet}}}{kT}$$

$$\sigma_{O^{2-}} = \frac{4e^2 C_o\left(1 - X_{v_o^{\bullet\bullet}}\right) D_{O^{2-}}}{kT} = \frac{4e^2 C_o\left(1 - X_{v_o^{\bullet\bullet}}\right) X_{v_o^{\bullet\bullet}} D_{O^{2-}}}{kT} \exp\frac{-\Delta H_m}{kT}$$

The diffusion of the vacancy $V_{\frac{7}{8}O}^{\frac{7}{4}\bullet}$ is

$$D_{V_{\frac{7}{8}O}^{\frac{7}{4}\bullet}} = X_{O_{\frac{7}{8}O}^{\frac{1}{4}/}} a{S_{o-o}}^2 \gamma_o \exp\frac{\Delta S_m}{k} \exp\frac{-\Delta H_m}{kT}$$

$$D_{0,V_{\frac{7}{8}O}^{\frac{7}{4}\bullet}} = a{S_{o-o}}^2 \gamma_o \exp\frac{\Delta S_m}{k}$$

$$D_{V_{\frac{7}{8}O}^{\frac{7}{4}\bullet}} = X_{O_{\frac{7}{8}O}^{\frac{1}{4}/}} D_{0,V_{\frac{7}{8}O}^{\frac{7}{4}\bullet}} \exp\frac{-\Delta H_m}{kT}$$

The diffusion of the oxygen ion $O_{\frac{7}{8}O}^{\frac{1}{4}/}$ is

$$D_{O_{\frac{7}{8}O}^{\frac{1}{4}/}} = X_{V_{\frac{7}{8}O}^{\frac{7}{4}\bullet}} a{S_{o-o}}^2 \gamma_o \exp\frac{\Delta S_m}{k} \exp\frac{-\Delta H_m}{kT}$$

$$D_{0,O_{\frac{7}{8}O}^{\frac{1}{4}/}} = a{S_{o-o}}^2 \gamma_o \exp\frac{\Delta S_m}{k}$$

$$D_{O_{\frac{7}{8}O}^{\frac{1}{4}/}} = X_{V_{\frac{7}{8}O}^{\frac{7}{4}\bullet}} D_{0,O_{\frac{7}{8}O}^{\frac{1}{4}/}} \exp\frac{-\Delta H_m}{kT}$$

Therefore,

$$\sigma_{V_{\frac{7}{8}O}^{\frac{7}{4}\bullet}} = \frac{4e^2 C_o X_{V_{\frac{7}{8}O}^{\frac{7}{4}\bullet}} D_{V_{\frac{7}{8}O}^{\frac{7}{4}\bullet}}}{kT} = \sigma_{O_{\frac{7}{8}O}^{\frac{1}{4}/}} = \frac{4e^2 C_o X_{O_{\frac{7}{8}O}^{\frac{1}{4}/}} D_{O_{\frac{7}{8}O}^{\frac{1}{4}/}}}{kT}$$

$$7\left[V_{\frac{7}{8}O}^{\frac{7}{4}\bullet}\right] = \left[O_{\frac{7}{8}O}^{\frac{1}{4}/}\right]$$

$$\left[V_{\frac{7}{8}O}^{\frac{7}{4}\bullet}\right] + \left[O_{\frac{7}{8}O}^{\frac{1}{4}/}\right] = 8$$

$$X_{V_{\frac{7}{8}O}^{\frac{7}{4}\bullet}} = \frac{\left[V_{\frac{7}{8}O}^{\frac{7}{4}\bullet}\right]}{\left[V_{\frac{7}{8}O}^{\frac{7}{4}\bullet}\right] + \left[O_{\frac{7}{8}O}^{\frac{1}{4}/}\right]} = \frac{1}{8}$$

$$X_{O_{\frac{7}{8}O}^{\frac{1}{4}/}} = \frac{\left[O_{\frac{7}{8}O}^{\frac{1}{4}/}\right]}{\left[V_{\frac{7}{8}O}^{\frac{7}{4}\bullet}\right] + \left[O_{\frac{7}{8}O}^{\frac{1}{4}/}\right]} = \frac{7}{8}$$

$$\sigma_{V_{\frac{7}{8}O}^{\frac{7}{4}\bullet}} = \frac{4e^2 C_o X_{V_{\frac{7}{8}O}^{\frac{7}{4}\bullet}} D_{V_{\frac{7}{8}O}^{\frac{7}{4}\bullet}}}{kT} = \frac{4e^2 C_o X_{V_{\frac{7}{8}O}^{\frac{7}{4}\bullet}} X_{O_{\frac{7}{8}O}^{\frac{1}{4}/}} D_{0,V_{\frac{7}{8}O}^{\frac{7}{4}\bullet}}}{kT} \exp\frac{-\Delta H_m}{kT}$$

The proton conductivity can be derived in the following calculation.

$$\sigma_{H+} = C_{H+}\mu_{H+}e$$

$$\mu_{H+} = \frac{\mu_{H+,0}}{T}\exp\left(\frac{-\Delta H_{m,H+}}{kT}\right)$$

$$K_H = \exp\left(\frac{\Delta S^0_{hydr}}{k}\right)\left(\frac{-\Delta H^0_{hydr}}{kT}\right)$$

$$\left[OH_{\frac{7}{8}O}^{\frac{3}{4}\bullet}\right] = (7K_H)^{\frac{1}{2}} P_{H_2O}{}^{\frac{1}{2}} = \sqrt{7}\exp\left(\frac{\Delta S^0_{hydr}}{k}\right)\left(\frac{-\Delta H^0_{hydr}}{kT}\right) P_{H_2O}{}^{\frac{1}{2}}$$

$$\sigma_{H+} = \sqrt{7}\exp\left(\frac{\Delta S^0_{hydr}}{k}\right)\left(\frac{-\Delta H^0_{hydr}}{kT}\right) P_{H_2O}{}^{\frac{1}{2}}\frac{\mu_{H+,0}}{T}\exp\left(\frac{-\Delta H_{m,H+}}{kT}\right)e$$

$$\sigma_{H+} = \frac{\sqrt{7}\mu_{H+,0}e}{T}\left(\frac{\Delta S^0_{hydr}}{2k}\right)\exp\left(-\frac{\frac{\Delta H_{hydr}{}^0}{2} + \Delta H_{m,H+}}{kT}\right) P_{H_2O}{}^{\frac{1}{2}}$$

$$\left[e^{/}\right] = \left(7K_r{}^{/}\right)^{\frac{1}{2}}(PO_2)^{-\frac{1}{4}}$$

$$\sigma_n = C_n\mu_n e = \left(7K_{0,r}{}^{/}\right)^{\frac{1}{2}}\exp\frac{-\Delta H_r{}^0}{2kT}(PO_2)^{-\frac{1}{4}}\mu_n$$

$$\mu_n = \frac{\mu_{n,0}}{T}\exp\frac{-\Delta H_{m,n}}{kT}$$

$$\sigma_n = C_n\mu_n e = \left(7K_{0,r}{}^{/}\right)^{\frac{1}{2}}\exp\left(\frac{-\Delta H_r{}^0}{2kT}\right)(PO_2)^{-\frac{1}{4}}\frac{\mu_{n,0}}{T}\exp\left(\frac{-\Delta H_{m,n}}{kT}\right)$$

$$= \frac{\left(7K_{0,r}{}^{/}\right)^{\frac{1}{2}}\mu_{n,0}}{T}\exp\left(-\frac{\frac{\Delta H_r{}^0}{2} + \Delta H_{m,n}}{kT}\right)(PO_2)^{-\frac{1}{4}}$$

Electronic conductivity can be calculated as follow

$$\sigma_p = C_p \mu_p e = \left(7K_{0,ox}{}'\right)^{\frac{1}{2}} \exp\left(\frac{-\Delta H_{ox}{}^0}{2kT}\right) (PO_2)^{\frac{1}{4}} \frac{\mu_{n,0}}{T} \exp\left(\frac{-\Delta H_{m,p}}{kT}\right) \frac{\left(7K_{0,ox}{}'\right)^{\frac{1}{2}} \mu_{p,0}}{T} \exp\left(-\frac{\frac{\Delta H_r{}^0}{2} + \Delta H_{m,p}}{kT}\right) (PO_2)^{\frac{1}{4}}$$

$$\sigma_{tot} = \sigma_{ion} + \sigma_e + \sigma_p = \sigma_{V_{\frac{7}{8}O}^{\frac{7}{4}\bullet}} + \sigma_n + \sigma_p + \sigma_{H+}$$

$$\sigma_{tot} = \frac{4e^2 C_o X_{V_{\frac{7}{8}O}^{\frac{7}{4}\bullet}} X_{O_{\frac{7}{8}O}^{\frac{1}{4}\prime}} D_{0,V_{\frac{7}{8}O}^{\frac{7}{4}\bullet}}}{kT} \exp\left(\frac{-\Delta H_m}{kT}\right) + \frac{\left(7K_{0,r}{}'\right)^{\frac{1}{2}} \mu_{n,0}}{T} \exp\left(-\frac{\frac{\Delta H_r{}^0}{2} + \Delta H_{m,n}}{kT}\right) (PO_2)^{-\frac{1}{4}}$$
$$+ \frac{\left(7K_{0,ox}{}'\right)^{\frac{1}{2}} \mu_{p,0}}{T} \exp\left(-\frac{\frac{\Delta H_{ox}{}^0}{2} + \Delta H_{m,p}}{kT}\right) (PO_2)^{\frac{1}{4}}$$
$$+ \frac{\sqrt{7}\mu_{H+,0} e}{T} \left(\frac{\Delta S_{hydr}^0}{2k}\right) \exp\left(-\frac{\frac{\Delta H_{hydr}{}^0}{2} + \Delta H_{m,H+}}{kT}\right) P_{H_2O}{}^{\frac{1}{2}}$$

The expression for the total conductivity as a function of pO_2 gives

$$\sigma_{tot} = A + B(PO_2)^{-\frac{1}{4}} + C(PO_2)^{\frac{1}{4}}$$

Similarly, the expression of the total conductivity with the change of pH_2O reads as

$$\sigma_{tot} = X + D(PO_2)^{\frac{1}{2}}$$

9.2. Rietveld refinements of NCCO5 and GCCO5

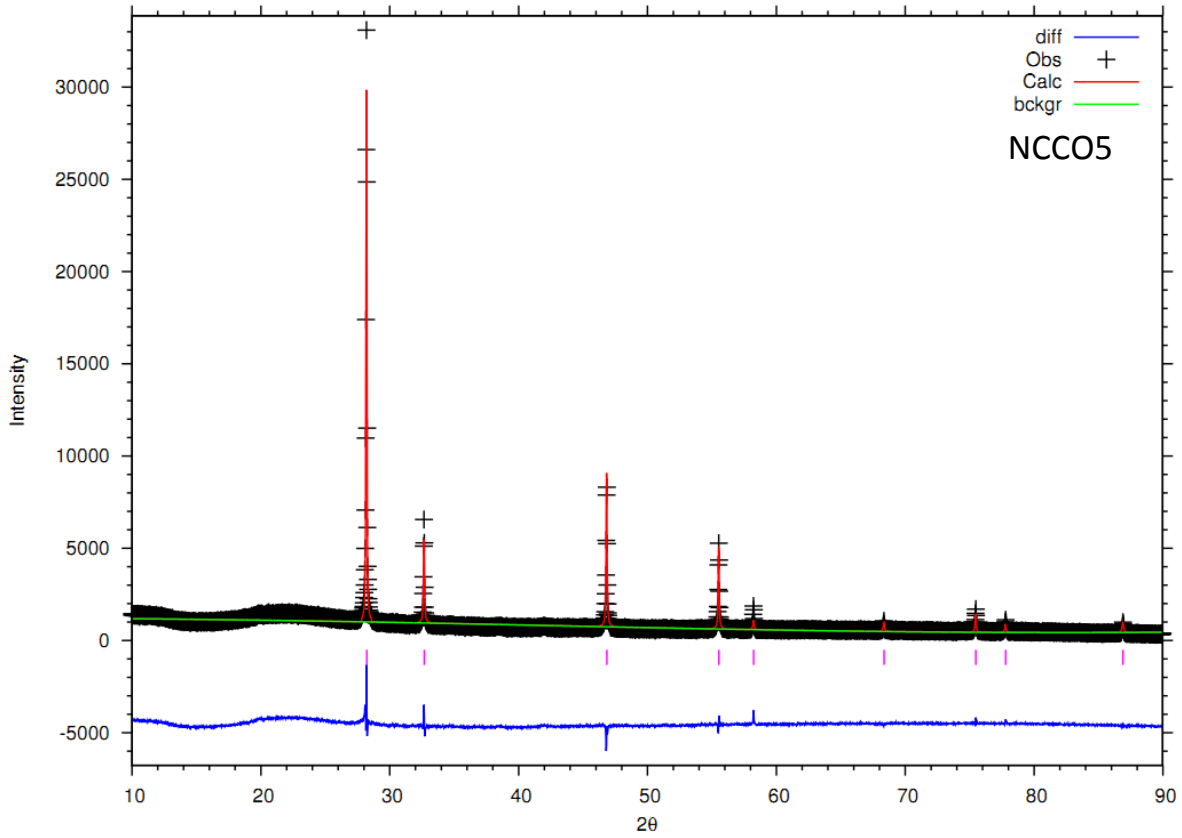

Figure 9.1 Rietveld refinement of NCCO5

Table 9.1 Crystal information of Rietveld refinement of NCCO5

Atom	Wyck.	x	y	z	U	Occupancy (n)
Nd1	4a	0.0	0.0	0.0	0.407	0.4998
Ce1	4a	0.0	0.0	0.0	0.055	0.5000
O1	8c	0.25	0.25	0.25	0.072	0.8750
Ca1	4a	0	0	0	0.008	0.0025
a(Å)	5.49289(24)	V(Å^3)	165.730(12)			

Space group $Fm\bar{3}m$, R_p (%) = 21.44, R_{wp} (%) = 13.64, χ^2 =15.50

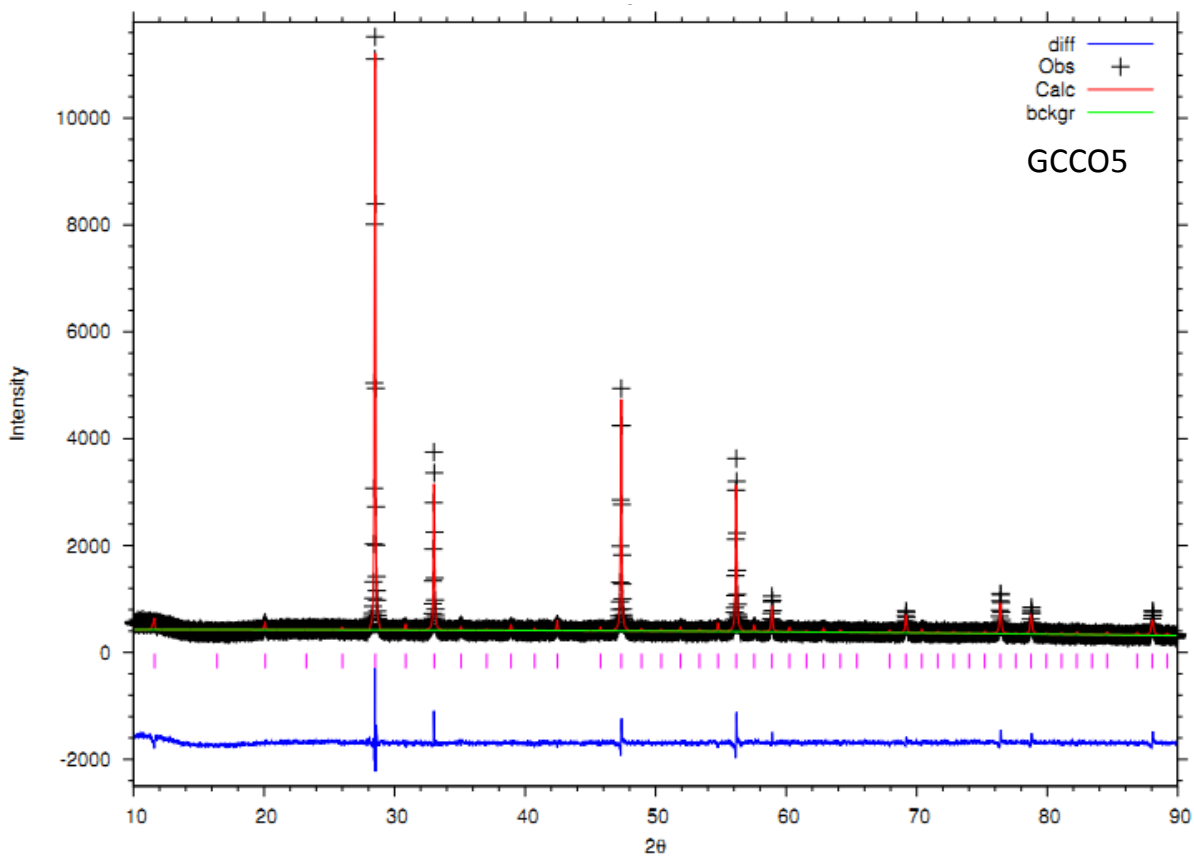

Figure 9.2 Rietveld refinement of GCCO5

Table 9.2 Crystal information of Rietveld refinement of GCCO5

Atom	Wyckoff	x	y	z	U	Occupancy (n)
Gd1	8a	0.23	0.23	0.23	0.052	0.5147
Ce1	8a	0.27	0.27	0.27	0.052	0.5000
Gd2	12b	0.50	0.50	0.25	0.039	0.9756
Ce2	12b	0.98	0	0.25	0.029	1.0000
Ca1	8a	0.23	0.23	0.23	0.025	0.0025
O1	24c	0.38	0.15	0.38	0.054	1.0000
O2	24c	0.63	0.88	0.62	0.018	1.0000
O3	8a	0.38	0.38	0.38	0.027	1.0000
a(Å)	10.87198(20)	V(Å^3)	1285.07(4)			

Space group $I2_13$, Rp (%) = 9.97, R_{wp} (%) = 7.83, χ^2 =2.68